Extension of a Finite Element Model to 2D for the Prediction of Adiabatic Shear Bands

by

Jeffrey Delorme

A thesis submitted to the Faculty of Graduate Studies of

The University of Manitoba

In partial fulfillment of the requirements of the degree of

Master of Science

Department of Mechanical and Manufacturing Engineering

University of Manitoba

Winnipeg, Manitoba, Canada

ABSTRACT

Failure of metals under impact loading is known to occur through the formation of adiabatic shear bands (ASBs). ASBs appear in materials as evidence of damage, and are known to be sites for material failure. General purpose plasticity models fail to predict the phenomenon of ASB formation. The present research validates and extends a model developed at the University of Manitoba by Feng and Bassim to predict damage due to ASBs.

Parameters for the Feng and Bassim model are determined experimentally using a direct impact pressure bar to impact specimens at temperatures of 20-500^{o}C and strain rates of 500-3000/s. A direct impact experiment is simulated in ANSYS using the model and fitted parameters. The results of the simulation show localized temperature rise and predict failure at the same locations as those observed experimentally. Nominal strain to failure is approximately 40-50% for a specimen impacted at 38 kg-m/s.

ACKNOWLEDGEMENTS

I would like to extend my sincere appreciation and thanks to my advisor, Dr. Nabil Bassim, for his support and guidance. Professor Bassim has been a huge source of encouragement and inspiration during this endeavor, his meetings never fail to trigger new ideas and provide a renewed sense of purpose. The trust he places in the abilities of his students and the independence associated with this trust has always made the pursuit of knowledge both challenging and rewarding, and I could not have asked for a better advisor to watch over my progress and evolution as a student over the past 4 years.

For their patience and support, I would like to thank my family and loved ones, especially my parents Murray and Janet Delorme, and girlfriend Sarah Sung. Without their continuous support, this degree would not have been possible.

I would also like to thank my examining committee, Dr. Malcolm Xing and Dr. Mohamed Bassuoni for taking the time to read and review the work I have completed.

Finally, I would like to thank my co-workers and fellow graduate students, Ian Polyzois and Solomon Boakye-Yiadom for the company and many fruitful conversations that have surely helped to shape this thesis in one way or another.

TABLE OF CONTENTS

LIST OF FIGURES

LIST OF TABLES

CHAPTER 1: INTRODUCTION

Metals and alloys subjected to impact type loading conditions are susceptible to failure through the formation of adiabatic shear bands (ASBs). Adiabatic shear bands are regions of intensely localized deformation that arise in metals at very high strain rates , on the order of $>10^2$/s), and large strains. Two competing mechanisms are at work in metals deforming under these conditions, namely strain hardening and thermal softening. Strain hardening tends to increase the flow stress, while thermal softening tends to decrease the flow stress as the material heats up. The initial stage of the deformation is dominated by strain hardening. Softening eventually overpowers the hardening stage as thermal energy generated due to plastic work is unable to dissipate to the surrounding material via conduction. Once the shear band has established a definite shape, the shear strain becomes localized within the band and the areas directly adjacent to the shear band experience an "unloading" of strain. Past this point, almost all of the bulk shear strain is limited to the narrow band and the material on either side is experiencing rigid translation. Even if straining is arrested prior to total collapse, the material within the band becomes extremely brittle upon cooling and are susceptible to cracking. For this reason, adiabatic shear bands have been described as a "fingerprint" of damage, and indicate that a material has been compromised.

The prediction of material failure during impact is studied by means of physical testing and computer simulation. Physical testing includes full scale field tests and generalized laboratory tests. The former may be thought of as crash testing in the automotive industry, or blast/penetration testing in military applications. These tests provide realistic loading conditions, but are extremely time consuming, expensive, have limited

repeatability, and it is difficult to generalize the results to other geometries or loading conditions. The second type of physical testing, referred to here as laboratory testing, describes methods related to a particular material of specific geometry under a more simplified type of loading. These tests are generally regarded to be more repeatable and cost effective than full scale destructive testing. The results of these tests are usually in the form of stress-strain relationships for a given combination of strain rate, temperature, and mode of loading (tension, compression, pure shear/torsion, plane strain, bending).

The focus of the present work is to study the behaviour of materials under impact at strain rates of 10^2 - 10^4/s. Hopkinson Bar devices are used for testing materials in this strain rate range.

Numerical simulations developed at the University of Manitoba (Feng and Bassim 1999) were developed to predict the high strain rate behaviour of steel under torsion. The objective of the current work is to extend this model to other states of stress and generalize to other materials based on the physical process of dynamic recrystallization.

CHAPTER 2: LITERATURE REVIEW

2.1 Deformation of Metals

The deformation behaviour of ductile metals may be characterized as elastic followed by plastic. Elastic behaviour refers to the stage of deformation that is reversible. Once the load is removed the material returns to its original shape. This stage extends up to the yield point, which is typically around 0.2-0.5% total strain for steels (Callister 1994). After the yield point, the material begins to deform in an irreversible, plastic manner. This stage is accompanied by strain hardening, which is to say that the stress to deform the material increases with increasing the applied strain.

2.1.1 The Crystal Structure of Metal and Dislocations

Metals are crystalline materials and their atoms are stacked in a definite pattern, occupying specific positions in a lattice structure. This lattice may be face centered cubic (FCC), body centered cubic (BCC), or hexagonal close packed (HCP). These structures are shown in Figure 2.1. Examples or each lattice arrangement are: aluminum (FCC), steel (BCC), and magnesium (HCP). The specific arrangement plays an important role in the plastic behaviour of the metal.

Figure 2.1: Crystal structure of metals (Adapted from Hull and Bacon (1984))

Metals deform when the planes of atoms are displaced from their initial lattice positions through a process known as slip. The theoretical amount of shearing force (τ) required to deform a perfect crystal by sliding one plane of atoms across the adjacent plane has been calculated by Frenkel (1926) as:

$$\tau = \frac{Gb}{2\pi a} \sin\left(\frac{2\pi x}{b}\right) \qquad (2.1)$$

where "G" is the shear modulus, "a" is the distance between planes, "b" is the interatomic spacing, and "x" is the displacement from the equilibrium position in the direction parallel to the planes. The maximum of this function is referred to as the "critical resolved shear stress" and is many orders of magnitude larger than the observed yield stress in metals (10^3-10^7). This discrepancy is explained by using dislocation mechanics.

A dislocation refers to a line defect within the crystal lattice. This defect is described as either edge, screw, or mixed configuration which is a combination of the two. A schematic of each type is shown in Figure 2.2.

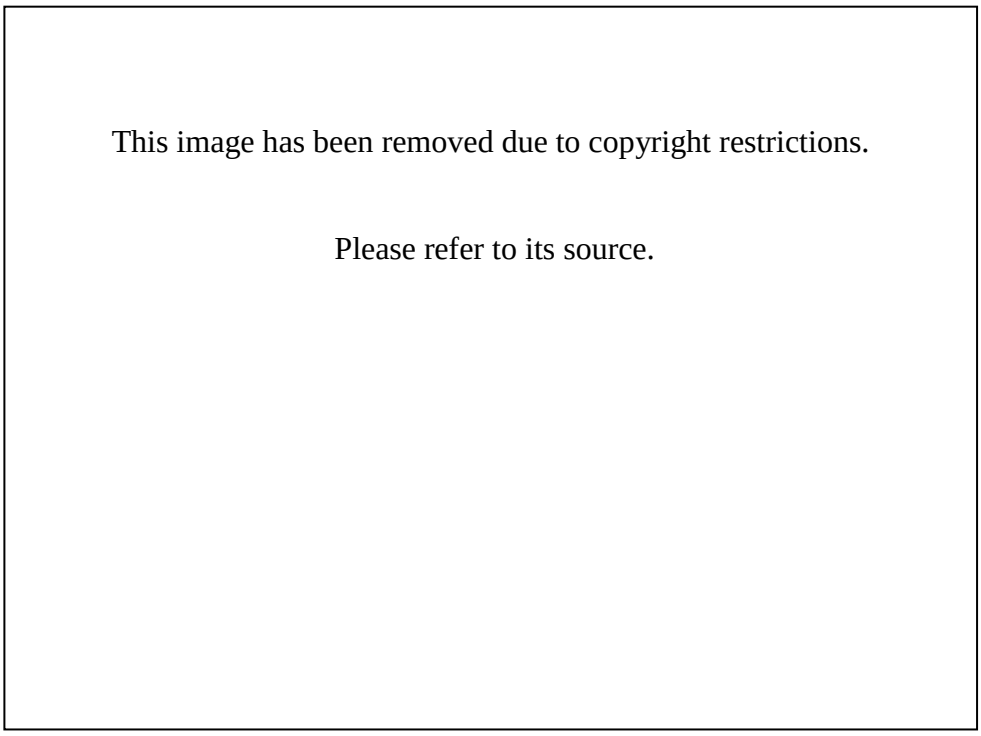

Figure 2.2 : Edge (above) and screw (below) dislocations (Hull and Bacon 1984)

The deformation of metals is attributed to the movement of these defects through the crystal, and the applied resolved shear stress required to mobilize a dislocation is far below the critical resolved shear stress mentioned above. This stress required to overcome the lattice resistance is referred to as the Peierls-Nabarro stress, and is expressed as a function of the shear modulus (G), Poisson's ratio (ν), interatomic spacing (b), interplanar spacing (a), and dislocation type (edge or screw):

$$\tau_p = \frac{2G}{1-\nu} \exp\left(-\frac{2\pi w}{b}\right) \tag{2.2}$$

Where,

$$w = \frac{a}{1-\nu} \text{ (For an edge dislocation)} \quad (2.3)$$

$$w = a \text{ (For a screw dislocation)} \quad (2.4)$$

This relationship is important since it suggests that a much lower stress is required to deform a material than the critical resolved shear stress, indicating that the movement of dislocations is an acceptable explanation for deformation in metals.

When a material is initially deformed at the yield stress, dislocations have fewer obstacles to overcome and the mean free path is longer (the distance a dislocation may travel unimpeded). As the material is deformed further, dislocations begin to interact with each other and tangle, increasing the amount of energy required to move. This increase in resistance is due to strain hardening in the material.

2.1.2 Thermal Softening

In addition to strain hardening, another phenomenon is important when a material is strained at high strain rates, namely thermal softening. Thermal softening describes the observation that materials become more ductile and require less stress to flow plastically at elevated temperatures.

The effect of thermal softening may be explained by considering the energy required for dislocations to travel through the material and overcome obstacles. The energy required to move dislocations consists of a thermal component and a mechanical component. At elevated temperatures and lower strain rates, the additional energy required to move dislocations is decreased and this leads to a decrease in flow stress (Hull and Bacon 1984). This is illustrated in figures 2.3 and 2.4.

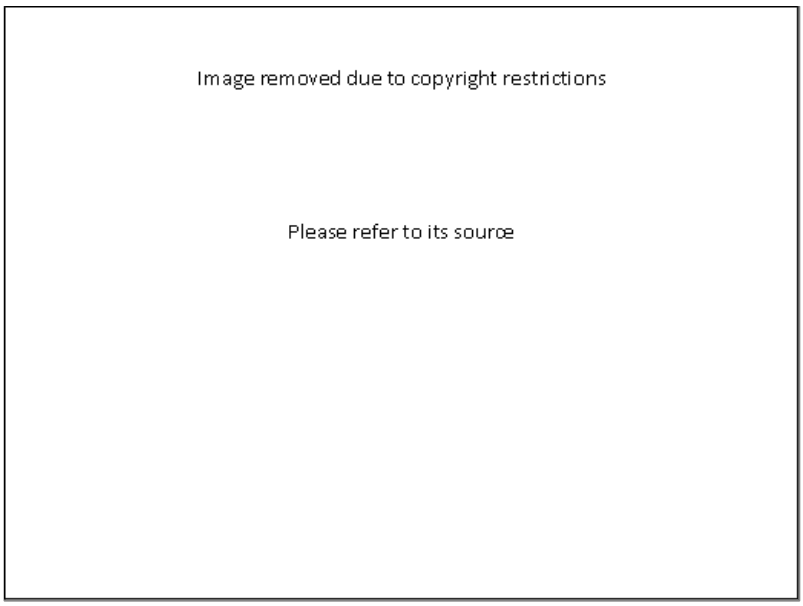

Figure 2.3: Resistive force for move an array of dislocations, showing thermal and mechanical components (adapted from Hull and Bacon, 1984)

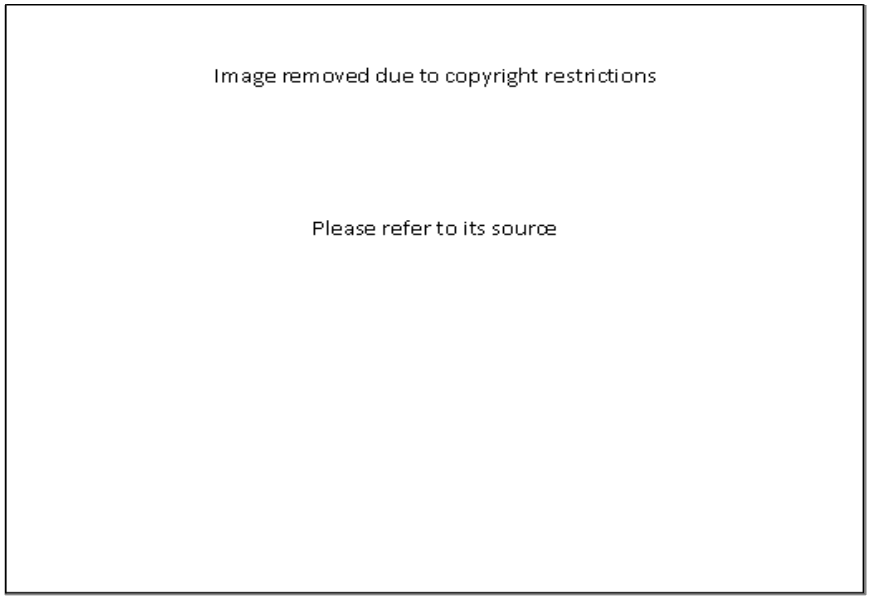

Figure 2.4: Components of resistive force to move dislocations as a function of temperature (adapted from Hull and Bacon, 1984)

Since it has been established that metals deform by the movement of dislocations, and the force required to move dislocations has a thermal component that vanishes at elevated temperature, it follows that the applied stress required to plastically deform a material will decrease with increasing temperature. This phenomenon is referred to as thermal softening.

2.2 Adiabatic Shear Bands

2.2.1 Occurrence of Adiabatic Shear Bands

Tresca first observed adiabatic shear bands in 1878 as "X" shaped patterns that occurred in a Platinum-Iridium alloy subjected to impact. Tresca concluded that materials of high strength, with favourable thermal properties (low conductivity and heat capacity) tend to favor the formation of these "hot crosses".

Zener and Hollomon (1944) were the first to characterize adiabatic shear bands as evidence of thermal instability, and postulated that the instability was due to the competition of strain hardening and thermal softening. They examined the effect of punching speed during a blanking operation on the characteristics of the deformed material. They found that shear strain became localized as the strain rate increased, and at very high speeds the material was found to transform into regions that appeared white under an optical microscope when etched. The term "white etching band" is now used to describe this type of shear band, and is synonymous with the term "transformed band". The white etching bands were found to be similar to untempered martensite - very hard, brittle, and prone to cracking. This work initiated several decades of research to further characterize adiabatic shear bands and attempt to explain the underlying mechanisms.

Since the time of Zener and Hollomon, adiabatic shear bands have been observed in many materials, some of which appear below in Table 2.1. For a more extensive list, refer to Bai and Dodd (1992).

Table 2.1: List of metals observed to exhibit adiabatic shearing

Aluminum	Aluminum Alloy	Stock and Thompson (1970)
	Metal-Matrix Composites	Odeshi et al. (2007)
	Aluminum-Lithium	Xu et al. (2001)
Titanium	Commercially Pure	Meyers and Pak (1986)
	Titanium Alloy (review of several)	Shahan and Taheri (1993)
Steels	Low Carbon	Xu et al. (1990)
	Mild Steel	Klepaczko (1994)
	High Strength Alloy Steel	Bassim (2001)
	Maraging Steel	Nazimuddin (2010)
Copper	Commercially Pure	Yazdani, Bassim, and Odeshi (2009)
Magnesium	Magnesium Alloy	Zou et al. (2011)
Tantalum	Commercially Pure	Pérez-Prado, Hines, and Vecchio (2001)
	Tantalum - Tungsten	Perez-Prado, Hines, and Vecchio (2001)
Tungsten	Tungsten Alloy	Bose, Couque, and Lankford Jr (1992)
Uranium	Uranium Alloy	Batra and Kim (1992)
Zirconium	HCP-Zr	Kad et al. (2006)
Platinum	Platinum - Iridium	Tresca (1878)

Adiabatic shear bands are categorized as either deformed bands or transformed bands. In steels, deformed bands appear as sections of elongated grains, as shown in Figure 2.5Figure 2.. These deformed bands are observed at lower impact velocities and are considered to be less severe than transformed bands (Nazimuddin, 2010).

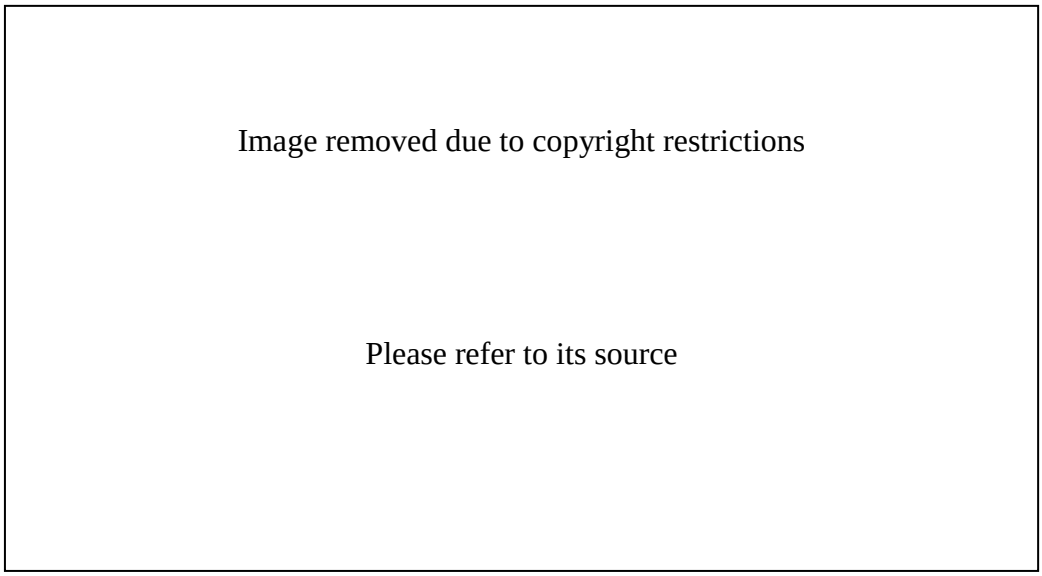

Figure 2.5: Deformed band in high hardness alloy (HHA) steel (Nazimuddin, 2010)

The second type of adiabatic shear band are referred to as "transformed" or "white etching" bands, as discussed earlier in this section. A micrograph of a white etching band is shown in Figure 2.6.

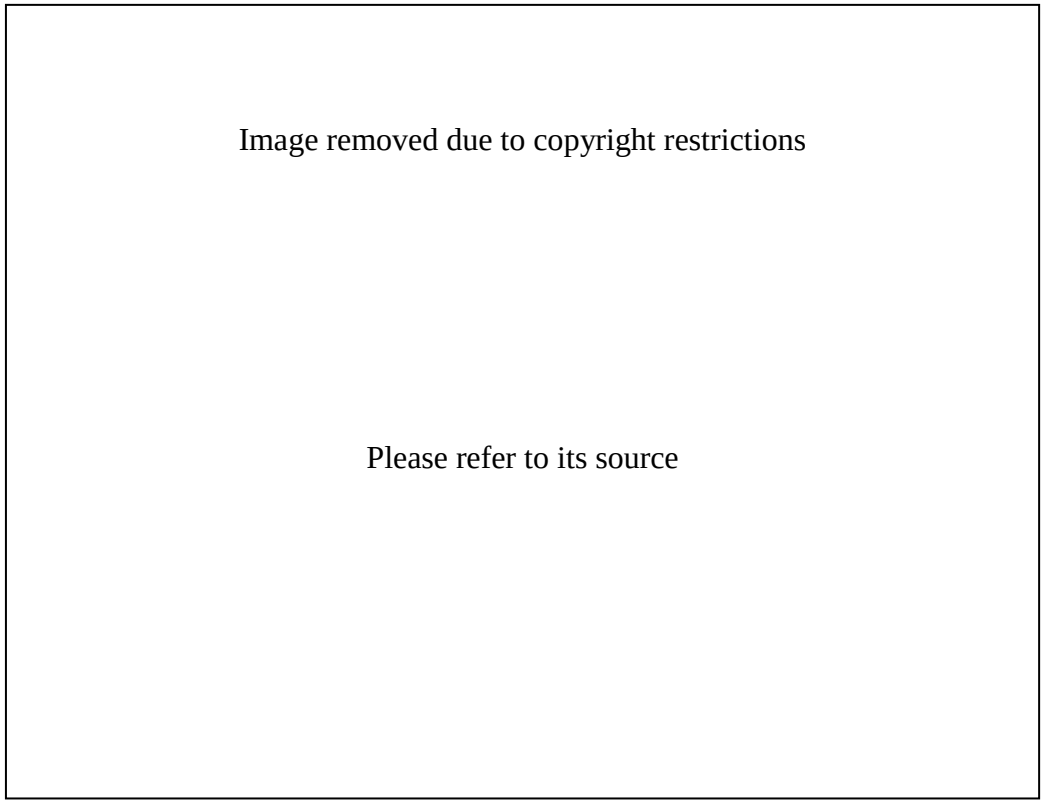

Figure 2.6: Transformed band in Maraging Steel (Nazimuddin, 2010)

The formation of white etching bands is particularly dangerous since the material becomes very brittle and prone to cracking. Cracks are often observed to form within white etching bands, as shown in Figure 2.7.

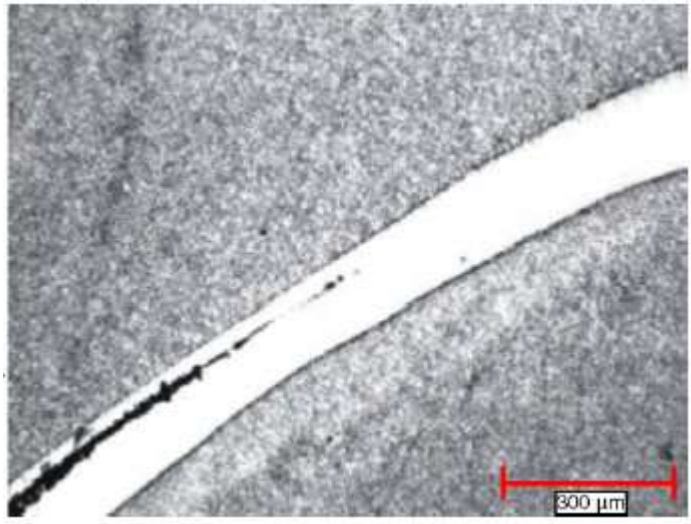

Figure 2.7: Crack formed in a white etching band. Used with permission from (Odeshi et al. 2005)

The width of adiabatic shear bands has been found to be generally on the order of 20-400 μm (Huang (1987), for steels, depending on the strain rate. The general trend observed is that larger strain rates tend to produce narrower shear bands (Lee et al. 2010). Local strains of 100-350% are commonly observed (Liao and Duffy 1998), but strains as high as 500 have been reported by Ashby and Verrall (1973).

2.2.2 Formation of Adiabatic Shear Bands

Zener and Hollomon (1944) proposed the first theory of adiabatic shear band formation, as discussed previously. This theory considered the hardening and softening as competing mechanisms. Eventually the softening mechanism overpowers hardening and the material fails by thermal collapse along the shear band.

Marchand and Duffy (1988) studied the mechanics of shear band formation in HY-100 steel under high strain rate torsion using high speed photography and a specimen

with a grid pattern printed on its surface. They found three distinct stages of the deformation process:

i) Homogenous deformation - All of the grids deforming together

ii) Inhomogeneous deformation - Some grids deforming more than others

iii) Localization into shear bands - All deformation occurring along a narrow band

These stages are illustrated in Figure 2.8.

Figure 2.8: Stages of Adiabatic Shear Band formation, Marchand and Duffy (1988)

The core concept of hardening and softening suggested by Zener and Hollomon persists even today, but there is considerable debate about the mechanisms behind the softening and the evolution of adiabatic shear bands. The initial premise of truly "transformed" bands by austenization of the structure was shown to be incorrect since the

calculated temperature rise in the material is insufficient to austenize the material (approximately 830^{o}C would be required). Experimental work by Marchand and Duffy (1988) measured a maximum temperature rise of approximately 600^{o}C, and subsequent work by Liang and Duffy (1998) and Hartley, Duffy, and Hawley (1987) measured peak temperatures of only 440-550^{o}C. Numerical simulations at the University of Manitoba were conducted and found to be in agreement with these values (Feng and Bassim 1999).

2.2.3 Dynamic Recrystallization

The mechanism of softening and formation of adiabatic shear bands is still not well understood, but it is generally accepted that the process is related to a phenomenon known as dynamic recrystallization. Dynamic recrystallization refers to a rearrangement of the microstructure in a material undergoing high strain rate, high temperature deformation. This process is marked by a refinement of grains and decrease in dislocation density, and differs from static recrystallization in that the kinetics are much faster and the refined grains are very small (McQueen and Bergerson 1972). Materials undergoing dynamic recrystallization lose mechanical properties and soften during this process.

Dynamic recrystallization was initially observed and proposed as a mechanism for ASB by (Meyers and Pak 1986) and has since been substantiated by the studies of Andrade et al. (1994), Mescheryakov and Atroshenko (in (Murr, Staudhammer, and Meyers 1995)), Hines and Vecchio (1997), Meyers et al.(2001). This phenomenon has been studied from a numerical perspective by Chichili et al. (2004), Meyers et al. (2000),

and has been applied to ASB formation by Medyanik, Liu, and Li (2007) and more recently by Dolinski, Rittel, and Dorogoy (2010).

The principal observation that suggests the occurrence of dynamic recrystallization is that the ASB contains very fine grains with a comparatively low dislocation density. The formation of new grains by a static process has been ruled out by Hines and Vecchio (1997) according to the criteria proposed by McQueen and Bergerson (1972) and calculations based on the time required for diffusion under static recrystallization conditions.

The mechanism for the initiation of dynamic recrystallization is not yet fully understood. Initially, Meyers and Pak (1986) proposed a process of micrograin rotation and sliding or micrograin boundaries, shown in Figure 2.9.

Figure 2.9: Proposed mechanism of formation for dynamically recrystallized micrograins, Meyers and Pak (1986)

Rittel (2009) considers the mechanism as an athermal process brought on by buildup of strain energy due to cold work, as opposed to a thermally activated process (as in the model of Medyanik, Liu, and Li (2007). The main argument that Rittel makes for an athermal process is that high temperatures are not a prerequisite for the initiation of ASBs, since the severe temperature rise does not begin to occur until after localization has been initiated.

Dynamic recrystallization has been shown to require a critical temperature to initiate (Medyanik, Liu, and Li (2007)), which depends on the applied strain rate. This temperature is shown to be approximately 0.4Tm at strain rats above 100/s.

2.3 Models of Adiabatic Shear Bands

2.3.1 Thermo-Viscoplastic Models

Numerical simulation is a powerful tool to predict material behaviour, and is widely used for design problems. Adiabatic shear bands pose several challenges to numerical simulation. First and foremost is that ASBs are both a temperature and strain rate dependent process, and the material model selected to simulate ASBs must examine these two effects. This family of model is referred to as thermo-viscoplastic, and may be expressed in a general form as (De Souza Neto et al. 2008):

Flow Rule: $\dot{\epsilon}^p = \boldsymbol{G}(\boldsymbol{\sigma}, \boldsymbol{A}, T)$ (2.5)

Hardening Law: $\dot{\boldsymbol{\alpha}} = \boldsymbol{J}(\boldsymbol{\sigma}, \boldsymbol{A}, T)$ (2.6)

where $\boldsymbol{\alpha}$ is the set of hardening internal variables, **G** and **J** are constitutive functions, $\boldsymbol{\sigma}$ is the Cauchy stress tensor, $\boldsymbol{A}$ is a set of hardening forces, and T is the temperature. The form of **G** and **J** is unique to each model, for example Johnson-Cook or Anand plasticity (two popular plasticity models) each have their own set of constitutive equations that define a unique flow rule and hardening law. These constitutive equations are implemented using numerical techniques, such as the finite element method, to predict the behaviour of a material.

Several models exist for predicting the time and temperature dependent high strain rate plastic behaviour of metals. They may be broadly divided into two categories, namely phenomenological and physical. Phenomenological models are entirely based on empirical data, whereas physical models are based on the underlying physics of the

problem (dislocation mechanics). It is important to emphasize that even though the physical models are based on a physical and tangible process, they still rely on empirical data processing to extract useful parameters. The advantage of physical dislocation based models is that they are more closely tied to the mechanism of deformation, and more general statements and extrapolations may be made from the model to simulate similar materials more accurately.

The next section presents several empirical and phenomenological models reported in the literature to describe the thermo-viscoplastic behaviour of metals. This list is by no means exhaustive. There are many models reported in the literature, and those selected for more in depth discussion represent some of the more common models in use that are applicable to ASB simulation. The differences between these models generally lies in the expression of the flow rule or hardening law, described in general terms earlier in this section.

2.3.1.1 Johnson-Cook Model

The Johnson-Cook model (Johnson and Cook 1983) is perhaps the most common of all thermo-viscoplastic models. It is an entirely empirical model that is built into most large commercial finite element software packages (eg. ANSYS LS-DYNA, Abaqus). The flow stress ($\bar{\sigma}$) is expressed as a function of equivalent plastic strain ($\bar{\epsilon}$), strain rate ($\dot{\bar{\epsilon}}$), and temperature ($\hat{\theta}^m$),

$$\bar{\sigma} = \left(A + B\bar{\varepsilon}^n\right)\left[1 + C\ln\left(\frac{\dot{\bar{\varepsilon}}}{\dot{\bar{\varepsilon}}_0}\right)\right]\left(1 - \hat{\theta}^m\right) \tag{2.7}$$

where temperature is expressed as the homologous temperature given by:

$$\hat{\theta} = \frac{\theta - \theta_{room}}{\theta_{melt} - \theta_{room}} \tag{2.8}$$

and the strain rate is expressed as normalized equivalent strain rate:

$$\frac{\dot{\bar{\epsilon}}}{\dot{\epsilon}_0} \tag{2.9}$$

A,B,C, and m are material constants determined empirically from experimental data, and n is the strain hardening exponent.

The Johnson-Cook model assumes isotropic behaviour and is limited in its ability to accurately capture work hardening in certain cases. As discussed by Riqiang and Khan (1999), the Johnson-Cook model is limited to cases where there is positive correlation between strain rate and work hardening rate. It is unable to capture the behaviour of metals that show a decrease in work hardening rate at elevated strain rates (such as

tantalum). The model can be used for metals that show an increasing rate of hardening at higher strain rates (such as copper), or metals that show a constant rate of hardening at increasing strain rates (such as aluminum or steel).

2.3.1.2 Zerilli-Armstrong Model

The Zerilli-Armstrong Model (Zerilli and Armstrong 1987) is a physically motivated model that is based on dislocation mechanics. This model takes into consideration the crystal structure (HCP,BCC,FCC), grain size, temperature, initial dislocation density, presence of solutes, The constitutive equations are given as:

$$For\ BCC:\ \sigma_\epsilon = \Delta\sigma_G + B_o \exp((-\beta_o + \beta_1 \ln(\dot{\epsilon})T)) + K_o\epsilon^n + \frac{k_\epsilon}{\sqrt{l}} \quad (2.10)$$

$$For\ FCC:\ \sigma_\epsilon = \Delta\sigma_G + B_1\sqrt{\epsilon}\ \exp((-\beta_o + \beta_1 \ln(\dot{\epsilon})T)) + \frac{k_\epsilon}{\sqrt{l}} \quad (2.11)$$

where $\Delta\ \sigma_G$ is the athermal (mechanical) component of the stress, as discussed above in section 2.1; k_h is the microstructural stress intensity, B, B_o are material constants, l is the average grain diameter, and T is the temperature (absolute scale)

The flow stress is assumed to consist of two components, the thermal and athermal component, as discussed previously,

$$\sigma = \sigma_{at} + \sigma_{th}. \quad (2.12)$$

The thermal component is assumed to follow an exponential of the form:

$$\sigma_{th} = \sigma_{th_o} \exp(-\beta T) \quad (2.13)$$

where σ_{th_o} is the stress contribution to overcome initial dislocations and defects, and the exponential factor β is a function of strain rate:

$$\beta = \beta_o - \beta_1 \ln\left(\frac{\dot{\epsilon}_p}{\epsilon_o}\right) \tag{2.14}$$

The Zerilli-Armstrong model has at least one clear advantage over Johnson-Cook, which is that the strain rate and temperature are coupled (Johnson and Holmquist 1988). A disadvantage of the Zerilli-Armstrong model is that, like the Johnson-Cook model, it does not take into consideration any history effects, such as load/hold/reload (Riqiang and Khan 1999).

2.3.1.3 Anand's Model

While the initial work done by Anand (Anand 1985) was based on constitutive equations for the hot working of metals, it has been adopted for use as a general thermo-viscoplastic material model for large deformation with relatively low elasticity.

Anand's model uses a single internal scalar state variable ("s") representing the material's average isotropic resistance to plastic flow. This variable accounts for any microstructural effects which may act to raise or lower the resistance to plastic deformation, such as dislocation density, presence of defects/solutes, or state of hardenining.

One functional form for the Anand model flow rule is expressed as:

$$\dot{\tilde{\epsilon}}^p = A \exp\left(-\frac{Q}{R\theta}\right)\left[\sinh\left(\xi\frac{\tilde{\sigma}}{s}\right)\right]^{\frac{1}{m}} \tag{2.15}$$

Characteristics of Anand materials are that they do not have a yielding threshold, and the flow stress saturates to a constant value for a given strain rate and temperature. The lack of yielding threshold means that Anand materials should not be used for materials that have large elastic deformation. Anand's model has a definite advantage over Johnson-Cook and Zerilli-Armstrong in that it is able to capture strain history effects.

2.3.2 Models of Adiabatic Shear Bands

The first actual numerical model which included nucleation and growth of adiabatic shear bands appeared in 1980 with the work of Erlich, Seamen, and Shockley (1980). This model was primitive in the sense that the actual mechanics of the problem were not completely understood at this time, but it provided a starting point for further work in the area.

After this initial attempt at explaining the mechanics of the adiabatic shear problem numerically, an extraordinary amount of work was completed in the area. Several monographs exist on the subject, including works by Shawki and Clifton (1989), Bai and Dodd (1992), (Meyers 1994), and Wright (2002).

Several analytical solutions to the adiabatic shear problem exist, but only for simplified cases. These solutions are generally 1-D and use very simple material models. For example, the case of a finite slab in 1-D simple shear was considered by Wright and Batra (1985). This model considered an ideal thermally softening/strain hardening material. Shear band formation was initiated by altering the boundary conditions and introducing a perturbation at the point of maximum shear stress. The primary

disadvantage of this style of model is that it is not adaptable as a predictive tool, and is limited to a single (very specific and simplified) case. A limited number of two dimensional solutions also exist (Wright 2002) but these solutions have similar disadvantages and limitations.

General finite element solutions attempt to predict shear band failure based on some criteria, typically either a critical stress or strain. Batra and Lear (2004) examined a strain and rate hardening material with thermal softening and modeled ductile failure by porosity formation using a maximum strain criteria. This technique assumed a material to have failed once a critical predetermined strain is reached. Work completed at the University of Manitoba applied a similar technique to predict ductile failure (Polyzois 2010) and the formation of adiabatic shear bands in an armour steel, namely maraging steel 300, under impact loading conditions.

An alternative to maximum strain criteria is a maximum stress criteria. Batra and Kim (1992) examined twelve materials using the Johnson-Cook plasticity model to predict shear band failure and used a decrease in stress as the marker for failure. They observed that localization sets in when the stress has decreased by 5-10% after having achieved the peak value. This criteria is illustrated below in Figure 2.10.

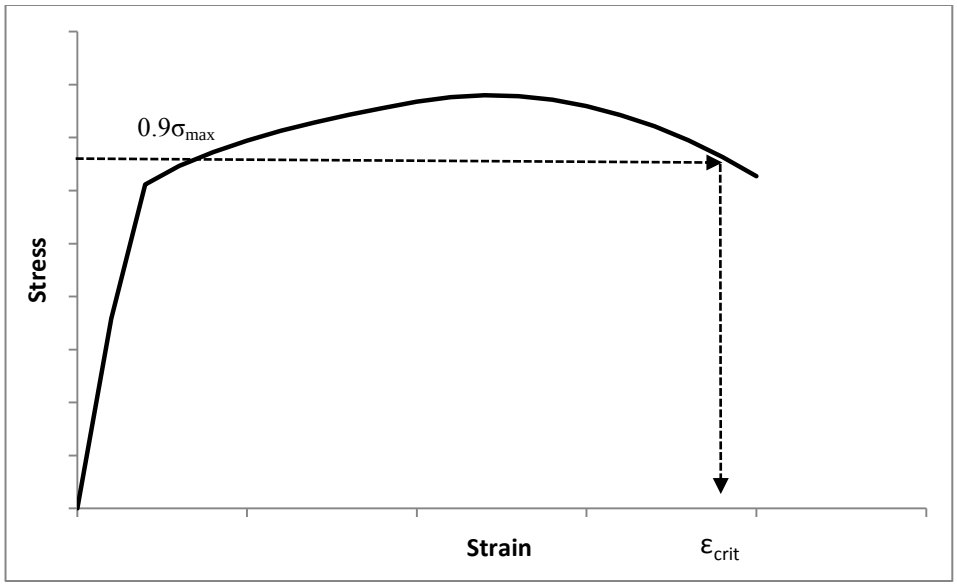

Figure 2.10: Critical Strain as a function of stress decay past peak stress, as presented by Batra and Kim (1992).

A strain based failure criteria proposed by Zhou, Ravichandran, and Rosakis (1996) that takes the loading rate into consideration. That is to say, the material will have "failed" at a lower total strain when loaded at elevated strain rates. This method is of the form:

$$\epsilon_{cr} = \epsilon_1 + (\epsilon_2 - \epsilon_1)\left(\frac{\dot{\epsilon}_r}{\dot{\epsilon}_r + \dot{\epsilon}}\right) \tag{2.16}$$

Where ϵ_n , $\dot{\epsilon}_r$ are material constants, fitted from empitical data. The major problem identified with this approach is that the parameters have no real physical significance, and estimating them without the necessary experimental data is not reliable. This criterion is shown graphically in Figure 2.11.

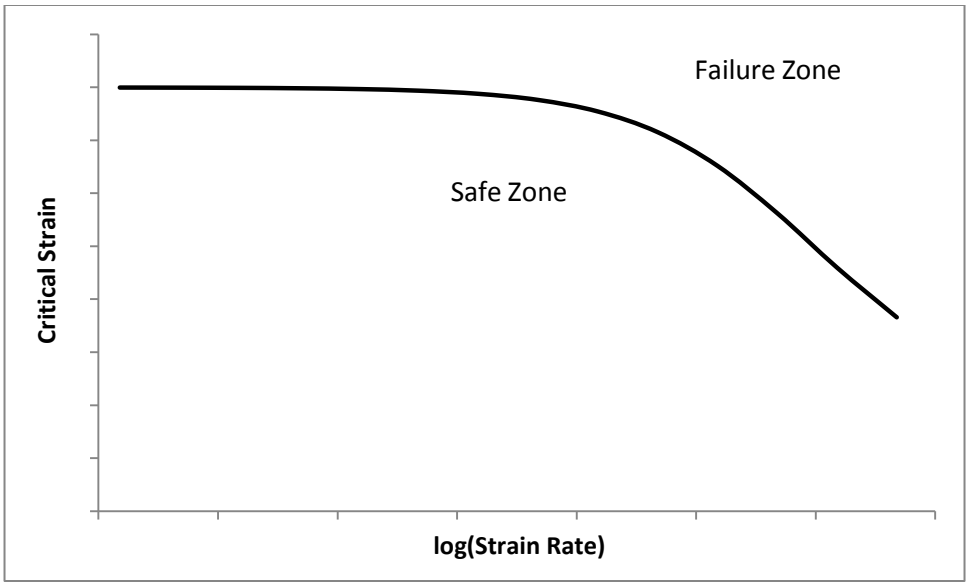

Figure 2.11: Empirical strain rate dependent failure criteria (Eq. 2.16)

A similar approach for defining failure that still maintains the physics of the problem was explored by Wright et al. (2004). This technique incorporated a set of scaling laws into a numerical code to predict the onset of instability. This particular work by Wright attempted to predict void formation and shear band formation. Schoenfeld and Wright (2003) used a similar method to predict the timing of ASB formation from homogenous material properties. They observed that three distinct types of material behaviour are exhibited in regions in and around ASBs, these behaviours are shown in Figure 2.12.

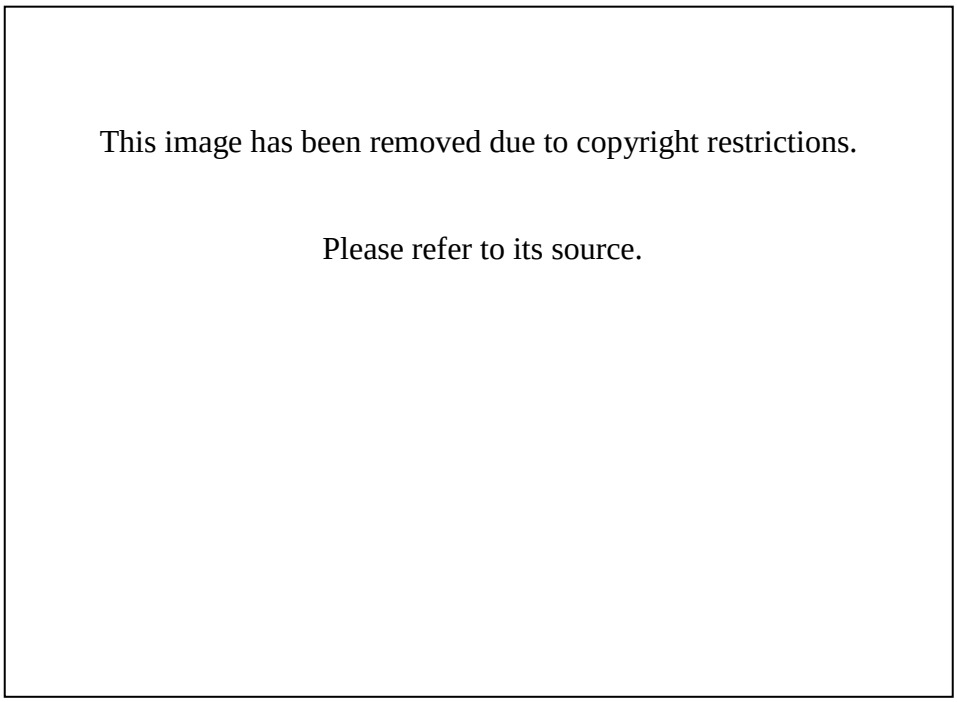

Figure 2.12: Three types of material behaviour in and around ASBs (Schoenfeld and Wright (2003))

A material without softening due to excess heat buildup behaves in an isothermal manner, this is shown with the coarse dashed line and would be expected at lower strain rates. As strain rates are increased, adiabatic heating becomes important and the change of material properties due to heat buildup must be considered. This type of behaviour is labeled as "Adiabatic" in Figure 2.12, and would be expected to be observed in regions of high strain rates without ASBs, such as the bulk material surrounding an ASB. During the formation of ASBs, inhomogeneous properties or loading lead to an additional loss of load carrying capacity due to localization of shear strain. This curve is shown in Figure 2.12 as "Localization", and represents the behaviour of a material within the ASB.

This method has the advantage of being able to predict failure due to ASB formation without a database of information, such as would be required for a

phenomenological failure model (for example, the Johnson-Cook damage model (Johnson and Cook 1985)).

2.3.2.1 Feng-Bassim Model of Adiabatic Shear Bands

Feng and Bassim (1999), at the University of Manitoba, combined Anand's model with an exponential softening term to predict the occurrence of ASBs in AISI 4340 steel under high strain rate torsional (pure shear) strains. The mesh and location of the elements on the physical specimen is shown in Figure 2.12 below.

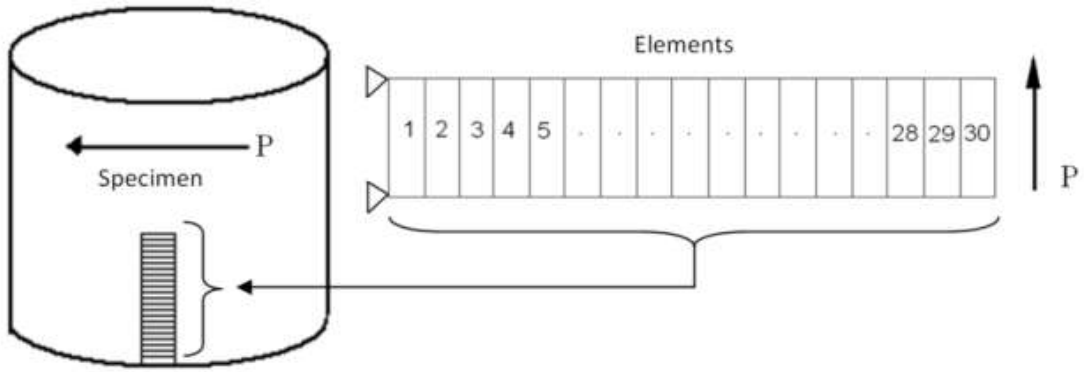

Figure 2.13: Location of finite element mesh of Feng and Bassim along specimen

This approach observed that the hardening and softening behaviour could be treated as separate phenomena which each contribute to the resistance to plastic flow. Increasing temperature softens the material and decreases the resistance to plastic flow, whereas increasing strain and strain rate harden the material and increase the resistance to plastic flow.

This model takes advantage of the deformation resistance parameter "s" in Anand's model, which is an internal scalar variable that describes the instantaneous

isotropic resistance to plastic flow. Monitoring this parameter allows the state of the material, and balance between hardening and softening, to be observed as deformation progresses. Figure 2.13 shows the results of Feng and Bassim for the evolution of the internal variable "s" as deformation progresses near the ASB and far away from it.

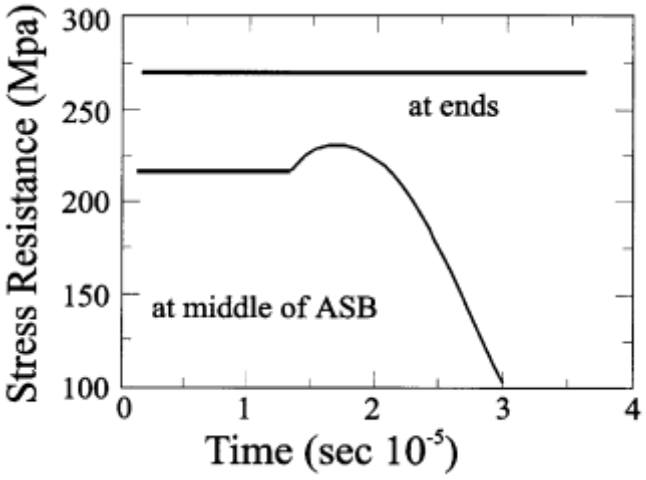

Figure 2.14: Stress resistance as a function of time for AISI 4340 steel at middle and far away from ASB. Used with permission from (Feng and Bassim, 1999)

Initially there is no rise in deformation resistance, this represents the early stages of deformation. At approximately $1.5(10)^{-5}$ s in the curve, an increase in resistance occurs. This region represents the initial strain hardening. Shortly past this point, the curve peaks and begins to decrease. The peak of this curve represents the point at which the material becomes unstable and the adiabatic heating has softened the material enough that the softening effects are now beginning to outweigh the hardening effects. Past this point, the material is softened severely and collapses along the shear band.

The shape of the deformed mesh (Figure 2.14) predicts the characteristic shape and localization during adiabatic shear band formation.

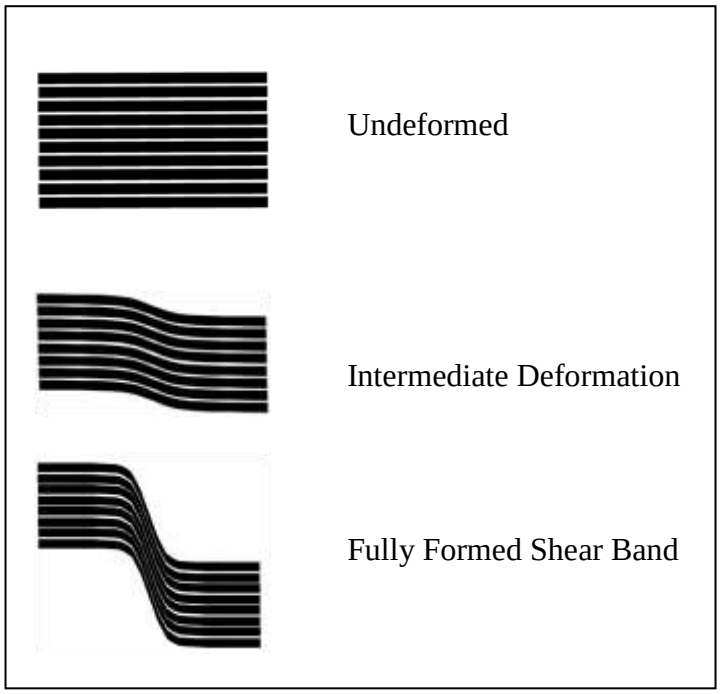

Figure 2.15: Deformed mesh showing evolution of shape of ASB. Adapted with permission from (Feng and Bassim, 1999)

Feng and Bassim predict the total temperature rise within the ASB to be approximately 200-250^{o}C for this particular steel (AISI 4340, tempered at 315^{o}C or 650^{o}C). This result agrees with the previously discussed issues surrounding the formation of transformed ASBs at temperatures below the austenizing temperature. The evolution of the predicted temperature rise at the centre of the ASB is shown in Figure 2.15.

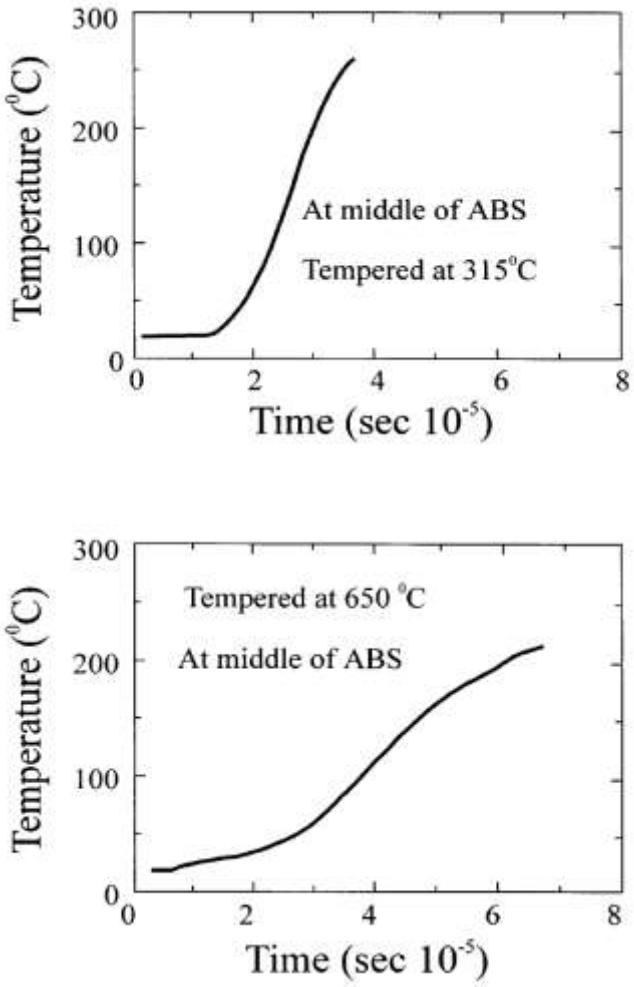

Figure 2.16: Simulated temperature rise in AISI 4340 steel, used with permission from (Feng and Bassim (1999))

Feng and Bassim accurately predict the timing for the onset of instability, the shape of the shear band, the effect of tempering temperature, and the total temperature rise at the site of localization. This model was applied to torsional behaviour, and has not yet been extended to include other stress states. The parameters for AISI 4340 steel were extrapolated from parameters obtained by Brown, Kim, and Anand (1989), which had

been fitted to experimental data representative of hot rolling of metal. These data were collected at high temperatures (above homologous temperatures of approximately 0.4) and maximum strain rates 1/s. Since the Anand model is highly non-linear, the extrapolated parameters may not reproduce the effects of strain hardening and strain rate sensitivity accurately. Previous work by the author has extended the work on the Feng and Bassim model and addressed the issue. He showed that the model holds for parameters fit from data for an armour steel, namely maraging steel (MARS) 300, supplied by the Canadian Department of National Defence.

The softening behaviour in the Feng-Bassim model is added to Anand's model by using a pair of exponentials of the form:

$$S_{new} = S_{old} \exp(-k\Delta T) \tag{2.17}$$

$$h_{new} = \frac{h_{old} \exp(-k\Delta T)}{(500|\Delta T|+1)^{0.3}} \tag{2.18}$$

These equations follow the evolution of the deformation resistance (s) and hardening coefficient (h) as the temperature increases, and "k" is a constant. This relationship is empirical and agrees with observed effects accurately for this particular steel, but it is difficult to extend this softening behaviour to other materials since the relationships (2.17) and (2.18) above are specific to steel. The form of the temperature dependency is not expected to be the same for materials of different crystal structure or composition.

2.3.2.2 Recent views on softening

It has been proposed by Rittel (2009) that the mechanism responsible for shear bands is not uncontrolled thermal softening, but the effect of stored elastic energy from cold work that causes dynamic recrystallization. This is further explored by Rittel and Osovski (2010) and explained using dislocation mechanics. The motivation for this, as mentioned previously, is that the observed temperature rise is nowhere near the temperatures required to soften materials to the extent observed in adiabatic shear bands. Dolinski, Rittel, and Dorogoy (2010) created a model of adiabatic shear band formation based upon this physical process. The results were found to agree well with the expected fracture path, temperature rise, local strains, and critical impact velocity required to initiate ASB.

This theme of dynamic recrystallization is incorporated into a model created by Medyanik, Liu, and Li (2007) which uses temperature as the driving mechanism (not stored elastic energy, as put forth by Rittel) to initiate shear bands. The model of Medyanik considers a general thermo-viscoplastic material (Johnson-Cook material) that softens once a critical temperature is reached. This model has been shown to work well for the prediction of the occurrence of ASBs in an FCC (OFHC copper) as well a BCC (4340 alloy steel) material, and adequately captures the speed of propagation and width of fully formed bands.

In conclusion, there is a lack of models of the evolution of adiabatic shear bands which are easy to implement and suitable for a range of geometries and materials. The model put forth by Feng and Bassim is sound and provides significant information about the initiation and evolution of adiabatic shear bands. This model has been shown to predict the behaviour of steel under torsion. However, the empirical nature of the softening term (k) and form of the softening equations (2.15) and (2.16) limits the applicability to other materials. The present work examines the extension of this model to two dimensions and introduces a physically motivated softening mechanism, based on the process of dynamic recrystallization, that may extrapolate more effectively to other materials. Anand's plasticity parameters are determined from experimental data for AISI 4340 steel under impact loading conditions.

CHAPTER 3: EXPERIMENTAL AND MODELLING PROCEDURES

This chapter describes the experimental (section 3.1) and modelling (section 3.2) procedures followed in the present work. The experimental section discusses the material under investigation (AISI 4340 alloy steel), specimen preparation, high strain rate testing procedures using a direct impact pressure bar, and interpretation of test data. The modelling section discusses the fitting of material model parameters and the finite element code, including temperature updating and shear localization programs.

3.1 Experimental Procedure

The experimental procedures described in this section include the preparation of specimens, testing procedures, and processing of data. The documentation and description of these procedures is especially important since the technique used, namely direct impact pressure bar testing, is very specialized and not widely used. For this reason, there are no standard operating procedures established and it is up to the experimenter to justify the validity and accuracy of the procedure.

3.1.1 Specimen Material, Geometry, and Preparation

The material selected for this investigation is a high strength alloy steel, namely AISI 4340. This steel is selected since it is commonly available and may be heat treated to a wide range of properties, including very high strength conditions. Applications where impact properties are important often use AISI 4340 (for example, moving parts on heavy machinery), making it an excellent candidate for modelling adiabatic shear bands in real world design problems.

The principal alloying elements in AISI 4340 are nickel, chromium, and molybdenum. Additional specifications are shown in Table 3.1.

Table 3.1: Constituents of AISI 4340 steel (SAE J404)

Element	Weight %
Chromium	0.70-0.90
Nickel	1.65-2.00
Molybdenum	0.20-0.30
Carbon	0.38-0.43
Manganese	0.60-0.80
Phosphorous	< 0.035
Sulfur	< 0.04
Silicon	0.15-0.30
Iron	Balance

The steel is supplied in the normalized condition as 3/8 inch (9.35 mm) nominal diameter rods.

The steel rod is cut into 9.5 mm plugs, providing a length to diameter ratio of approximately 1:1. This geometry has been shown to work well during previous direct impact experiments conducted at the University of Manitoba ((Bassim and Panic 1999), Nazimuddin (2010), (Odeshi et al. 2006)). A schematic of the specimen geometry appears in Figure 3.1.

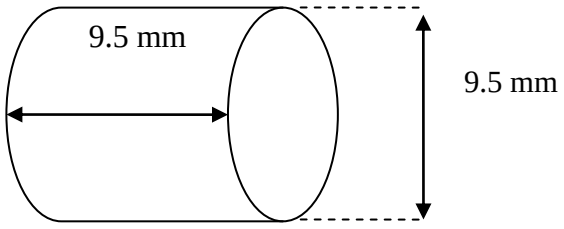

Figure 3.1: Direct impact specimen geometry

The specimens are cut using a miter saw equipped with an abrasive cutting wheel, commonly known as a "hot saw". A fixture is used to hold the bar in place during cutting to ensure that the cuts are repeatable, homogenous, and safe. An image of the fixture appears in Figure 3.2.

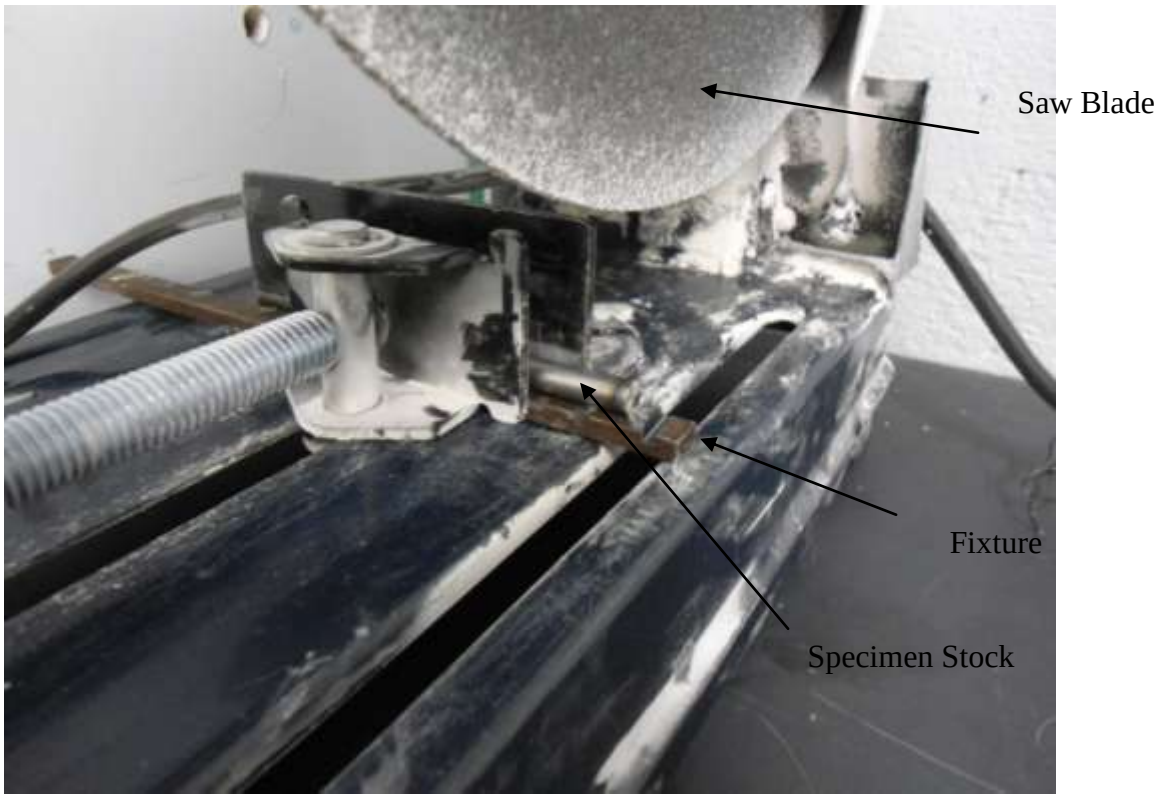

Figure 3.2: Abrasive saw and jig holding specimen for cutting

The edges of the specimens are de-burred and the faces are ground flat using a bench grinder with fine and coarse abrasive wheels. A photograph of a finished specimen prior to heat treatment appears in Figure 3.3.

Figure 3.3: Photograph of a finished specimen prior to heat treatment

Heat treatment is essential to the preparation of the specimens to ensure homogenous and controlled material properties. This stage removes any of the microstructural damage incurred as a result of the abrasive cutting and grinding operations. Heat treatment is accomplished using a furnace designed and built by the author, shown in Figure 3.4.

Figure 3.4: Furnace interior (left) and exterior, showing control box (right)

The furnace uses PID control to adjust the temperature and features programmable heat treatment schedules, including ramp and soak stages. This ensures that the temperature is closely controlled and the timing is consistent between batches.

Specimens were austenized at 860^{o}C for 20 minutes, followed by a quench in water. After the quench, specimens were tempered for 2 hours at 550^{o}C. The heating schedule is summarized in Figure 3.5.

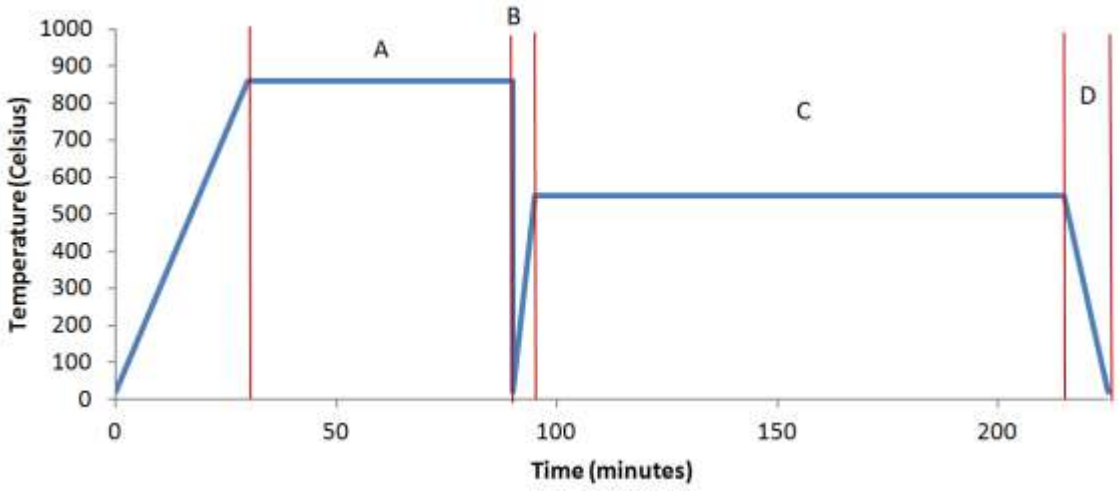

Figure 3.5: Heat treatment schedule for cylindrical AISI 4340 impact specimens.

After an initial ramp-up time of 20 minutes, 'A' is the austenizing stage at 860^{o}C (30 min), 'B' is the quench, 'C' is the tempering at 550^{o}C (90 min), and 'D' is air cooling (approximately 5-10 minutes).

3.1.2 Impact Testing

Impact testing was carried out using a direct impact pressure bar (DIPB). The arrangement was developed at the University of Manitoba and used for testing materials at very high strain rates and large strains (Odeshi et al. (2006), Nazimuddin (2010), Boakye -Yiadom (2011)).

The apparatus consists of a long elastic bar made from high strength steel (AISI 4340) and measures 1.525 m long by 38 mm (1.5 inches) in diameter. The specimen is positioned on the face of the pressure bar and the projectile impacts the specimen directly. The projectile measures 0.222 m long and has the same diameter as the pressure bar (38 mm). The projectile is made of the same high strength steel as the pressure bar. A photograph of the system is shown in Figure 3.6.

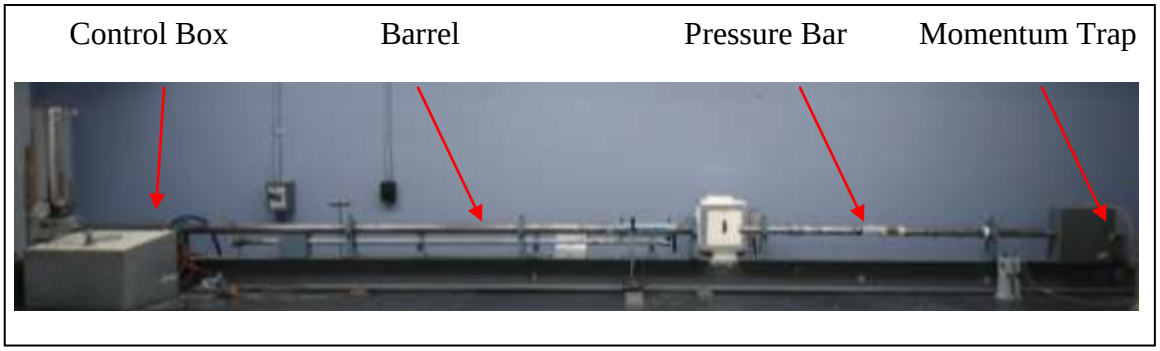

Figure 3.6: Photograph of the direct impact pressure bar

3.1.3 Strain Measurement

Strain gages mounted on the pressure bar measure the stress-time information in the specimen and this data is recorded using a digital oscilloscope (Figure 3.7).

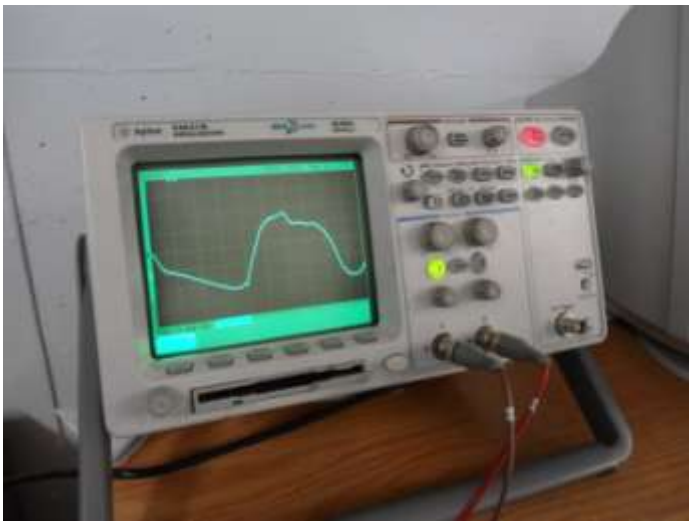

Figure 3.7: Recorded strain signal on digital oscilloscope during testing

A full bridge strain gage configuration is selected to improve signal quality for this test. Four strain gages spaced equally around the perimeter of the bar, with adjacent gages being perpendicular, allow for the rejection of bending strains and improved sensitivity to axial strains (by a factor of $2(1+\nu)$, where ν is Poisson's ratio). The schematic showing the configuration of the strain gages appears in Figure 3.8, with axially oriented gages labeled "ε" and perpendicular gages labeled "-νε". To improve the signal to noise ratio, remote excitation is used to remove lead wire effects and all cables from the signal amplifier to the strain gages on the bar are shielded.

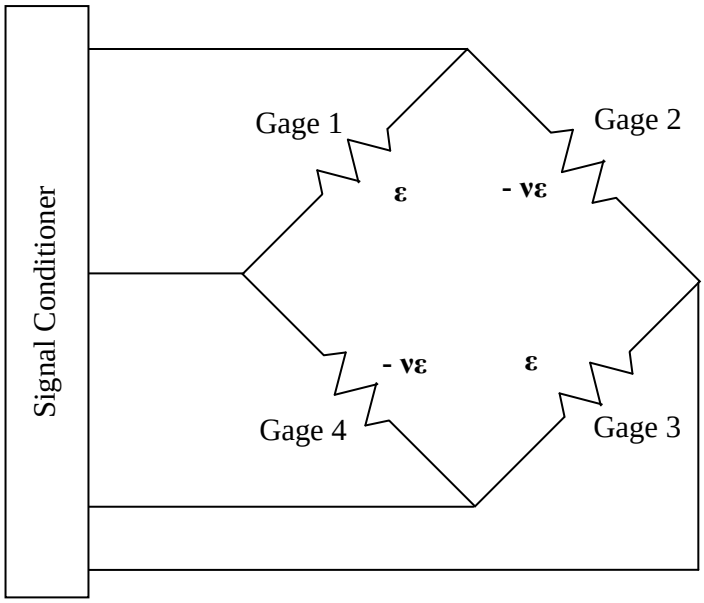

Figure 3.8: Full bridge (axial) strain gage wiring

3.1.4 Bar Calibration

Bar calibration includes determining the strain-voltage relationship for the apparatus and the elastic properties of the bar (wave speed, elastic modulus). These calibrations ensure that the calculations of specimen stress/strain curves are as accurate as possible.

For a full bridge arrangement, the strain-voltage relationship, $\epsilon(V_r)$, is found as:

$$\epsilon = -\frac{2V_r}{GF[(\nu+1)-V_r(\nu-1)]} \tag{3.1}$$

Where V_r is the ratio of excitation voltage to output voltage, GF is the gage factor, and ν is Poisson's ratio for the steel bar.

The strain-voltage relationship is then simplified to:

$$\epsilon(t) = k \cdot V(t) \tag{3.2}$$

where k is a constant (units of $1/mV$) calculated from the gage factor, excitation voltage, and Poisson's ratio of the steel bar.

Wave speed was measured by examining the time between successive reflections within the bar. A single reflection is shown in Figure 3.9. The initial wave detected by the strain gages is in compression (negative voltage) and its reflection is in tension (positive voltage). The length of time between peaks is the time required to travel one lap of the bar, or twice the bar length.

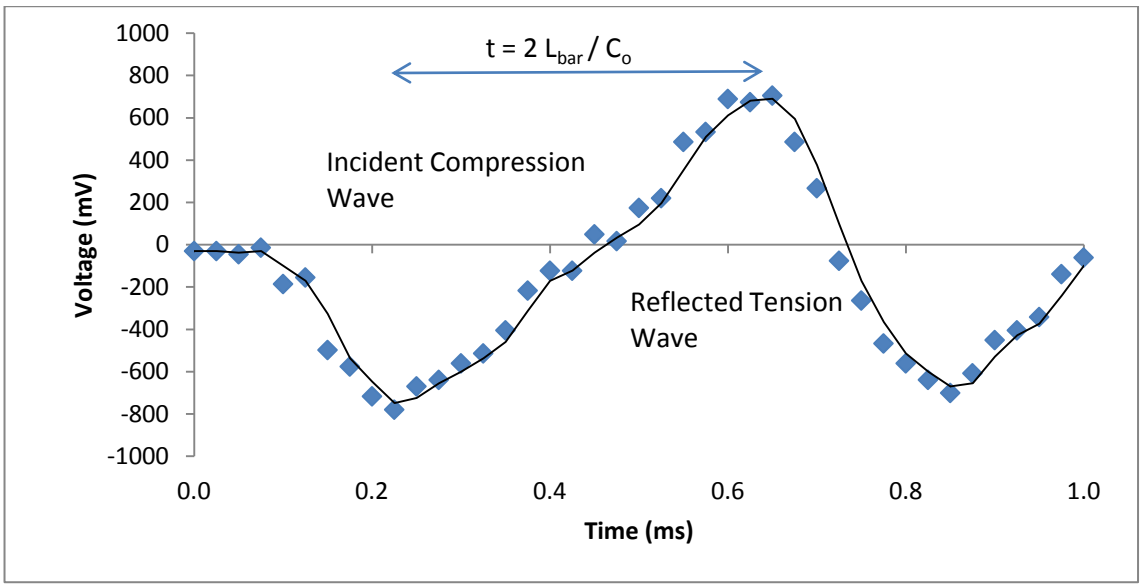

Figure 3.9: Single Reflection of an elastic wave in the pressure bar

An accurate measurement of the time was obtained by recording the average distance over a very large number of reflections by taking the Discrete Fourier Transform

(DFT) of a large number of reflections (Figure 3.10) and extracting the primary frequency component (Figure 3.11).

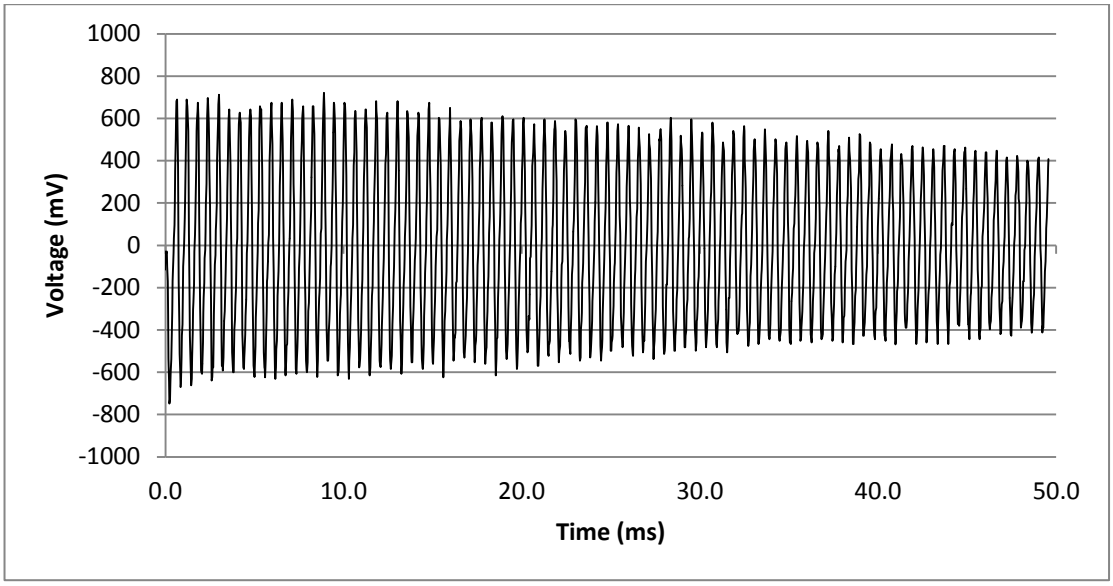

Figure 3.10: Reflections of an elastic wave within the pressure bar

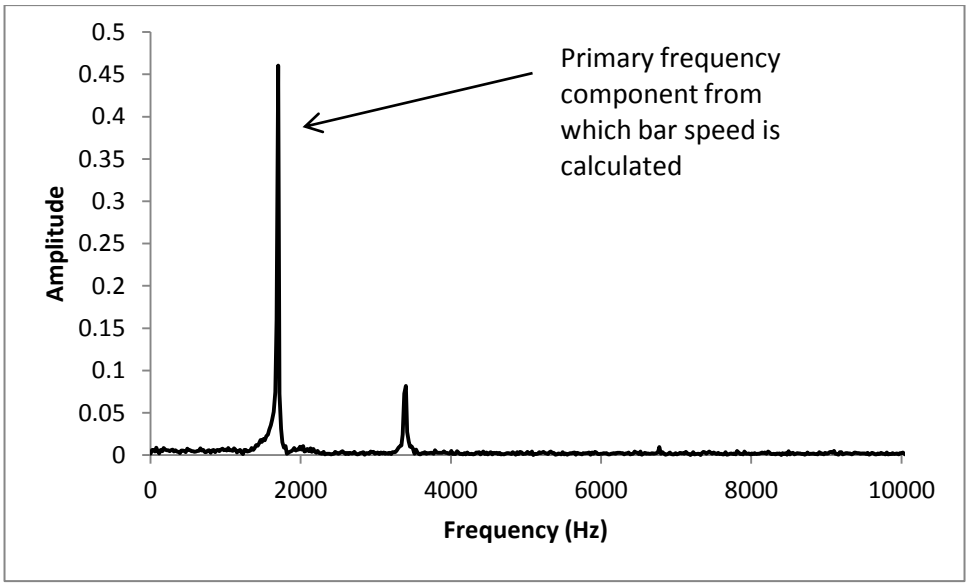

Figure 3.11: Single sided amplitude spectrum of voltage

Bar speed (C_o) is calculated from the primary frequency component (f) as:

$$C_o = 2L_{bar}f \tag{3.3}$$

The dynamic elastic modulus is then calculated as:

$$C_o = \sqrt{\frac{E}{\rho}}\ ;\ E = C_o^2\rho \tag{3.4}$$

3.1.5 Stress-Strain Calculations

The strain-time data, obtained previously using equation (3.2), was converted to force-time. It is assumed that the stress in the elastic bar is purely longitudinal, so it follows that:

$$F(t) = \epsilon(t) \cdot (EA)_{bar} \tag{3.5}$$

Where F(t) is the force-time data, $\epsilon(t)$ is the strain-time data from the elastic bar, and $(EA)_{bar}$ is the product of elastic modulus and cross sectional area for the elastic bar.

A force balance is taken at the bar-specimen interface, and the stress is calculated by assuming a uniaxial state of stress within the specimen.

$$\sigma_s(t) = \frac{F(t)}{A_s(t)} \tag{3.6}$$

Where subscript "s" refers to the specimen.

From this point, the data is processed in two ways. The first method is referred to as a the "nominal" stress-strain curve, and the second method is referred to as the "constant strain rate" curve. The nominal curve allows for an overall view of the stress-

strain data, and is useful for comparing the stress at very large strains; the constant strain rate curve is used for fitting experimental data to the numerical model.

3.1.5.1 Nominal Strain-Time Calculation

Assuming the specimen is incompressible and deforms uniformly, specimen area A_s is related to the length $L(t)$ and the original geometry (A_i, L_i) according to:

$$A_s(t) = \frac{A_i L_i}{L(t)} \tag{3.7}$$

Where the length is assumed to be related to the time linearly,

$$L(t) = L_i - \frac{L_i - L_f}{t_f} t_s \tag{3.8}$$

Then final specimen stress as a function of strain is then obtained as:

$$\sigma(t) = [\varepsilon_t(t)] \frac{EA\left[L_i - (L_i - L_f)\,(t/t_f)\right]}{A_i L_i} \tag{3.9}$$

$$\varepsilon(t) = \ln\left(\frac{L_i}{L_i - (L_i - L_f)\frac{t}{t_f}}\right) \tag{3.10}$$

Where $\varepsilon_t(t)$ is the recorded strain-time data from the elastic pressure bar, EA are the modulus and area of the elastic pressure bar, and t_f is the total time of the impact event.

3.1.5.2 Constant Strain Rate Calculations

The second method used to calculate strain rate is used to obtain constant strain rate data from the direct impact results. This method calculates specimen strain by using the mechanical impedance to characterize the response of the elastic bars. From the impedance and a known function of force (from the strain gage), the motion of the ends of the rods is calculated as:

$$l(t) = l_o - v_o t + \left(\frac{1}{Z_1 A_1} + \frac{1}{Z_2 A_2}\right) \int_0^t f(t')dt' \tag{3.11}$$

Where $l(t)$ is the specimen length, v_o is the impact velocity, Z is mechanical impedance, A is cross sectional area, and the subscript 1 and 2 represent projectile and elastic bar respectively.

For two bars of the same cross section and material, this relationship simplifies to:

$$l(t) = l_o - v_o t + \left(\frac{2}{Z_1 A_1}\right) \int_0^t f(t')dt' \tag{3.12}$$

This approach is necessary since the plasticity model (discussed in section 3.2) requires constant strain rate data for curve fitting. The constant strain rate portion of the direct impact test is only up to the point where the elastic compression wave has travelled from the impact end to the striker bar, reflected from the free end, and returned to the face. Past this point, the strain rate is significantly diminished due to the mechanical impedance mismatch between striker and specimen. The time where constant strain rate is valid, $t_{\dot{e}}$, is therefore $0 < t_{\dot{e}} < C_o(2l)$, where C_o is the bar speed of the elastic striker and l is the length of the striker bar.

3.1.6 High Temperature Fixture

During direct impact tests, specimens are typically held in place with a thin layer of grease at the specimen-bar interface. This becomes impractical for specimens at elevated temperatures, since the grease would not remain viscous enough to hold the specimen in place. A special fixture was constructed which holds the specimen and also allows it to be transferred from the furnace to impact site in a repeatable and safe manner. This fixture is shown in Figure 3.12 and Figure 3.13.

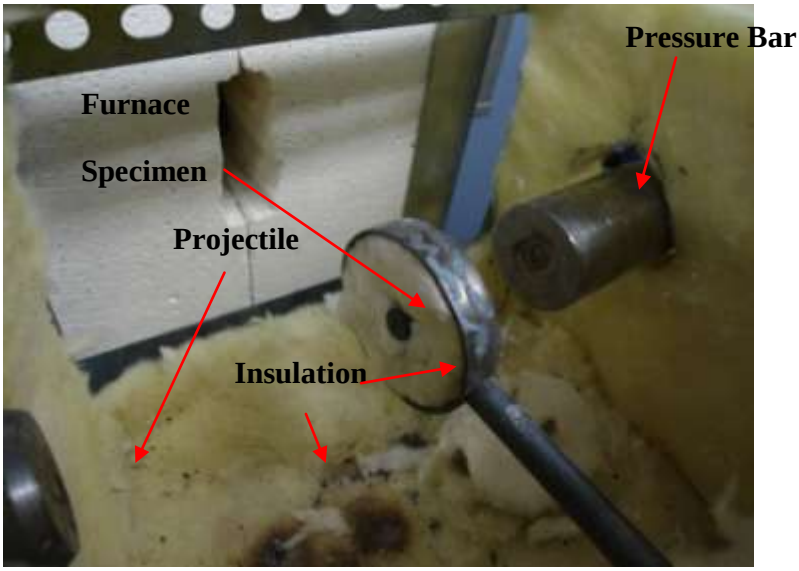

Figure 3.12: High temperature fixture (retracted position for loading/firing)

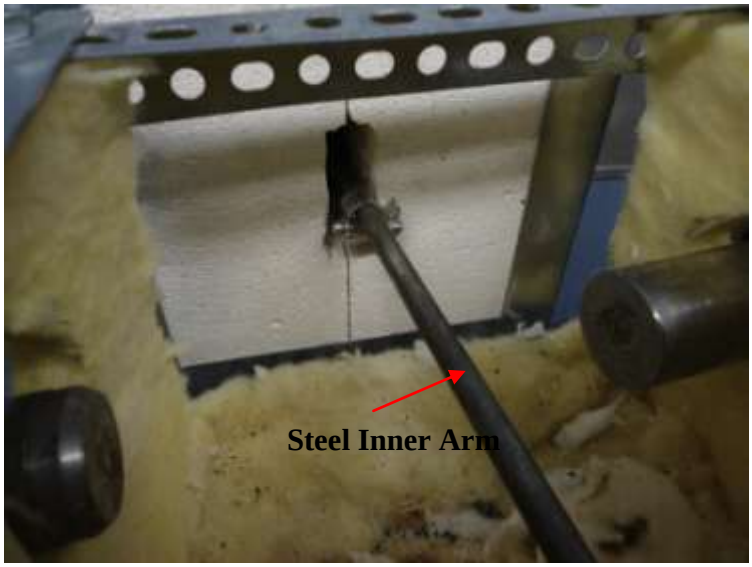

Figure 3.13: High temperature fixture (heating position with specimen in furnace for heating)

The fixture consists of an outer steel cage, a steel inner arm, and a steel specimen ring. The specimen arm slides in an aluminum guide tube of slightly larger inside diameter than the diameter of the inner arm.

The specimen is held in place in the specimen ring using a circular piece of mineral wool with a hole drilled through the centre. The mineral wool serves two purposes, namely thermal insulation and structural support. The insulative properties of the mineral wool protect against heat loss to the atmosphere from the heated specimen, which lengthens the time allowed outside of the furnace, and helps keep the specimen at a more uniform temperature at the time of impact. The structural properties allow the specimen to be held securely in place while still being soft enough to prevent radial constriction of the specimen or interfere with the projectile. The loading procedure for the specimen is shown in Figure 3.14.

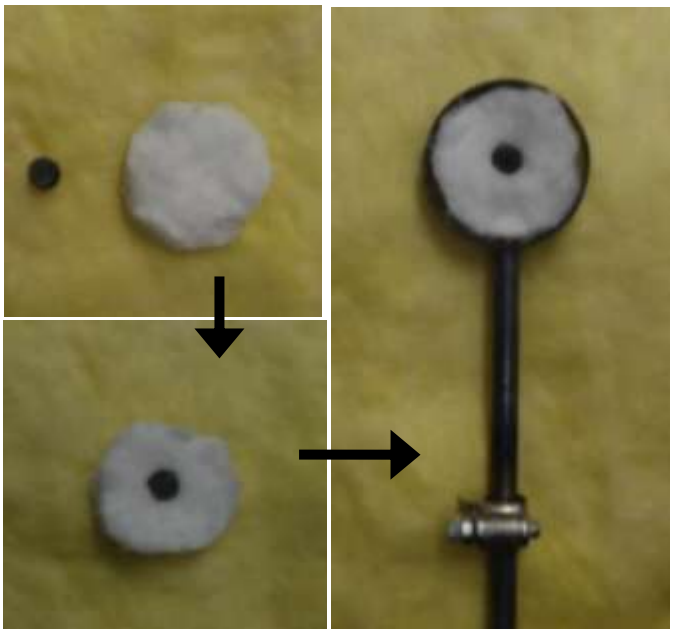

Figure 3.14: Loading specimen into fixture arm

In order to know how long the specimen must remain in the furnace before reaching a uniform temperature, a dummy specimen (shown in Figure 3.15) is equipped with a thermocouple and placed in the furnace using the testing fixture arm.

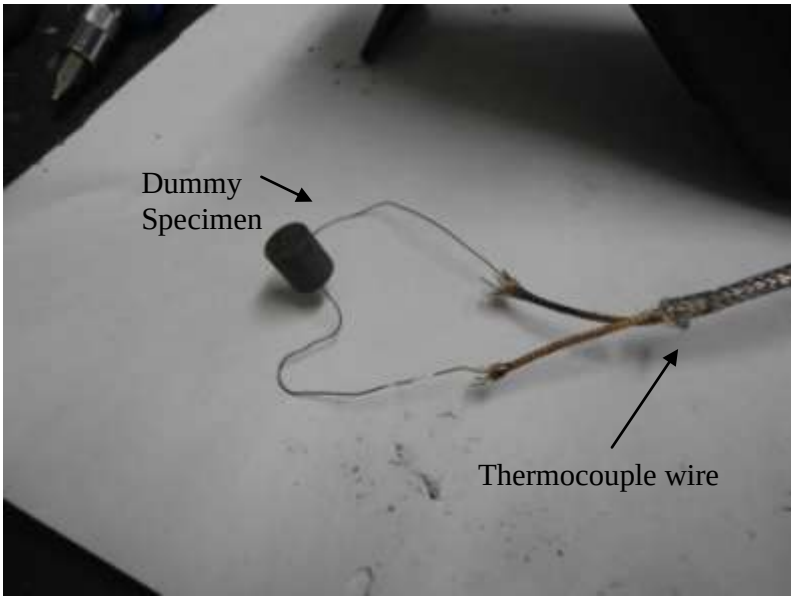

Figure 3.15: Dummy specimen with thermocouple

Mounting of the thermocouple was achieved by first annealing the specimen for easier machining. A 1/16" hole was drilled along the longitudinal axis of the specimen to a depth of approximately 6 mm to accept the end of a thermocouple probe. The twisted end of a K type thermocouple was threaded into the specimen until it is held securely. The end of the thermocouple wires were attached to a digital multimeter with maximum resolution of 1mV. A stopwatch was started and the time was recorded each time the multimeter advances.

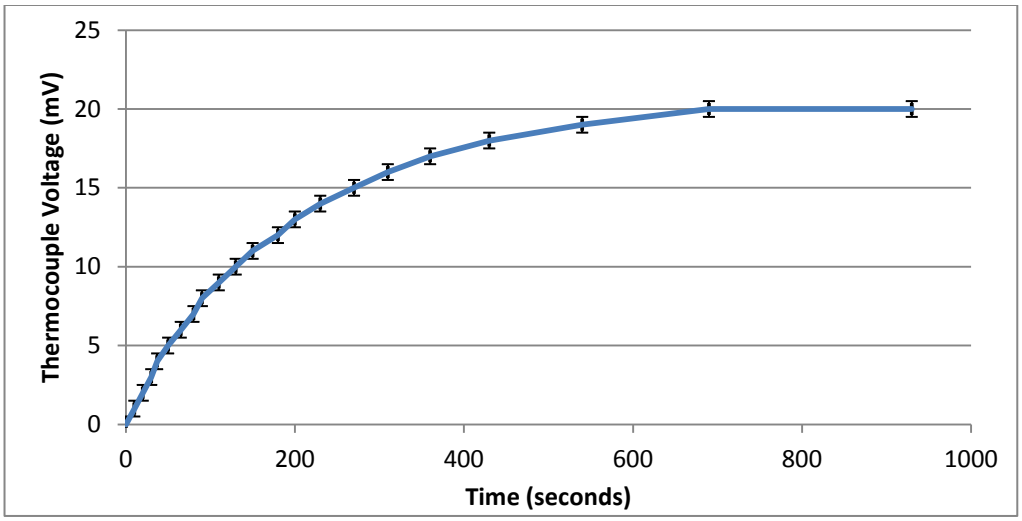

Figure 3.16: Heating curve for specimen to 500^{o}C

The cooling curves are also of interest, since it is important to know how fast the specimen will cool down once removed from the furnace. An acceptable rate of cooling here is assumed to be 1mV (12^{o}C) per 10 seconds.

The cooling curve for the specimen after being removed from the furnace is shown in Figure 3.17, and the portion of this curve from 0 to 60 seconds is shown in Figure 3.18. Error bars indicate the maximum resolution of the multimeter.

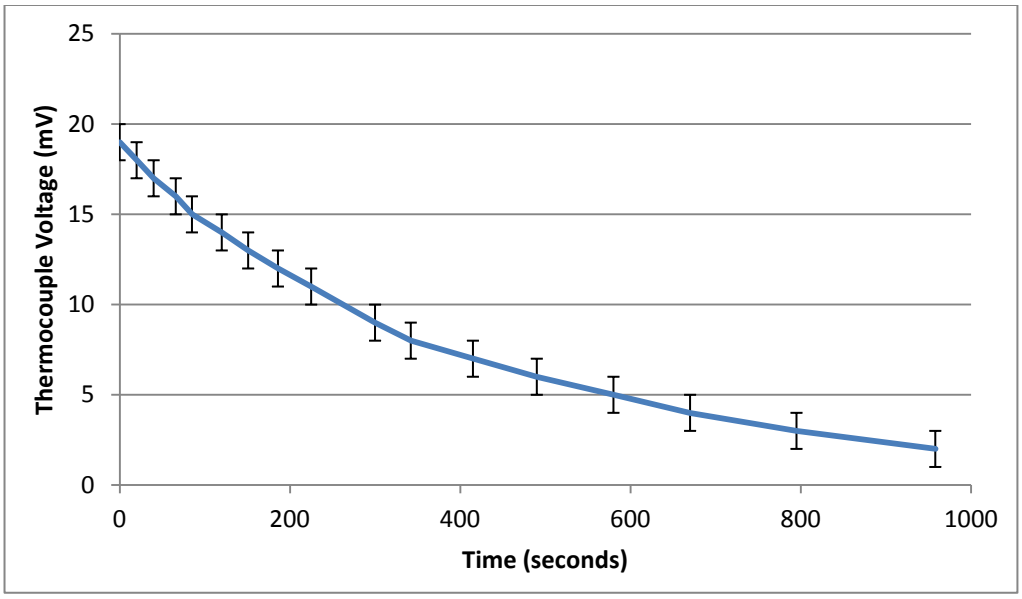

Figure 3.17: Cooling curve for specimen from 500°C to room temperature

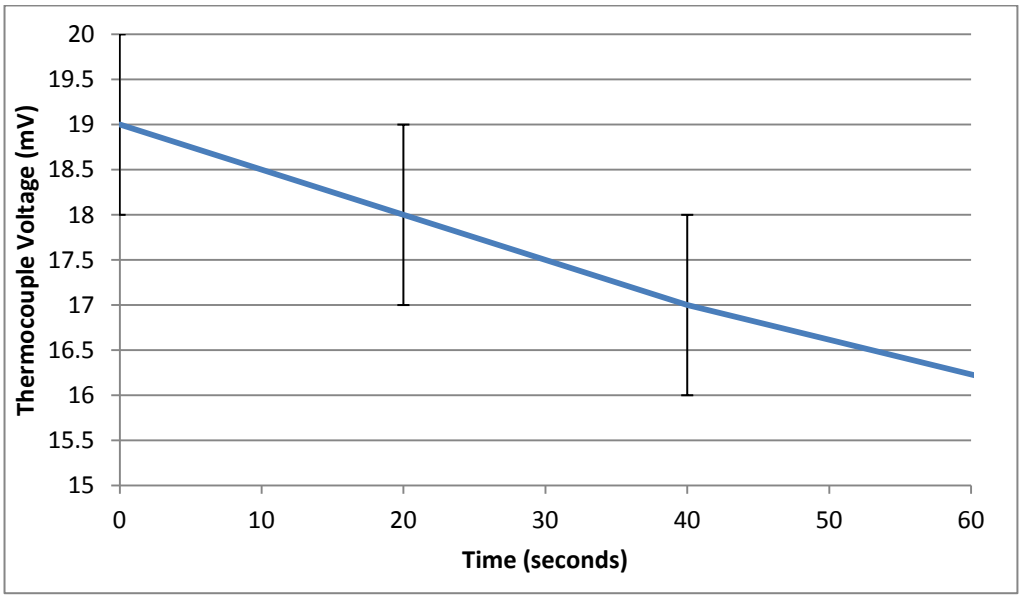

Figure 3.18: Close-up of cooling curve for specimen from 500°C for first minute removed from furnace.

From Figure 3.18, to cool by 1mV (12^{o}C) at 500^{o}C requires a time of approximately 10 seconds, which is sufficiently long as to allow for removal and impacting of the specimen.

3.1.7 Testing Protocol

To quantify the rate and temperature dependent plastic behaviour of the specimen, three impact velocities and three temperatures are tested, from 17 to 35 m/s and 20^{o}C to 550^{o}C. These ranges are selected to cover the anticipated conditions up to the formation of ASBs. A summary of the approximate testing conditions appears in Table 3.2. A minimum of 3 trials are conducted for each group to ensure that the results are repeatable.

Table 3.2: Testing protocol

Firing Pressure/Temperature	**20^{o}C**	**300 ^{o}C**	**550 ^{o}C**
50kPa	Group 1	Group 2	Group 3
100kPa	Group 4	Group 5	Group 6
200kPa	Group 7	Group 8	Group 9

The method for testing a specimen using the fixture is outlined below:

1. Preheat furnace and hold at desired temperature for 10 minutes, to ensure a homogenous temperature is reached inside.
2. Slide the specimen arm into the furnace through the rectangular opening in the furnace door.
3. Heat for 10 minutes
4. Retract projectile and charge
5. Remove specimen and align with face of pressure bar
6. Cover top to reduce amount of flying debris
7. Fire projectile and capture signal using oscilloscope.

The data recorded by the oscilloscope was then processed using the methods outlined previously in this chapter to obtain stress-strain curves. These curves were then analyzed and used to fit the material models to implement the Feng and Bassim model, and used to predict the impact behaviour of the material. The procedures for the numerical steps are described in the following chapter.

3.2 Modelling Procedures

3.2.1 Outline of the Program

The stress-strain curve for a material exhibiting ASBs appears differently depending on whether the material is within the localized region or outside. Outside the localized region, the material behaves as a standard homogenous thermo-viscoplastic material with strain hardening and thermal softening. Inside the shear band, local processes such as dynamic recrystallization result in softening beyond what is predicted by the homogenous material properties. To describe this behaviour, it is necessary to define two separate stress-strain relationships, namely homogenous and localized.

Both homogenous and localized stress-strain relationships are described using Anand plasticity model, which was the model originally adapted to high strain rate used by Feng and Bassim. Anand's model is a general purpose thermo-viscoplasticity model. The variables describing the state of the material are the Cauchy stress tensor (**T**), the isotropic deformation resistance (s), and the absolute temperature (θ).

The Anand plasticity model consists of three constitutive relations that describe the evolution of each variable: the rate relation, the flow rule, and the evolution equation. A more detailed description of the mathematics of this model may be found in Anand's original paper on the subject (Anand, 1984).

1) The "rate stress-strain-temperature" relation:

$$\widetilde{\boldsymbol{T}}^{\boldsymbol{\nabla}} = £[\boldsymbol{D} - \boldsymbol{D}^{\boldsymbol{p}}] - \boldsymbol{\Pi}\dot{\theta} \qquad (3.5)$$

Where,

$\widetilde{\boldsymbol{T}}^{\nabla} = \dot{\boldsymbol{T}} - \boldsymbol{W}\boldsymbol{T} + \boldsymbol{T}\boldsymbol{W}$	Jaumann derivative of Cauchy stress (**T**)	(3.6)
$\mathfrak{L} = 2\mu\boldsymbol{I} + \left\{\kappa - \frac{2}{3}\mu\right\}\mathbf{1}\otimes\mathbf{1}$	Fourth order isotropic elasticity tensor	(3.7)
$\mu = \hat{\mu}(\theta)$	Elastic shear modulus	(3.8)
$\kappa = \hat{\kappa}(\theta)$	Elastic bulk modulus	(3.9)
$\boldsymbol{\Pi} = (3\kappa\alpha)\mathbf{1}$	Stress-temperature tensor	(3.10)
$\alpha = \hat{\alpha}(\theta)$	Coefficient of thermal expansion	(3.11)
$\boldsymbol{L} = \nabla\boldsymbol{v}$	Spatial gradient of the velocity	(3.12)
$\boldsymbol{D} = sym(\boldsymbol{L})$	Stretching tensor	(3.13)
$\boldsymbol{W} = skew(\boldsymbol{L})$	Spin tensor	(3.14)
$\boldsymbol{I} =$	Fourth order identity tensor	(3.15)
$\mathbf{1} =$	Second order identity tensor	(3.16)

2) The constitutive equation for the plastic stretching tensor, $\boldsymbol{D^p}$, is called the "flow rule":

$$\boldsymbol{D}^p = \dot{\epsilon}^p \left\{3\,\frac{\widetilde{\boldsymbol{T}}'}{2\tilde{\sigma}}\right\};\ \boldsymbol{W}^p = 0 \qquad (3.17)$$

$\dot{\epsilon}^p = f(\tilde{\sigma}, s, \theta) > 0$, when $\tilde{\sigma} > 0$ Equivalent plastic strain rate (3.18)

$\boldsymbol{T}'$ Deviator of the Cauchy stress tensor (3.19)

$$\tilde{\sigma} = \sqrt{\frac{3}{2}\boldsymbol{T}' \cdot \boldsymbol{T}'} \quad \text{Equivalent tensile stress} \quad (3.20)$$

Where a functional form of the flow rule is:

$$\dot{\epsilon}^p = A \exp\left(-\frac{Q}{R\theta}\right)\left[\sinh\left(\xi\frac{\tilde{\sigma}}{s}\right)\right]^{\frac{1}{m}} \quad (3.21)$$

3) The evolution equation for the scalar isotropic resistance to stress, or simply "evolution equation" is of the form:

$$\dot{s} = h(\bar{\sigma}, s, \theta)\dot{\epsilon}^p - \dot{r}(s, \theta) \quad (3.22)$$

Where h and $\dot{r}$ represent dynamic or static contributions to hardening/recovery respectively.

A functional form of the evolution, as suggested by Brown, Kim, and Anand (1989), is given as:

$$\dot{s} = \left\{h_o \left|\left(1 - \frac{s}{s^\star}\right)\right|^a \text{sign}\left(1 - \frac{s}{s^\star}\right)\right\} \dot{\epsilon}^p \quad (3.23)$$

With $$s^\star = \tilde{s}\left[\frac{\dot{\epsilon}^p}{A}\exp\left(\frac{Q}{R\theta}\right)\right]^n \quad (3.24)$$

The temperature dependence of stress is accounted for by an Arrhenius style exponential term in (3.24).

These constitutive equations are implemented in ANSYS by defining a set of 9 parameters, described in Table 3.3.

Table 3.3: Anand plasticity parameters

Parameter	**Meaning**	**Units**
s_0	Initial value of deformation resistance	Stress (MPa)
$\frac{Q}{R}$	Q = activation energy	kJ / mol
	R = universal gas content	kJ / (mol - °K)
A	Pre-exponential factor	1 / s
ξ	Multiplier of stress	dimensionless
m	Strain rate sensitivity of stress	dimensionless
h_o	Hardening/softening constant	Stress (MPa)
$\hat{s}$	Coefficient for deformation resistance saturation value	Stress (MPa)
n	Strain rate sensitivity of saturation	dimensionless
a	Strain rate sensitivity of hardening or softening	dimensionless

Each state of the material (homogenous or localized) is described by a set of these 9 parameters, with the transition from homogenous to localized occurring at a pre-determined temperature of $0.4T_m$. This transition is made possible in ANSYS by using material data tables that define material parameters as a function of temperature. By creating a data table that has uniform parameters (homogenous) up to the point of instability, the data table acts as a switch that converts between regions of homogenous and localized behaviour once a critical temperature is reached. This process is outlined in Figure 3.19 below.

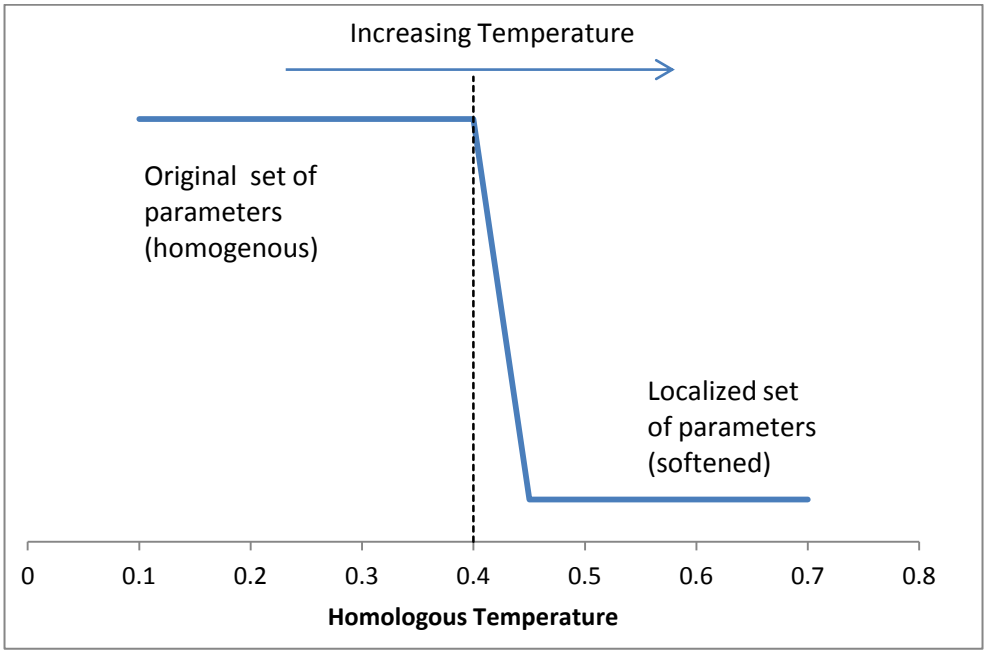

Figure 3.19: Switch between sets of material plasticity parameters at a critical temperature

The homogenous properties were obtained from the experimental results described in section 3.1, and the localized properties were obtained from the homogenous properties by decreasing the deformation resistance term to represent loss of structural integrity. These steps are outlined in Figure 3.20.

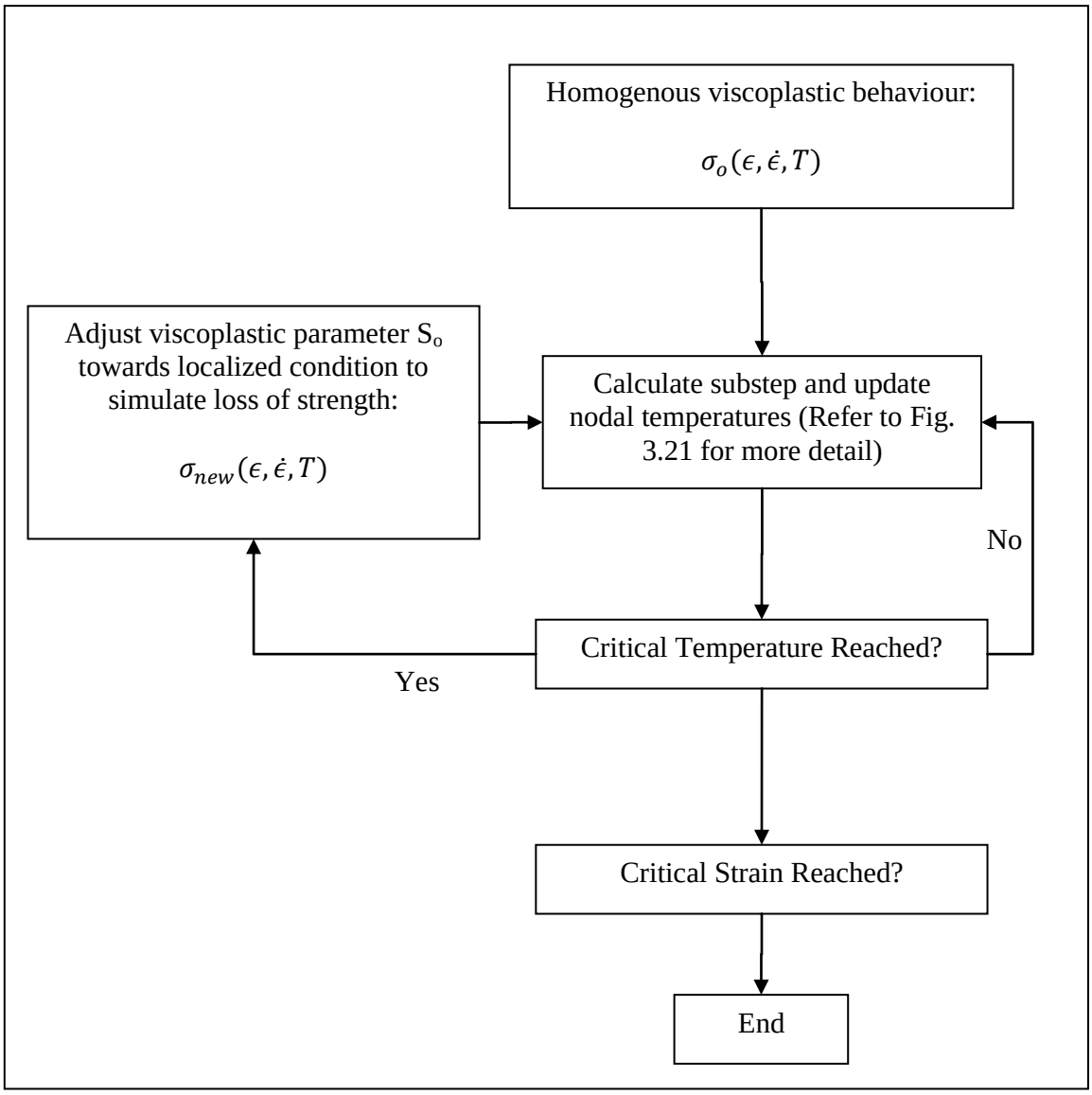

Figure 3.20: Program outline for switching from homogenous to localized condition

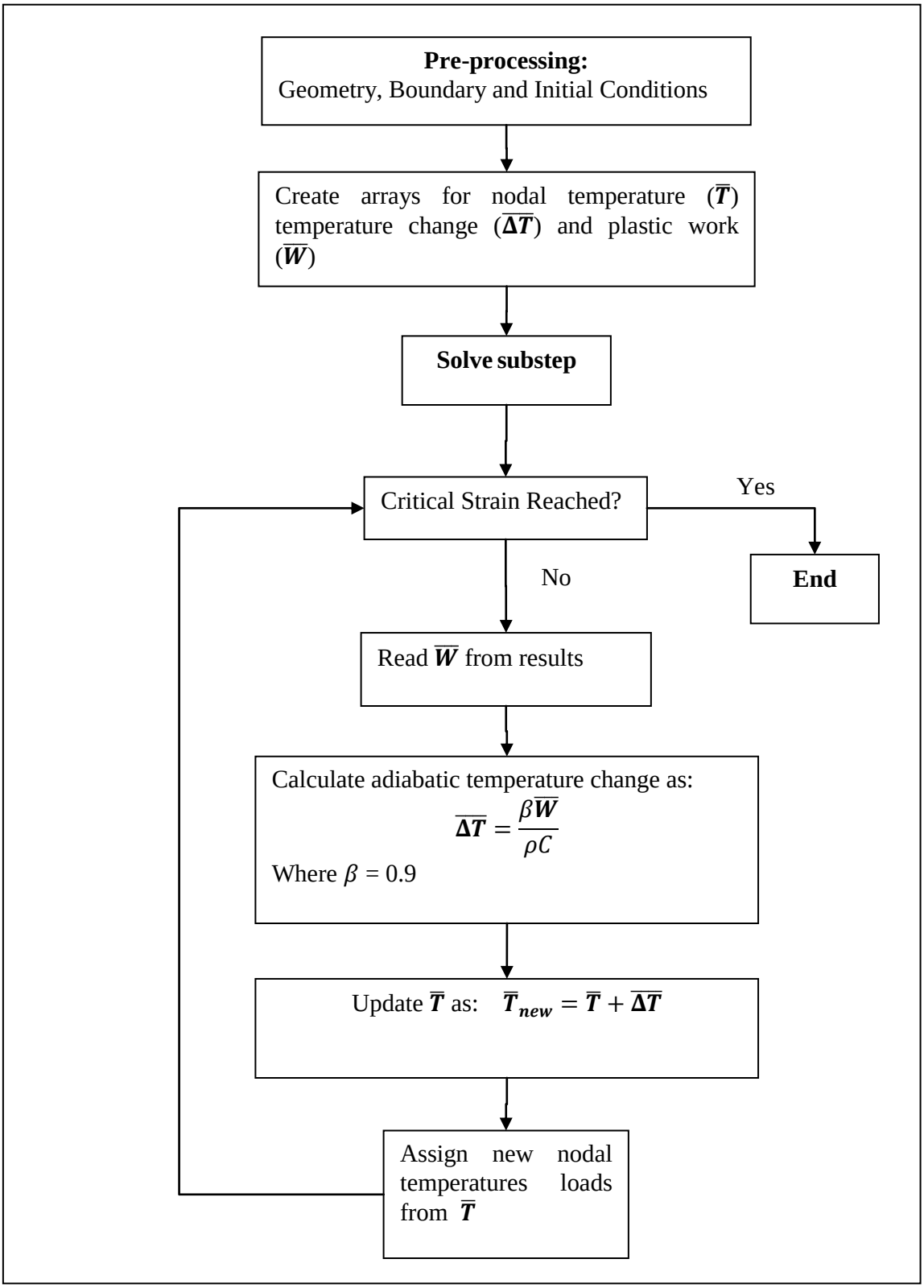

Figure 3.21: Flowchart for temperature evolution

3.2.2 Fitting Material Parameters to Experimental Data

The estimation of homogenous material parameters was achieved by linear and non-linear least squares regression of experimental stress-strain data to equations (3.25) and (3.26):

$$\sigma^*(\theta, \dot{\varepsilon}_p) = \left(\frac{\hat{s}}{\xi}\right)\left[\frac{\dot{\varepsilon}_p}{A} e^{\frac{Q}{R\theta}}\right]^n sinh^{-1}\left[\frac{\dot{\varepsilon}_p}{A} e^{\frac{Q}{R\theta}}\right]^m \tag{3.25}$$

$$\sigma = \sigma^* - \left[(\sigma^* - \sigma_o)^{\frac{1}{1-a}} + (a-1)\{ch_o(\sigma^*)^{-a}\}\dot{\varepsilon}_p\right]^{\frac{1}{1-a}} \tag{3.26}$$

Beginning with stress-strain data from a variety of strain rates and temperatures, the stress-plastic strain curves, (σ, ϵ^p), were generated.

Saturation stress, $\sigma^\star$, was determined directly from the (σ, ϵ^p) data by observing where on the plot the stress plateaus. If there was no plateau observed in the data, then curves for $(\sigma, d\sigma/d\epsilon^p)$ are extrapolated to $\frac{d\sigma}{d\epsilon^p} = 0$.

Parameters $a, ch_o,$ and σ_0 were determined by a least squares fit of the stress-plastic strain data to the integrated stress-strain relation (3.26).

$$\sigma = \sigma^* - \left[(\sigma^* - \sigma_o)^{\frac{1}{1-a}} + (a-1)\{ch_o(\sigma^*)^{-a}\}\dot{\varepsilon}_p\right]^{\frac{1}{1-a}} \tag{3.26}$$

Parameters A, $\frac{Q}{R}$, m, n, and $\frac{\hat{s}}{\xi}$ were determined by a non-linear least squares fit of the experimental data to the saturation stress relation (3.25).

$$\sigma^*(\theta, \dot{\varepsilon}_p) = \left(\frac{\hat{s}}{\xi}\right)\left[\frac{\dot{\varepsilon}_p}{A} e^{\frac{Q}{R\theta}}\right]^n sinh^{-1}\left[\frac{\dot{\varepsilon}_p}{A} e^{\frac{Q}{R\theta}}\right]^m \tag{3.25}$$

The parameter for the stress multiplier, ξ, was determined from (3.27) using the values of A, Q, and m determined previously by forcing $c < 1$ in each experimental data set.

$$c \equiv \frac{1}{\xi} \sinh^{-1}\left[\left\{\frac{\dot{\varepsilon}^p}{A} \exp\left(\frac{Q}{R\theta}\right)\right\}^m\right] \tag{3.27}$$

The value for h_o (work hardening coefficient) is the average of the combined ch_o term that was fitted above.

$$h_o = \frac{\left(\sum \frac{ch_o}{c}\right)}{q} \tag{3.28}$$

Finally, the initial value for the average isotropic deformation resistance (s_o) was evaluated by factoring out the constant, c, from the term $c\sigma_o$ determined above.

The Anand parameters for the material in the softened state were obtained by scaling down the saturation stress from equation 3.25 as:

$$\sigma_s{}^*\left(\theta, \dot{\varepsilon}_p\right) = \left(\frac{\hat{s}_s}{\xi}\right)\left[\frac{\dot{\varepsilon}_p}{A} e^{\frac{Q}{R\theta}}\right]^n \sinh^{-1}\left[\frac{\dot{\varepsilon}_p}{A} e^{\frac{Q}{R\theta}}\right]^m \tag{3.29}$$

Where σ_s^* and $\hat{s}_s$ are respectively the saturation stress and the coefficient of saturation stress of the material undergoing dynamic recrystallization.

All non-linear curve fitting was accomplished iteratively using the Levenberg-Marquardt algorithm, which minimizes the chi-squared value to find the best fit. Chi-

squared quantifies the amount of variation between the fitted curve and the experimental data points defined as:

$$\chi^2 = \sum_{i=1}^{n} w_i[Y_i - f(x_i, \boldsymbol{\theta}]^2 \quad (3.29)$$

Where w is the weight function, Y_i is the experimental data point, and $f(x_i, \theta)$ is the model function of the independent variable x_i and parameter vector $\boldsymbol{\theta}$.

3.2.3 Simplified Stress-Strain Program

Once material parameters were obtained, a stress-strain program was written in ANSYS APDL to simulate a uniaxial (tension or compression) test and extract the stress-strain curve. The program uses a single element and the loading conditions illustrated schematically in 3.22.

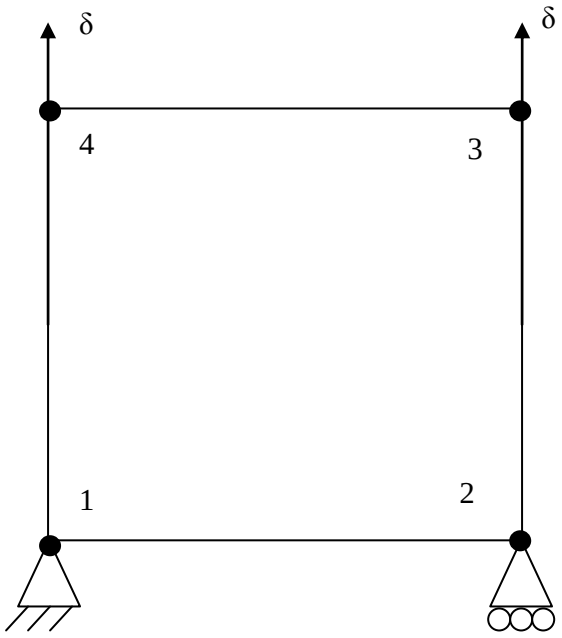

Figure 3.22: Loading conditions for stress-strain program

3.2.4 Simulation of the Direct Impact Pressure Bar

The final step in implementing the program is to verify functionality in two dimensions. The program offers two of the benefits of the Feng and Bassim model over a general purpose plasticity model, namely and temperature rise and the related thermal softening. This section describes the procedure used to model the specimen subjected to direct impact testing, where adiabatic shear bands are known to occur from the outside edges to the inside, as shown in Figure 3.23. A photograph showing this region on an actual specimen is shown in Figure 3.24.

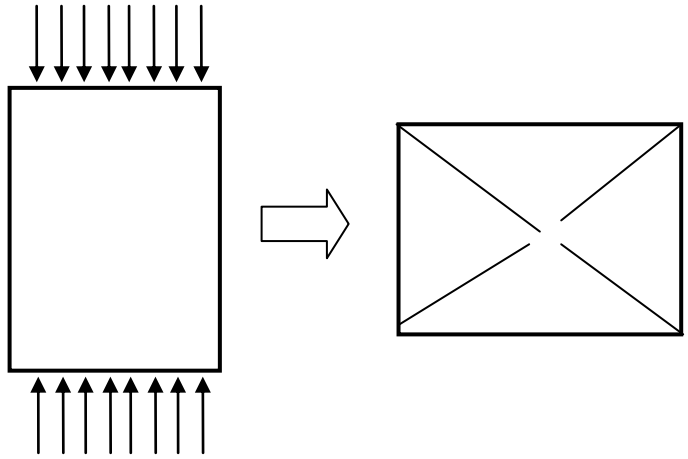

Figure 3.23: Cross-section of specimen before and after testing, showing approximate location of expected shear band formation

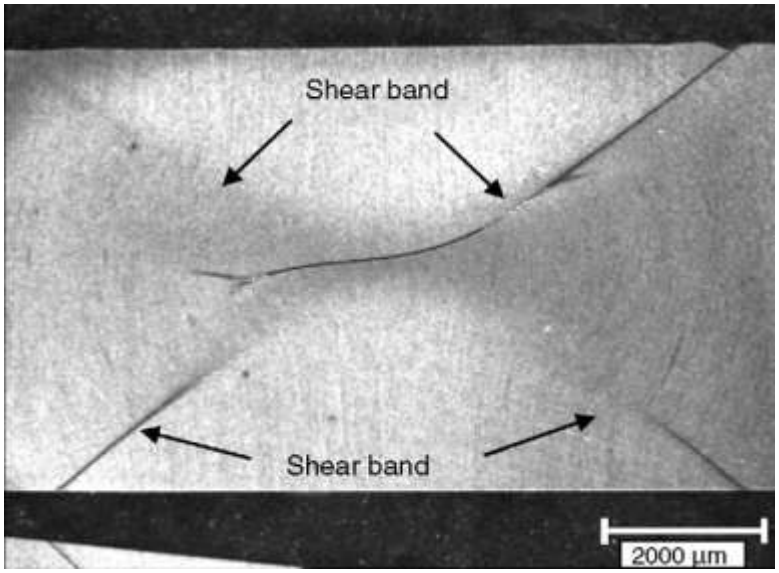

Figure 3.24: Photograph of compression specimen showing location of adiabatic shear bands (Odeshi et al. 2005)

A photograph of the area of interest for modelling is shown in Figure 3.25, including the striker bar (projectile), specimen, and pressure bar.

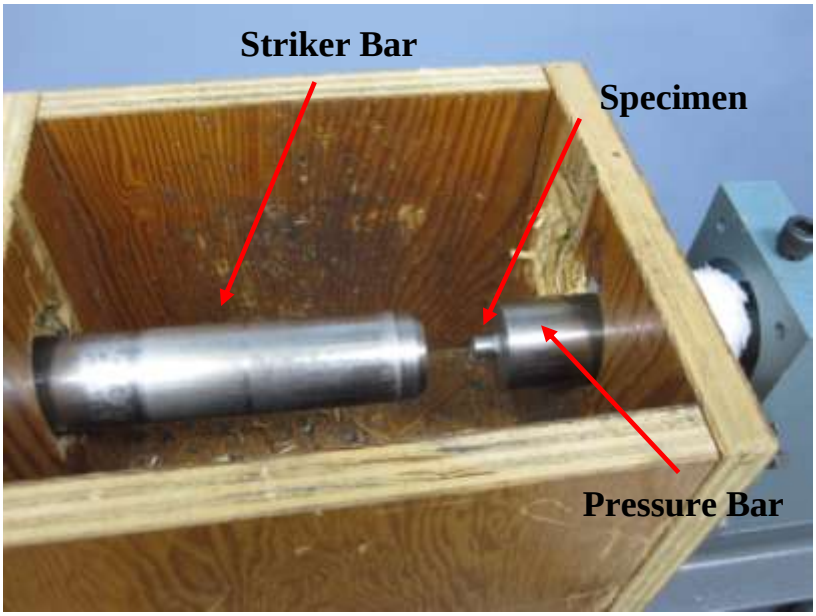

Figure 3.25: Photograph of the direct impact pressure bar at the specimen-bar interface

From the photograph, it is clear that this problem consists entirely of solid cylindrical rods of varying sizes, all arranged coaxially. For this reason, an axisymmetric model is used; simplifying the model to 2D allows for a much finer mesh and improves the level of detail possible with the available computing resources. To simulate this axisymmetric condition, all nodes lying along the axis of symmetry (Y-axis) are constrained in the X direction and in rotation about the Z-axis. A schematic showing these boundary conditions appears in Figure 3.26. The dashed line below the Y-axis represents an extension of the constraint to each node along the axis, since individual elements are not represented in this diagram. The dashed line perpendicular to the Y axis represents a break in the diagram, since the entire pressure bar is too long to show entirely.

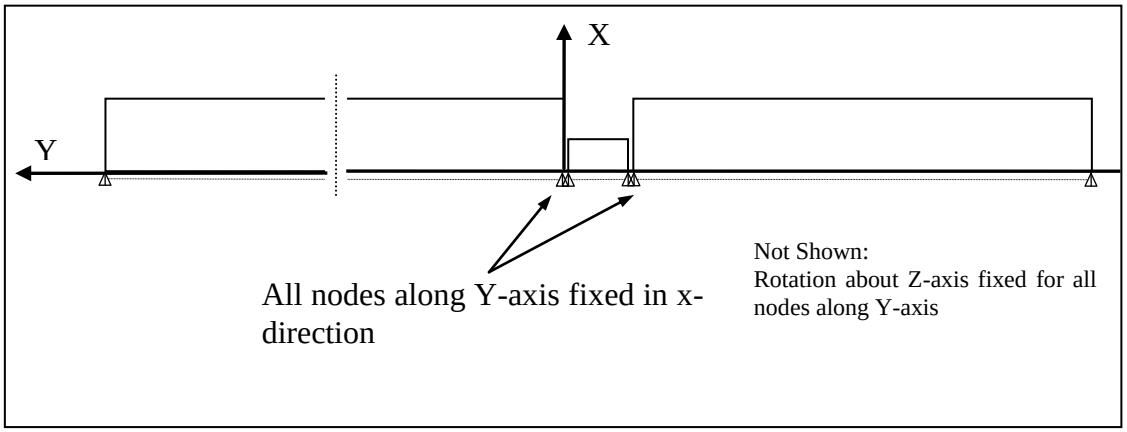

Figure 3.26. Boundary conditions for finite element model

The mesh for the model is refined in the regions of contact and in the specimen, where large strain gradients are expected. Element size in the elastic bars is selected to

capture wavelengths on the same order as the strain gages, which corresponds to an element length of approximately 5mm. The elements in the specimen are selected initially to be 0.2mm in length. To verify the accuracy of the solution, a second simulation is run using 0.1mm elements. The coarser mesh is used for the majority of the simulations to reduce computation time.

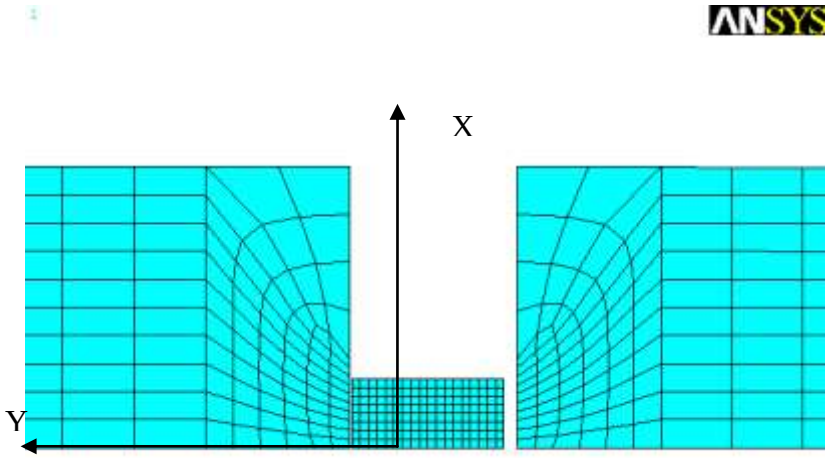

Figure 3.27. Transition Mapped Quadrilateral (Axisymmetric)

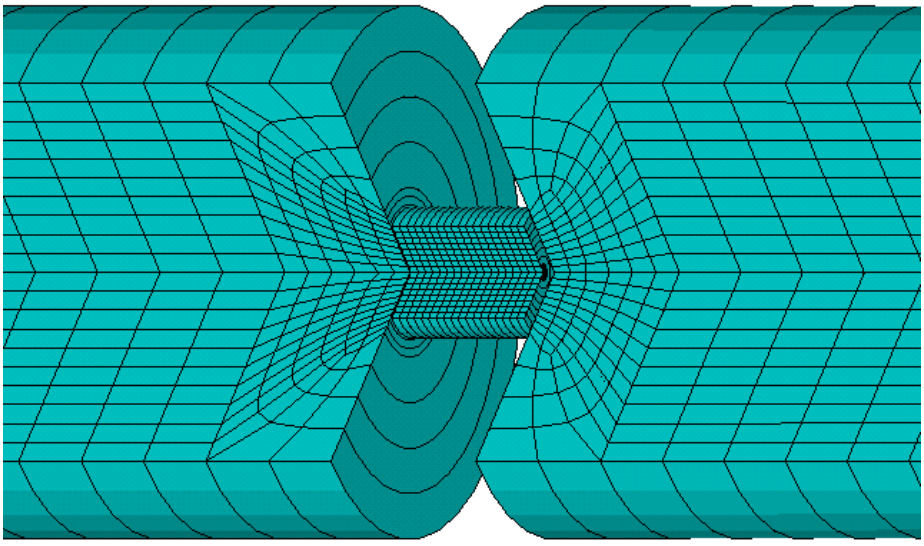

Figure 3.28. Transition Mapped Quadrilateral (Expanded 270°)

Figure 3.28 shows the same mesh expanded axisymmetrically, to help visualize the actual geometry of the problem. The area of refinement extends slightly beyond the specimen radius to account for radial expansion that occurs during compression. The area of refinement is matched to the contact (target) area. Contact is defined as shown in Figure 3.29. Surface-to-surface contact is used, along with quadratic contact and target elements. The target area lies along the refined region of the mesh for the elastic bar and striker, and the contact elements surround the entire specimen. Arrows indicate the normal directions for target and contact elements.

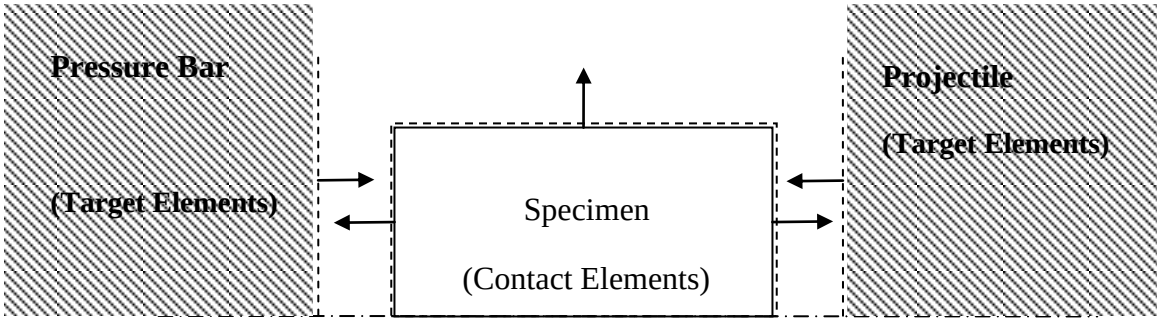

Figure 3.29. Contact normals

Friction is estimated as $\mu = 0.1$ to simulate the roughened steel surface of the projectile and pressure bar. The initial conditions are similar to a typical experiment, with a projectile velocity of 25m/s and temperature of 20^{o}C. This approximates an impact using a firing pressure of approximately 250 kPa with the apparatus at the University of Manitoba, and ASBs are known to form in steels at this pressure.

CHAPTER 4: EXPERIMENTAL AND MODELLING RESULTS

4.1 Experimental Results

This section describes the experimental results for bar calibration and direct impact experiments. The bar calibration section includes: bar speed and modulus, load-voltage relationship for the strain bridge, relationship between projectile velocity and firing pressure, dependence of saturation stress on impact momentum, and dependence of strain rate on impact momentum. The stress-strain curves are provided for impact momentums from 20 to 60 kg-m/s, and temperatures from 20 to 500^{o}C.

4.1.1 Bar Calibration

Bar calibration included measuring of elastic properties of the pressure bar, strain gage output versus bar strain, and firing pressure versus projectile speed. This calibration is especially important for direct impact tests, since there are no formal standards for conducting these experiments. Bar calibration is necessary to ensure the validity of the data and repeatability of the measurements, should repeated testing be required.

Bar speed was obtained by recording elastic reflections within the bar (Figure 4.1) and using a discrete fast Fourier transform algorithm to transform the data from the time domain to the frequency domain (Figure 4.2). The benefits of this method compared to measuring a single reflection, as discussed in Chapter 3, are increased accuracy due to the very large sample size (several hundred reflections) and removal of the human error component in consistently selecting the same part of the elastic wave.

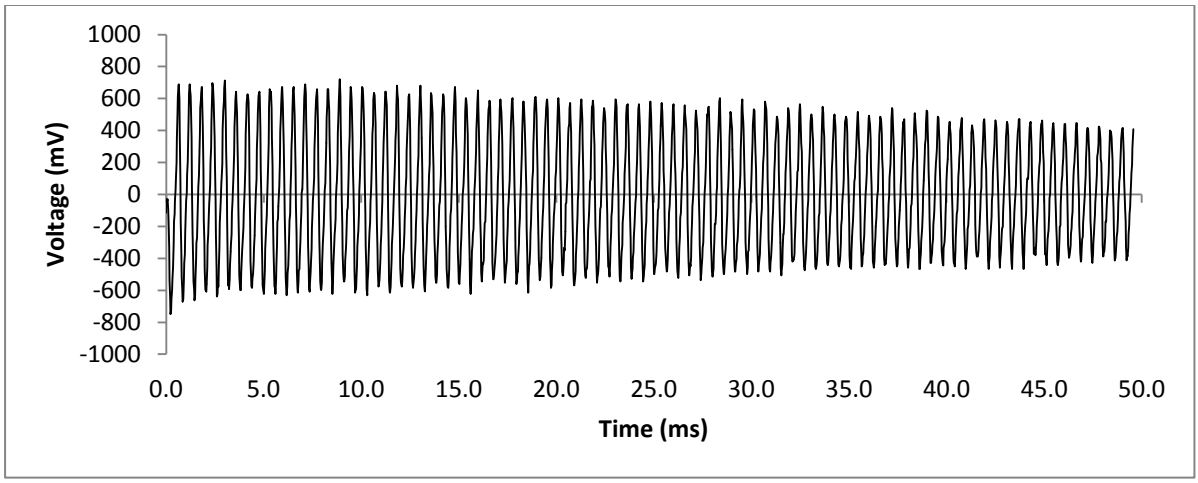

Figure 4.1: Voltage-time data for reflections of an elastic wave in the pressure bar.

Bar speed was measured by extracting the peak frequency from the single sided amplitude spectrum, as described in Chapter 3.

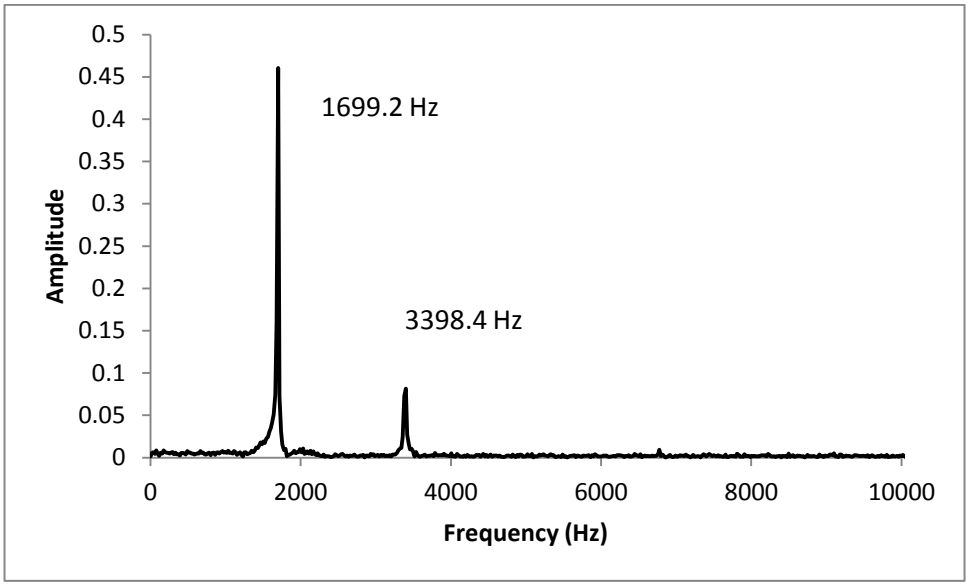

Figure 4.2: Single sided amplitude spectrum of voltage-time data from Figure 3.10, obtained using DFFT algorithm.

Two clear peaks are observed in Figure 4.2, with the first and largest at 1699.2 Hz, and a second smaller peak at 3398.4 Hz. These correspond to events with periods of approximately 600 and 300 microseconds respectively. The event with a period of 600 microseconds is the full wavelength of the wave and this is the frequency of interest. The second smaller peak represents a periodic disturbance of exactly twice the frequency of the first peak and accounts for the similarities in shape between like-signed waves (compression or tension).

Bar speed was calculated from each frequency as distance travelled by the wave between signals, as presented previously in Chapter 3. The period of the peak frequency was first identified as:

$$t = \frac{1}{f} = \frac{1}{1699} = 589(10)^{-6}\ \text{s}$$

Where t is the period, and f is the frequency. This corresponds to the time required for one lap of the bar, or $2(L_{bar})$, and was calculated to be 589μs. The bar speed (C_o) was then calculated as:

$$C_o = 2\frac{L_{bar}}{t} = 2\frac{1.525}{589(10)^{-6}} = 5178\ \text{m/s}$$

Where the length of the bar is 1.525 m. The uncertainty in this measurement was approximately 2 mm, which results in an estimated bar speed of 5178 ± 7 m/s (assuming the error in measurement of time was negligible, since the oscilloscope is capable of measuring down to nanosecond-timed events).

The modulus was calculated from the bar speed as another check of the result, and found to be 210.8 GPa, which is a reasonable value that agrees with values in the literature for steel.

$$C_o = \sqrt{\frac{E}{\rho}}$$

$$E = C_o^2 \rho = (5178^2)7850 \frac{\text{kg}}{\text{m}^3} = 210.8 \text{ GPa}$$

Projectile velocity as a function of firing pressure was recorded and plotted in Figure 4.3. The spread in the data shows that the relationship is not perfectly linear, but the high value of R^2 indicates that the relationship between velocity and pressure is strongly correlated, and that the linear regression line should provide a good approximation.

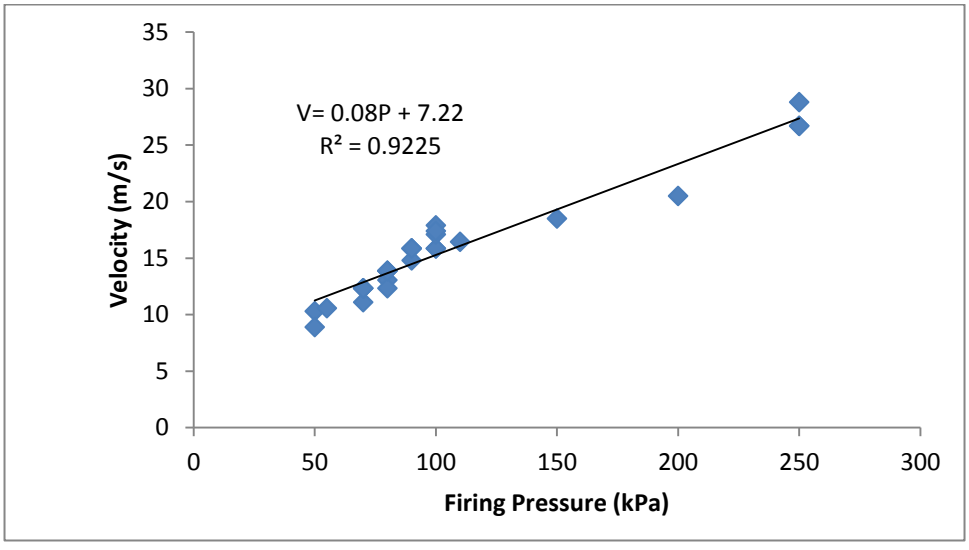

Figure 4.3: Velocity as a function of firing pressure for direct impact pressure bar apparatus

The load-output relationship is shown graphically in Figure 4.4. This equation was used to convert the measured voltage reading recorded by the strain gage amplifier to the magnitude of the load experienced by the pressure bar.

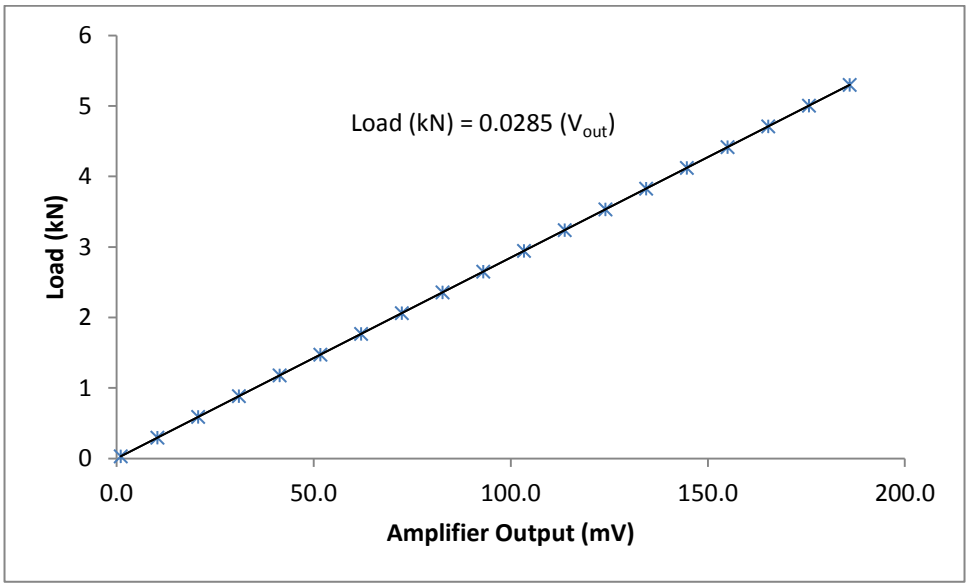

Figure 4.4: Load -Output curve for bar calibrated with parameters in Table 4.1.

The excitation voltage was set by finding the maximum setting that provided a stable signal. This value was found to be 5V for the current arrangement. Using 5V of excitation voltage, the system remained stable for the duration of the test. To further ensure a stable and reliable reading, the zero-offset was reset between tests. The settings for the strain amplifier were set by finding the maximum amount of gain possible that would not saturate at a maximum expected specimen stress of 2GPa and excitation voltage of 5V. A value of 1000 was found to allow for reliable measurement of strain without saturating the signal amplifier.

The bar calibration parameters obtained in this section are summarized in Table 4.1 below.

Table 4.1. Bar and strain gage calibration parameters

Parameter	**Value**
Gain	1000
Excitation Voltage (V_{exc})	5 V
Elastic Modulus (E_{Bar})	210.8 GPa
Poisson's Ratio (ν)	0.29
Gage Factor (GF)	2.11
Bar Speed (C_o)	5180 m/s
Load-Voltage Slope	0.0285 (kN/mV)
Velocity- Firing Pressure Line	0.08P+7.22

With these parameters and appropriate calibration, the direct impact apparatus is fully described and the results presented in the following chapter are justified and repeatable. The next section describes the experimental results obtained using these calibration parameters and the equations for stress-strain covered in Chapter 3.

4.1.2 Direct Impact Experiments

The purpose of the direct impact experiments is to validate and extend the model of Feng and Bassim. The experimental component measures the stress-strain response of a steel, AISI 4340, to various strain rates and temperatures, and these data are fit to a numerical model (Section 4.2.1). This section describes the results and important outcomes of the direct impact experiments.

The constant stress-strain curves, obtained using equations discussed in chapter 3, are presented along with the saturation stress and strain rates for each experiment. These curves and parameters are analyzed in Section 4.1.3 to extract the plasticity parameters required for the Feng and Bassim model of ASB formation. Finally, results for the impact momentum and saturation stress as functions of strain rate are shown at the end of this section.

Stress strain curves were obtained for each set of firing pressures, 250 kPa, 100 kPa, and 50 kPa. These curves are shown in Figures 4.5 - 4.7 respectively.

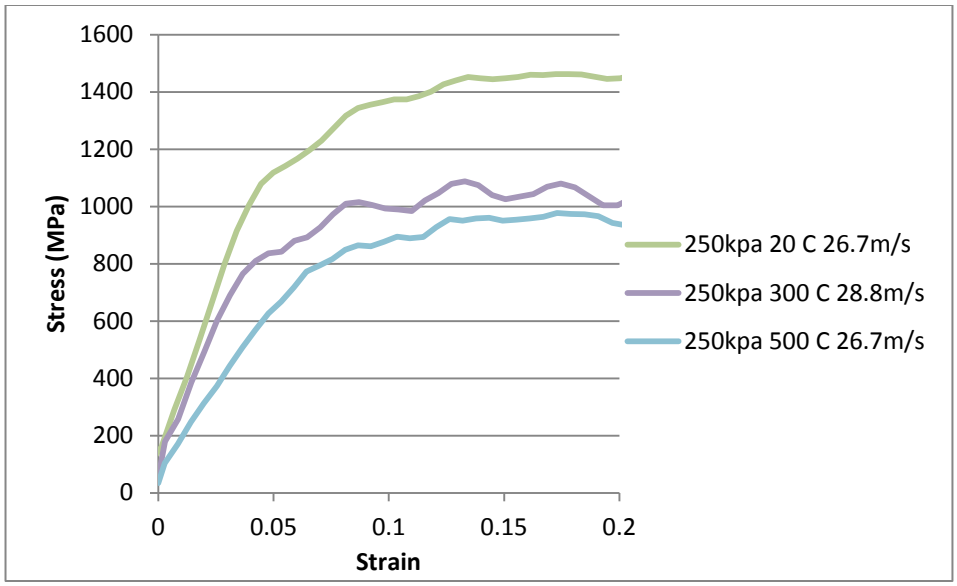

Figure 4.5: Stress-strain curve for AISI 4340 steel tested at 250kPa and varying temperature

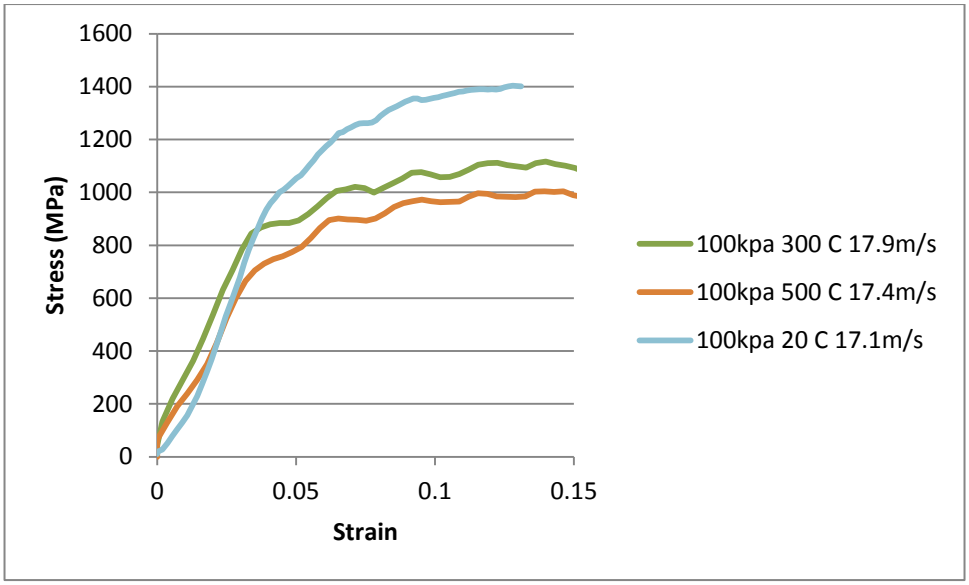

Figure 4.6:Stress-strain curve for AISI 4340 steel tested at 100kPa and varying temperature

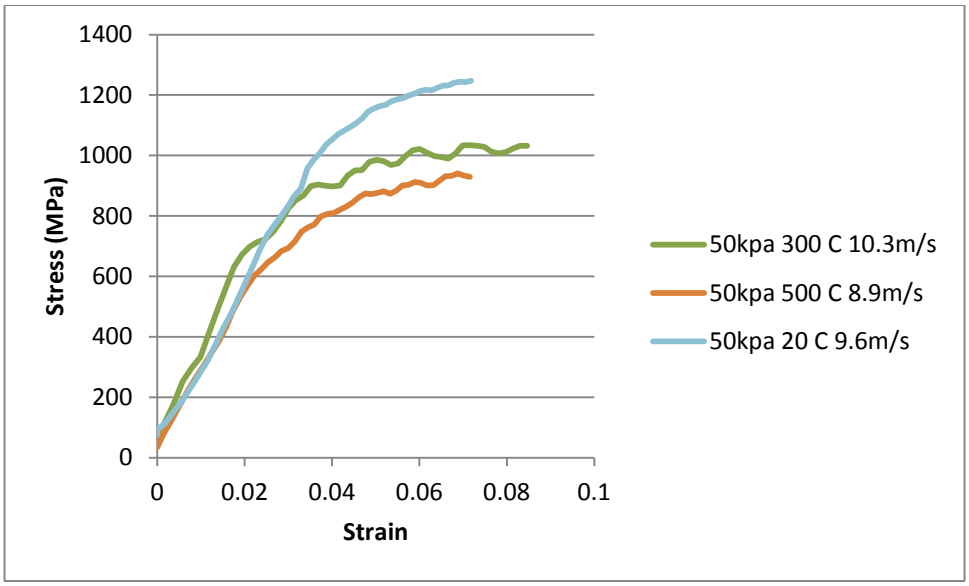

Figure 4.7:Stress-strain curve for AISI 4340 steel tested at 50kPa and varying temperature

Results for the saturation stress and strain rate from direct impact tests at each strain rate-momentum pair appear in Table 4.2. Note that these entries represent an average of all tests completed at the specific combination of impact momentum and temperature. Each entry represents the average of 3-5 individual experiments, with any extreme outliers, due to discarded.

Table 4.2: Summary of experimental results for saturation stress and strain rate

Testing Temperature	Impact Momentum (kg-m/s)	Velocity (m/s)	Saturation Stress (MPa)	Strain Rate (1/s)
20°C	18.3	9.6	1240	620
	32.6	17.1	1400	1500
	35.2	18.5	1400	1700
	38.5	20.2	1470	1900
	50.9	26.7	1460	2660
300°C	19.6	10.3	1030	830
	54.9	28.8	1070	2810
	34.1	17.9	1100	1710
500°C	33.1	17.4	1000	1680
	17.0	8.9	930	710
	50.9	26.7	970	2860

Saturation stress is an important material model parameter used in the Feng and Bassim model. The hardening equation, presented previously in chapter 3, uses a variable saturation stress to predict the resistance to plastic flow under a given combination of temperature and strain rate. The saturation stress was measured from each stress-strain curve as the maximum steady stress reached, and this value is used in subsequent curve fitting (Section 4.3.1).

Impact momentum was calculated for each test to allow for generalizations to other impact conditions. The graph of strain rate as a function of impact momentum (Figure 4.8) shows a very strong positive correlation and good linearity (R^2=0.988). This

indicates that impact momentum is a reliable method of estimating strain rates during direct impact experiments, and helps to generalize the results to impact with other projectiles.

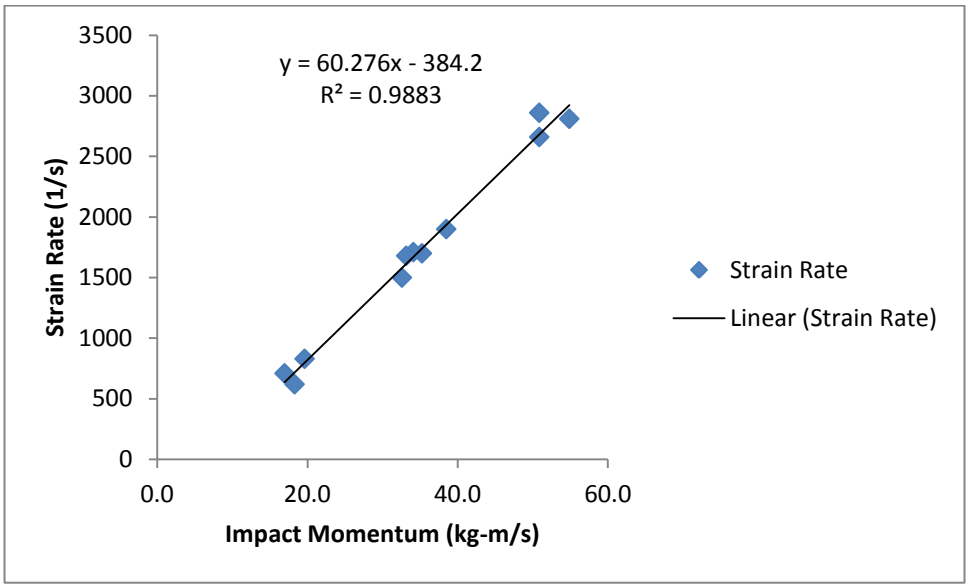

Figure 4.8: Strain rate as a function of impact momentum

The graph of saturation stress as a function of impact momentum (Figure 4.9) shows that there is not a significant correlation between the impact momentum and saturation stress over this range of strain rates tested, approximately 500/s to 3000/s. There is a slight positive correlation for the room temperature tests (all of the points above the regression line in Figure 4.9). However, the relationship does not hold for the tests conducted at 300°C and 500°C (the points below the regression line). In fact, there is a slight decrease in the saturation stress values from an impact momentum of 30 to 50 kg-m/s, indicating that the material shows no evidence of rate hardening over this range of impact momentums. This observation is reflected in the fit for the strain rate sensitivity to hardening parameter, n, which is discussed in the next section.

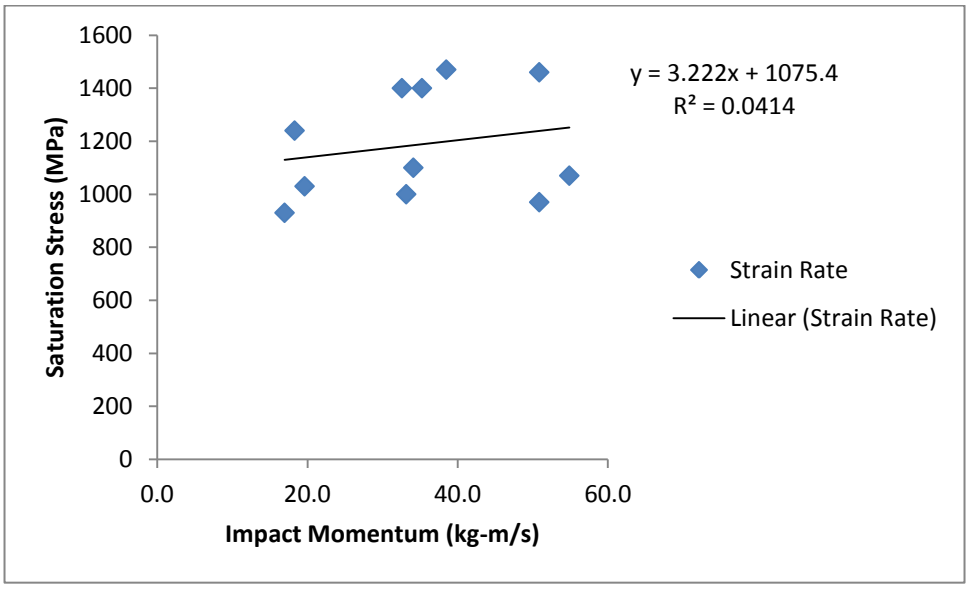

Figure 4.9: Saturation stress as a function of impact momentum

4.2 Numerical Results

This section describes the numerical results from the curve fitting procedure and finite element simulations, including: material parameters for the Feng and Bassim model, the validation of plasticity parameters with experimental stress-strain curves, the results for a simplified version of the heat evolution/localization program, and the implementation of this program into a simulation of the direct impact device.

4.2.1 Determining Parameters For Feng-Bassim Model

The Feng-Bassim model uses Anand's plasticity parameters, and these were fitted to the stress-strain curve data described in the previous section using a chi-squared reduction algorithm. Anand's plasticity parameters are a set of nine parameters that describe the homogenous rate and temperature dependent material behaviour. The general form of the Anand plasticity model includes an equation that specifies the saturation stress (3.25), and an equation for the hardening behaviour (3.26).

The saturation stress describes the maximum steady state stress that a material hardens to, as a function of strain rate and temperature. In general, the expected trend is that materials will reach higher saturation stresses when deformed at higher strain rates or lower temperatures.

$$\sigma^*(\theta, \dot{\varepsilon}_p) = \left(\frac{\hat{s}}{\xi}\right)\left[\frac{\dot{\varepsilon}_p}{A}e^{\frac{Q}{R\theta}}\right]^n \sinh^{-1}\left[\frac{\dot{\varepsilon}_p}{A}e^{\frac{Q}{R\theta}}\right]^m \qquad (3.25)$$

The hardening behaviour is described by the integrated hardening equation (3.26). This equation determines the specific shape of the hardening curve up to the saturation stress, using parameters $\sigma_o, a,$ and h_o. Physically, these parameters may be interpreted loosely as the yield stress (σ_o) and the steepness of the slope from yield stress to saturation stress

(a, h_o). The integrated hardening relationship, from which the hardening data is obtained, is shown below in (3.26).

$$\sigma = \sigma^* - \left[(\sigma^* - \sigma_o)^{\frac{1}{1-a}} + (a-1)\{ch_o(\sigma^*)^{-a}\}\dot{\varepsilon}_p\right]^{\frac{1}{1-a}} \quad (3.26)$$

The first step for the fitting procedure is to record all saturation stress - strain rate pairs for each experiment. These values for saturation stress are measured from each stress-strain curve as the steady state value reached during deformation, and the values for strain rate are calculated from the strain-time data, as described previously in Chapter 3. A summary of the averaged results are shown in Table 4.3.

Table 4.3: Summary of experimental results for saturation stress and strain rate

Testing Temperature	**Firing Pressure (kPa)**	**Saturation Stress (MPa)**	**Strain Rate (1/s)**
20 ^{o}C	50	1240	620
	100	1400	1500
	150	1400	1700
	200	1470	1900
	250	1460	2660
300 ^{o}C	50	1030	830
	250	1070	2810
	100	1100	1710
500 ^{o}C	100	1000	1680
	50	930	710
	250	970	2860

These saturation stress-strain rate pairs were fit to the integrated hardening relationship (3.26) using linear regression. The fit curve with parameters "a" and the combined hardening term "ch_o" using equation (3.26) compared to the experimental data is shown in Figure 4.10.

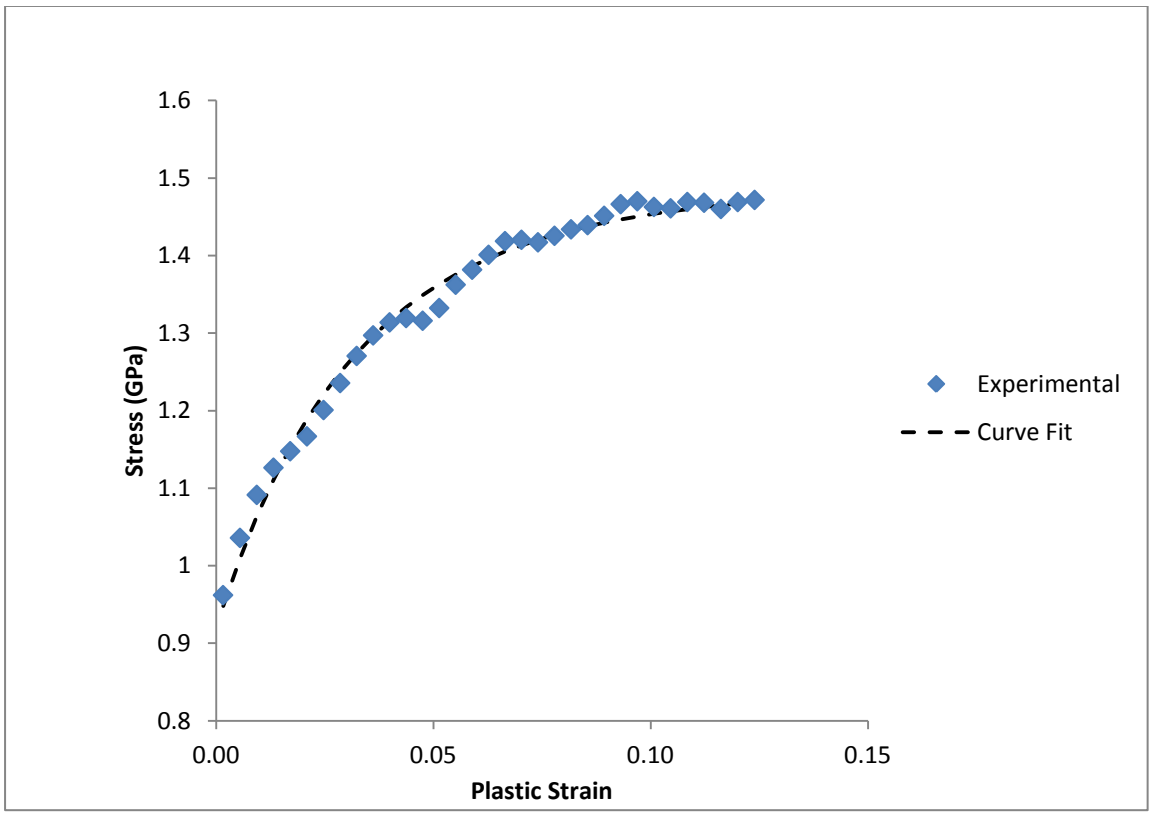

Figure 4.10: Sample of fitting results for the strain rate sensitivity of hardening parameter, "a", and the combined hardening term "ch_o"

From Figure 4.10, the hardening behaviour was found to be well represented by the Anand plasticity model.

The second set of fitting required to use Anand plasticity model is for the saturation stress equation (3.25). This equation is highly non-linear and requires non-linear curve fitting techniques, described previously in Chapter 3. The parameters A, $\frac{Q}{R}$, m, n, and $\frac{\hat{s}}{\xi}$ in the saturation stress equation are fit simultaneously to the experimental data for saturation stress as a function of temperature and strain rate. The results of the curve fit are shown in Figure 4.11.

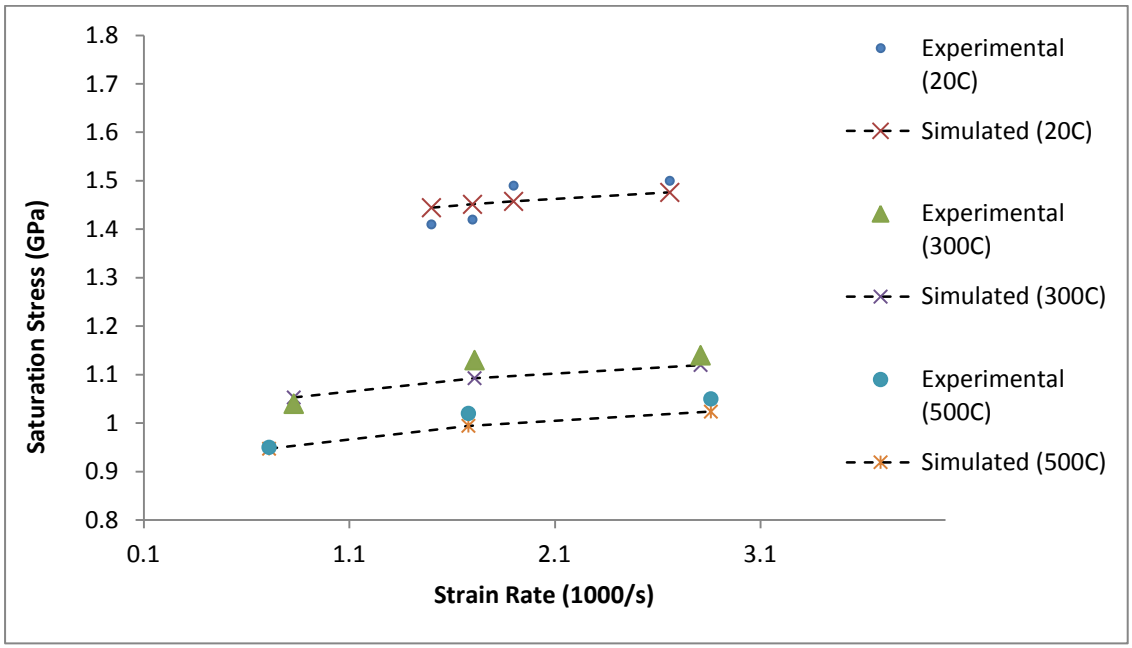

Figure 4.11: Comparison of experimental results for saturation stress to the fit parameters for strain rate dependence

In general, the fit appears good over the range of temperatures and strain rates tested. Note the very weak dependence of saturation stress on strain rate at higher temperatures. The experimental data shows a decrease in saturation stress at increased

strain rate, which is not possible for the Anand model to capture. This results in a very small parameter "n" for strain rate sensitivity of saturation (n = 0.0001).

The same results in terms of temperature are shown in Figure 4.12. Two simulated strain rate lines are shown in the figure to show upper and lower bounds of the model. The majority of the experimental data points fit well with the model.

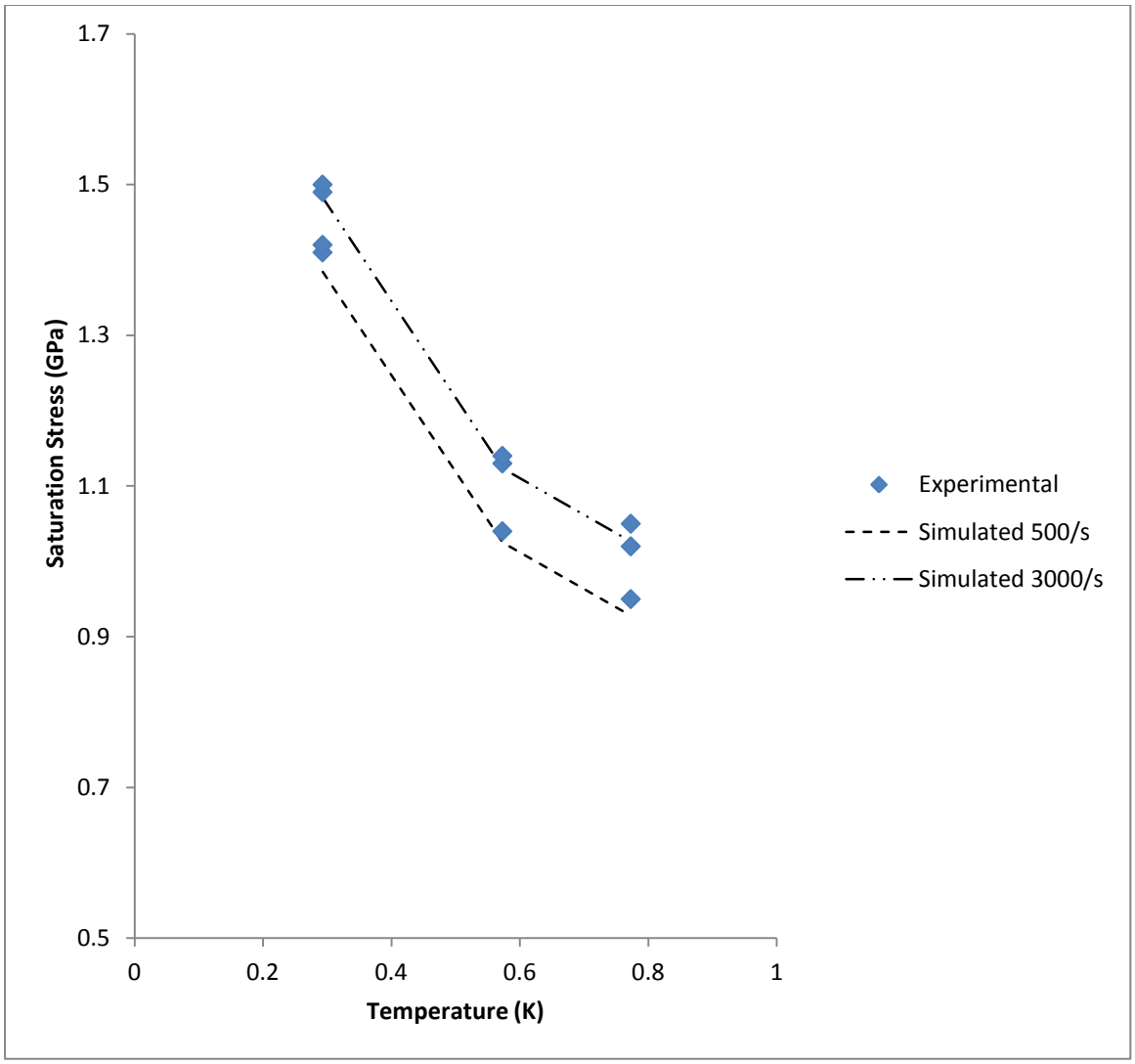

Figure 4.12: Comparison of saturation stress at varying temperature and two strain rates with experimental results

The final set of parameters for Anand's Model is the initial value for the stress resistance. These values were found at each temperature (20, 300, and 500°C) and found to be represented well (R^2=0.98) over this range by the linear relationship $\sigma_o = 9.28(10)^8 - 9.60(10)^5(T)$ where T is the temperature in degrees Celsius. This is shown in Figure 4.13.

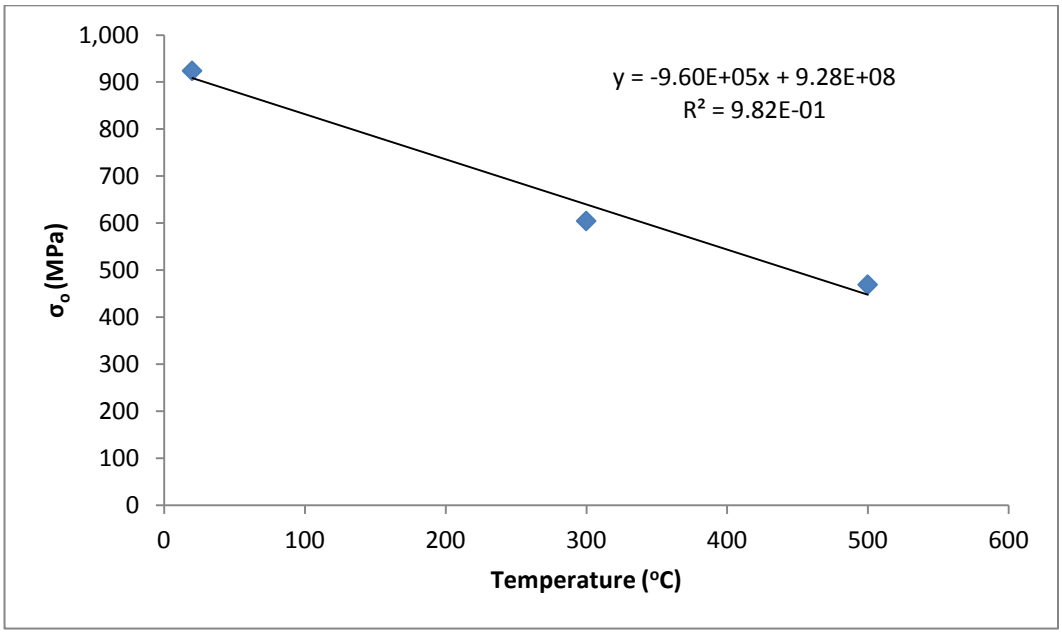

Figure 4.13: Initial value of saturation stress as a function of temperature

In summary, the parameters $a, ch_o,$ and σ_o were determined by linear regression of the integrated hardening relation (3.26), and the parameters A, $\frac{Q}{R}$, m, n, and $\frac{\hat{s}}{\xi}$ were obtained by non-linear regression to the saturation stress equation (3.25). A summary of the results of this section for parameters fitted to the experimental data are shown together in Table 4.4.

Table 4.4: Anand plasticity parameters for AISI 4340 steel tempered at 550°C. Valid for strain rates up to 3000/s and temperatures from 20°C to 500°C.

Parameter	Meaning	Value
s_0	Initial value of deformation resistance	450 MPa
$\frac{Q}{R}$	Q = activation energy R = universal gas content	3922 K
A	Pre-exponential factor	0.01014
ξ	Multiplier of stress	9.3
m	Strain rate sensitivity of stress	0.67893
h_o	Hardening/softening constant	53.7 GPa
$\hat{s}$	Coefficient for deformation resistance saturation value	752 MPa
n	Strain rate sensitivity of saturation	0.00001
a	Strain rate sensitivity of hardening or softening	1.3

These parameters require validation with experimental data to ensure that they accurately simulate the experimental stress-strain curves, the next section discusses the verification procedure. The sensitivity of these parameters to extrapolation outside of the range of fit is discussed in Chapter 5.

4.2.2 Validation of Material Model Parameters

Validation of material parameters is important to ensure that the fitted values in the model adequately simulates the experimentally measured stress-strain behaviour. Material model parameters were validated by developing a uniaxial stress-strain simulation in ANSYS. The results show good agreement with the experimental model at each temperature, and are shown in Figure 4.14.

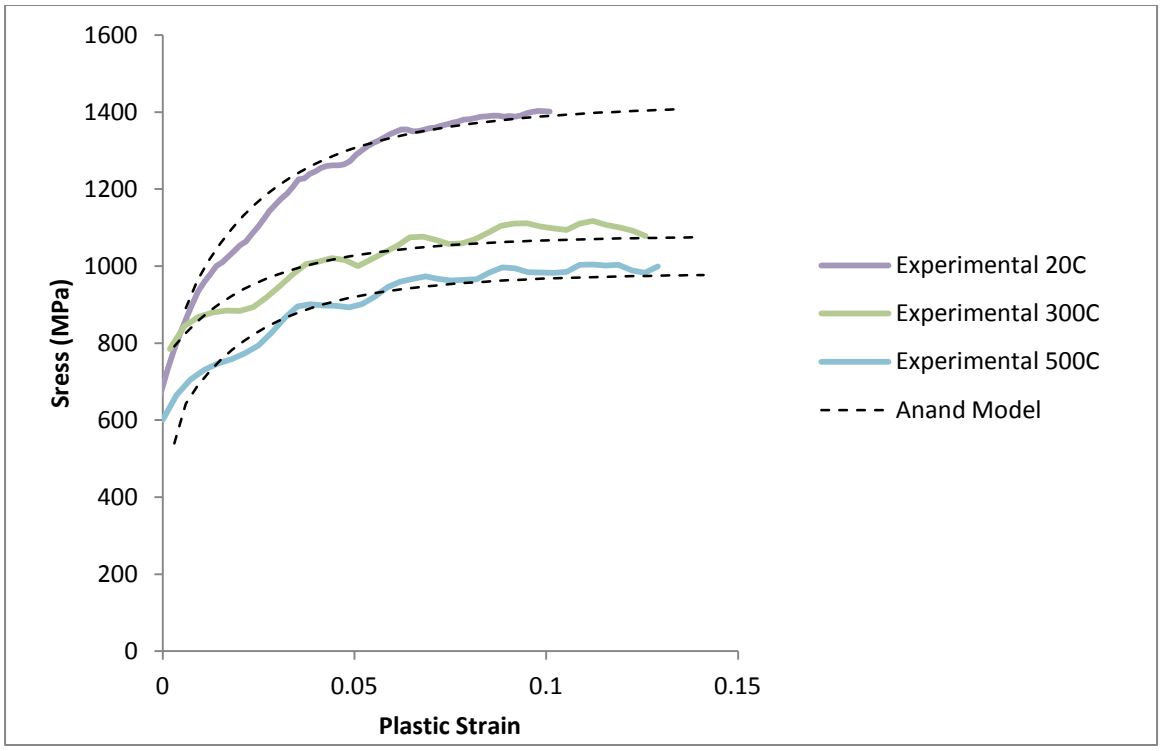

Figure 4.14: Comparison of fitted Anand model parameters to experimental data at 20°C, 300°C, and 500°C

4.2.3 Validation of Program Functionality

The next step in the validation procedure is to verify that the heat evolution functionality of the program is functioning correctly. Most finite element packages do not include self heating effects due to plastic work, since this is not a concern at lower strain rates. This functionality is introduced using the process outlined in Chapter 3. To verify that this aspect of the program is working, the same stress-strain program described previously was setup to run a single element with temperature evolution effects included. The temperature increase is shown in Figure 4.15 and the resistance to plastic deformation as a function of time is shown in Figure 4.16.

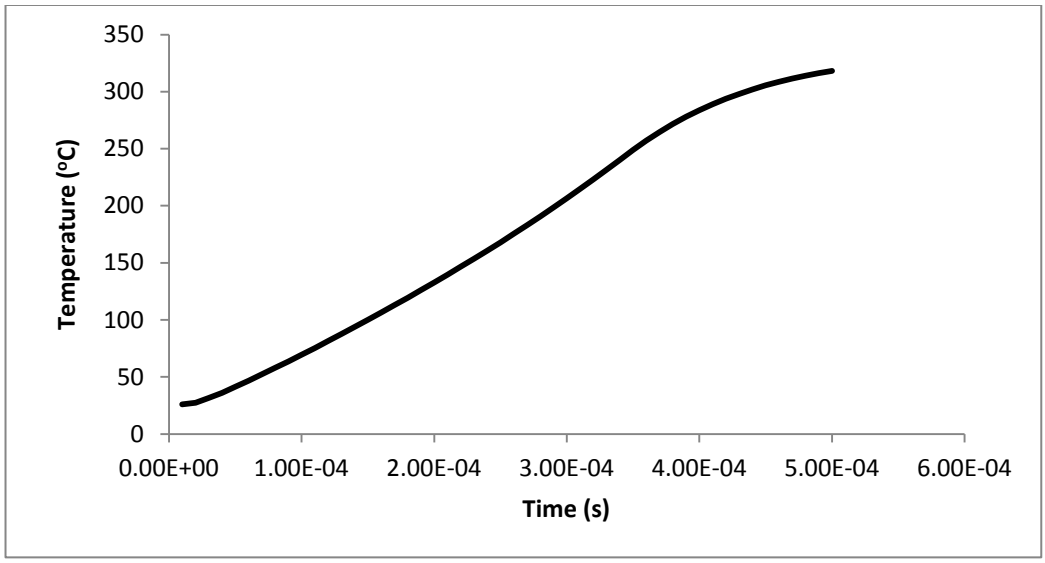

Figure 4.15: Simulated temperature rise in single Anand element undergoing uniform compression at 1500/s

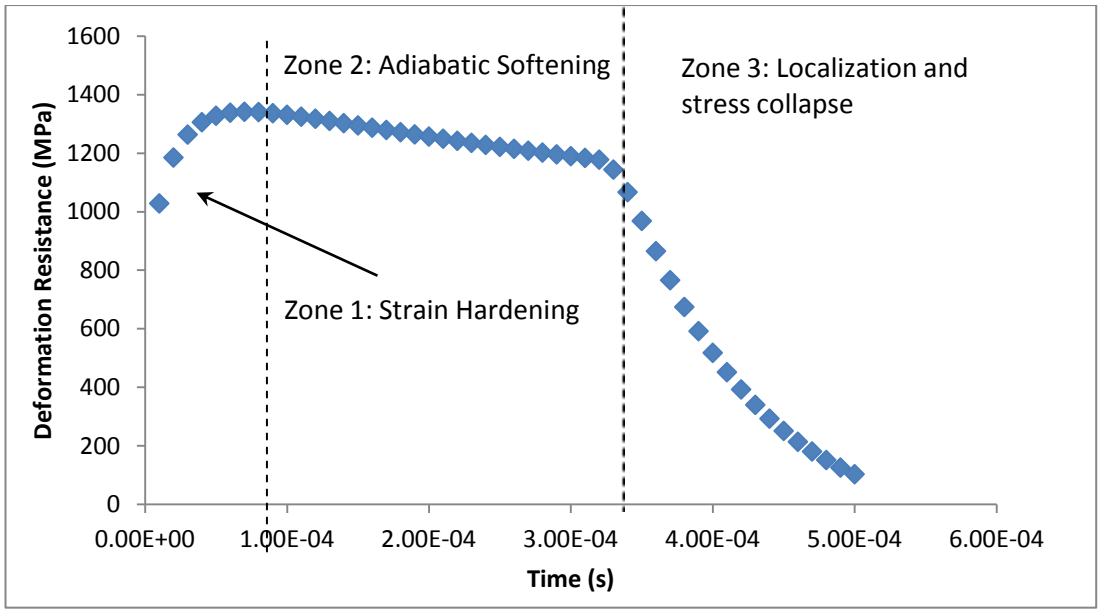

Figure 4.16: Simulated evolution of the stress resistance of a single Anand element deformed in compression at 1500/s

These results validate those obtained by Feng and Bassim (1999), shown in and the softening stage is extended to collapse.

4.2.4 Program Results

This section presents results for a direct impact simulation using the program for temperature evolution and localization. Two simulations were conducted, the first used coarse time-stepping and temperature evolution (10 divisions). The second used finer temperature updating intervals (100 divisions). The coarse mesh allows for verification of program functionality since the temperature updates are visible as steps in the output stress. The finer temperature updating intervals allow for a more homogenous curve and a more refined evolution of temperature and properties, but is more computationally expensive. General trends are reported for the coarse results, and the fine results are presented at the end of the section.

4.2.3.1 Coarse Temperature Updating

Results for the temperature distribution, plastic shear strain, and deformation resistance are shown in the following figures. Graphs of the evolution of each of these quantities for an element at the predicted site of ASB formation, at an element in the centre of the specimen, and an element on the edge. The location of individual elements are shown in Figure 4.17.

The temperature profile of the specimen after deformation is shown in Figure 4.17 and the accompanying graph showing evolution of the temperature is shown in Figure 4.18. Note the coarse divisions for temperature updating make the curve appear jagged. The temperature is predicted to be highest in the centre of the specimen and at

the corners, where ASBs are likely to initiate. The element away from the edge shows a much smaller temperature rise.

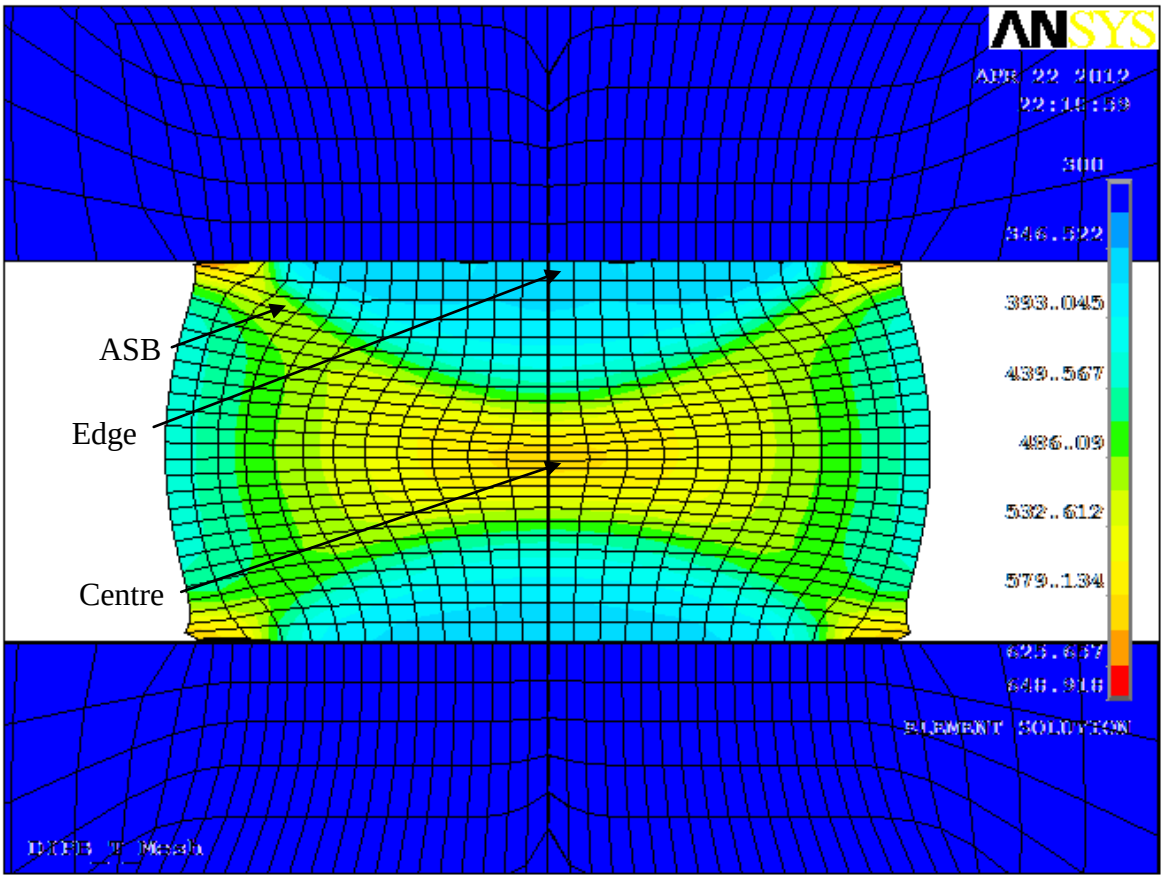

Figure 4.17: Simulated temperature rise during impact at 38kg-m/s

Note that the elements at the corners of the specimen have a very high aspect ratio, and for this reason, they are not chosen for further consideration. To examine the temperature rise and stress in this region, an element adjacent to this region is selected instead. To verify that this high stress region was not an error caused by sharp corners, a second simulation was run using a specimen with chamfered corners. The results indicate that this region still experiences higher temperature rise and plastic deformation than the surrounding region.

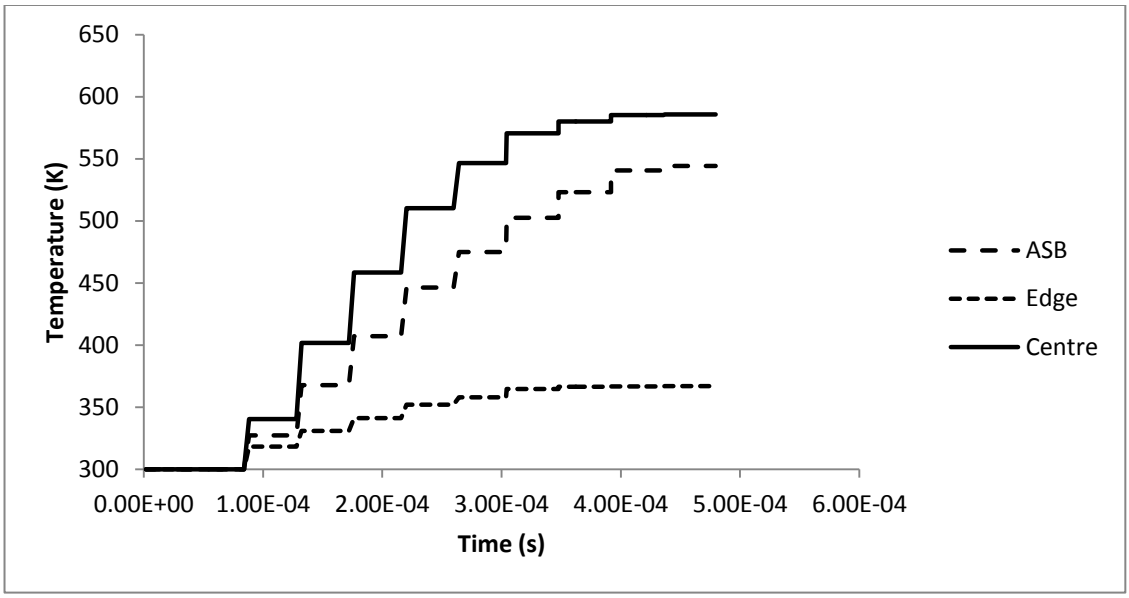

Figure 4.18: Evolution of temperature at predicted site of ASB formation, at the edge of the specimen, and at the centre.

Results for the total plastic shear strain are shown in Figure 4.19. This figure illustrates the areas of highest shear, where the material is most likely to fail by forming ASBs. The highest shear strains were observed on the corners of the specimen, moving in symmetrically towards the centre of the specimen, and outwards from the centre of the specimen to the edges.

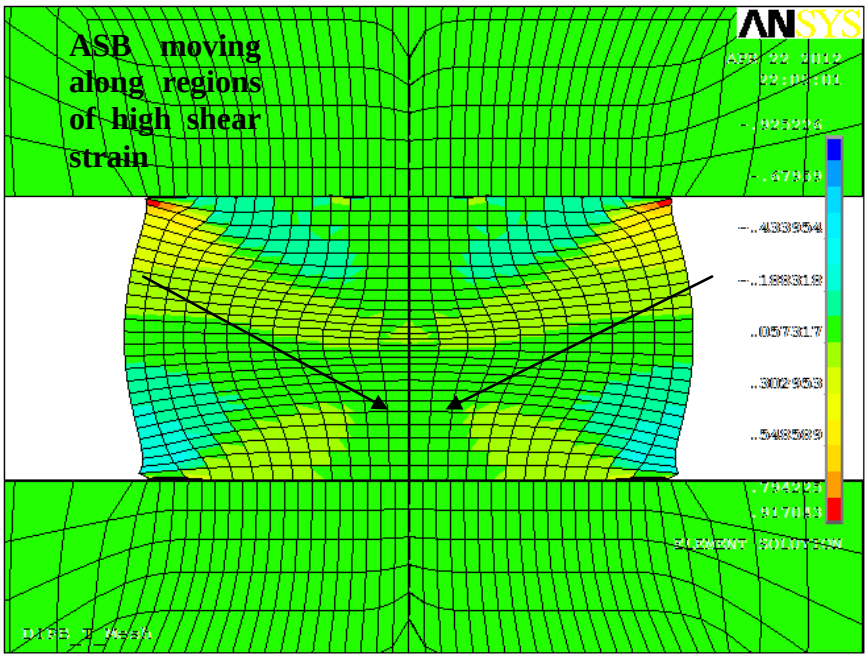

Figure 4.19: Simulated plastic shear strain in specimen impacted at 38kg-m/s

The shape of the high shear regions indicate a higher degree of curvature where shear is most severe, diffusing along the line as it progresses from edge to centre. This curvature is shown in Figure 4.20.

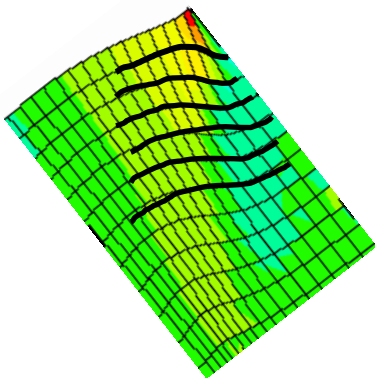

Figure 4.20: Shape of deformed mesh along regions of high shear strain

The simulated shear strain at the same three points (ASB, edge, and centre) was recorded, and these results are shown in Figure 4.21.

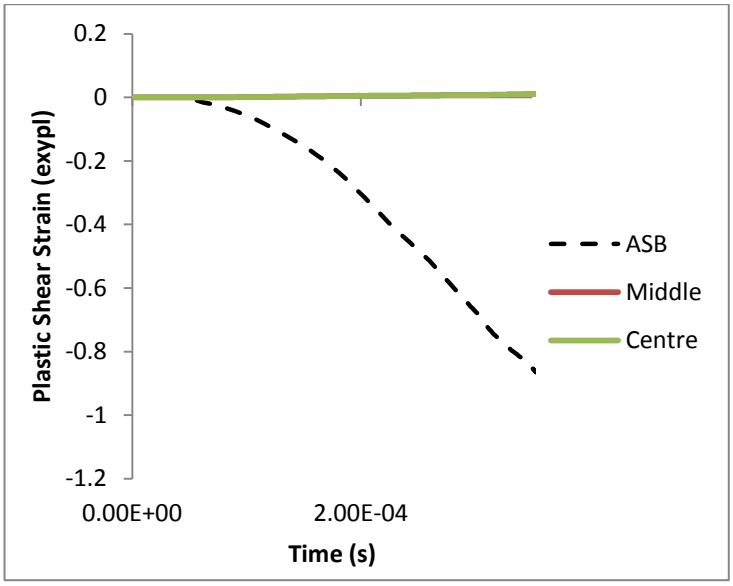

Figure 4.21: Simulated plastic shear strain as a function of time at three locations within the specimen impacted at 38 kg-m/s

The only regions that showed significant plastic shear strain were constrained along the line from the corner to the centre of the specimen.

Deformation Resistance Curves

Deformation resistance curves are a useful way for predicting the timing of ASB initiation, as well as a material's susceptibility to formation of ASBs. These curves are unique to the Anand model, and were first developed by Feng and Bassim as a means of predicting the evolution of ASBs.

Deformation resistance curves were generated from the observed flow stress and relationship between the flow stress and the internal variable "s" for deformation resistance, as discussed in Chapter 2:

$$\sigma = cs$$

Where σ is the flow stress, c is a constant, and s is the deformation resistance parameter.

The resulting curves appear in Figure 4.22.

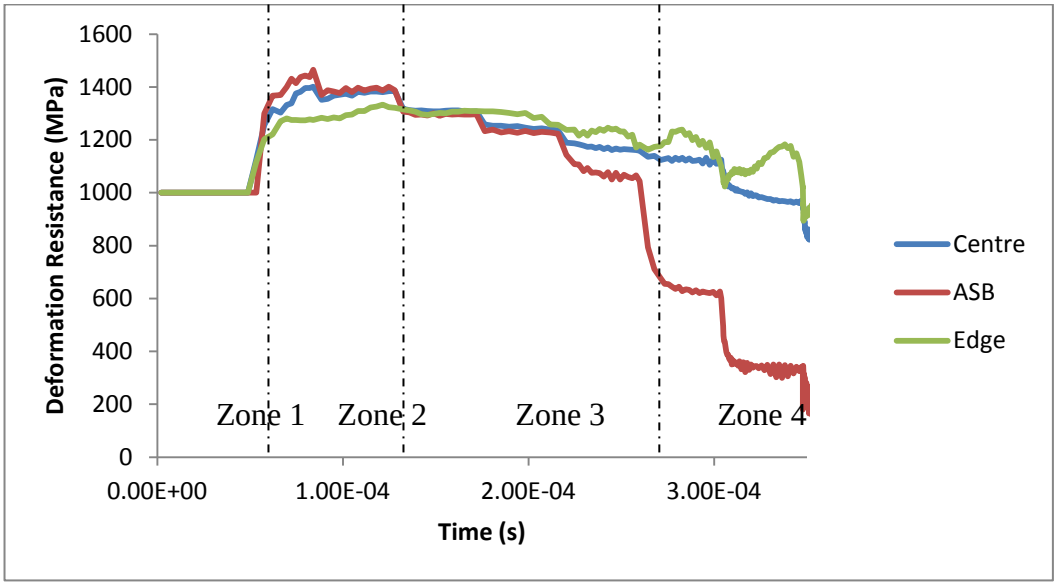

Figure 4.22: Simulated deformation resistance for specimen impacted at 38 kg-m/s

The curves in Figure 4.22 show 4 distinct regions: elastic (1) , hardening-dominated (2) , adiabatic softening (3) , and localization (4). These sections are separated by dashed lines in the figure. The only region that shows collapse is the element near the likely site of ASB initiation. The sections near the edge and centre show adiabatic softening, but not localization. This observation validates the general form of the

deformation curve of Feng and Bassim (1999), which shows the same characteristic shape (Figure 2.13).

ASBs were only predicted in regions with large shear strain together with high temperature. Areas that have high temperature alone, such as the middle of the specimen, do not display stress collapse, but still soften adiabatically and have the potential for stress collapse if a shear stress is present.

4.3.2.2 Fine Temperature Updating

Curves for temperature rise, deformation resistance, and plastic shear strain are shown in Figures 4.24 - 4.26 respectively. The properties were sampled at a region of expected ASB formation, at the centre of the specimen, and at location near the region of ASB formation. The location of these elements on the un-deformed mesh is shown in Figure 4.23

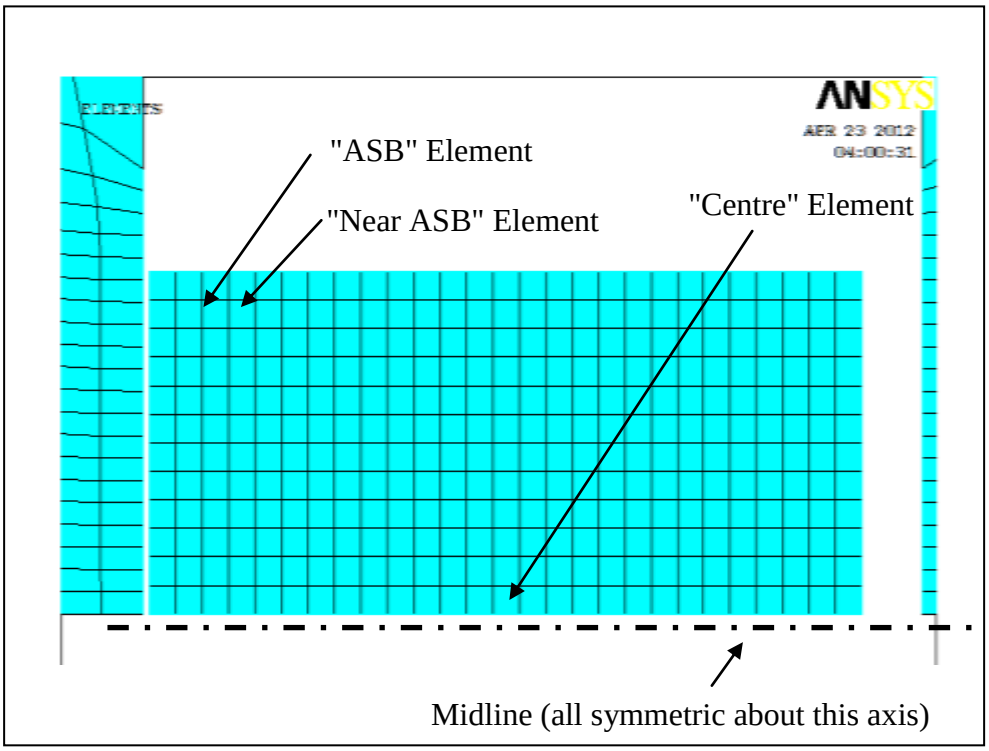

Figure 4.23: Location of elements on undeformed mesh.

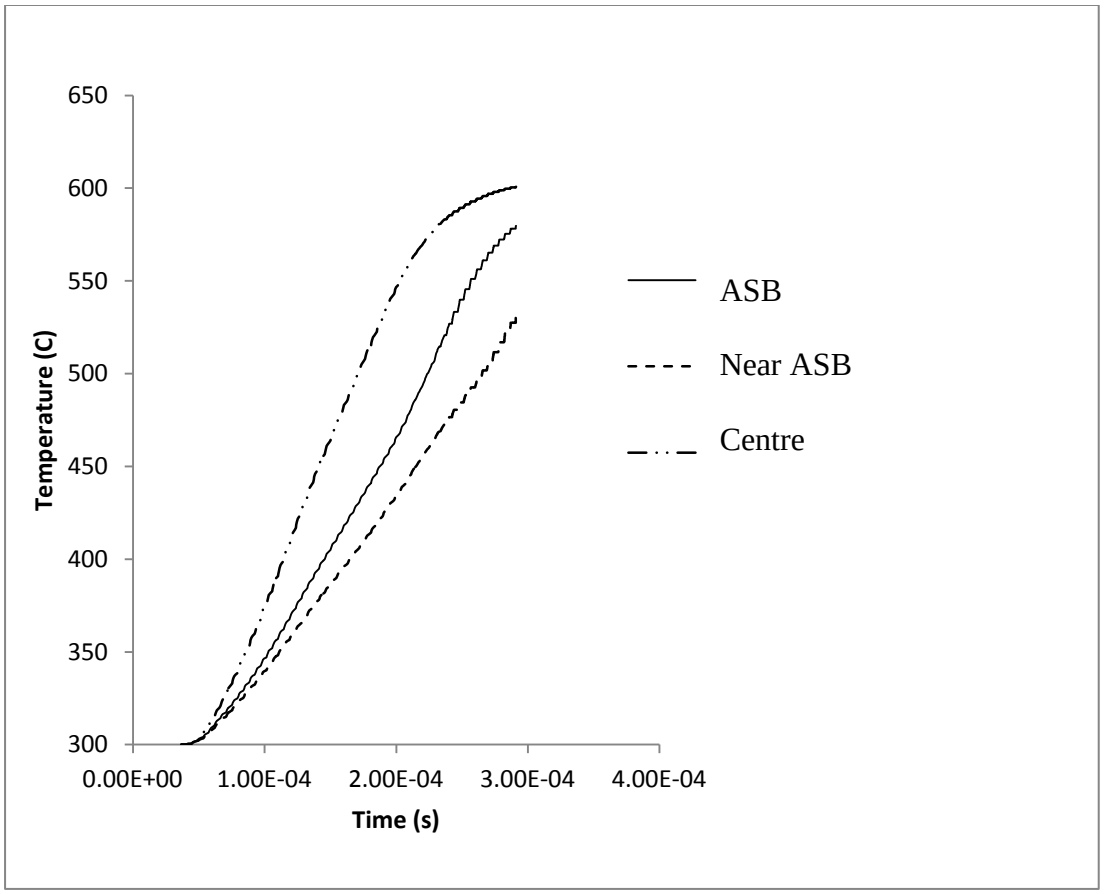

Figure 4.24: Temperature evolution along region of predicted ASB, at centre of specimen, and near the location of ASB

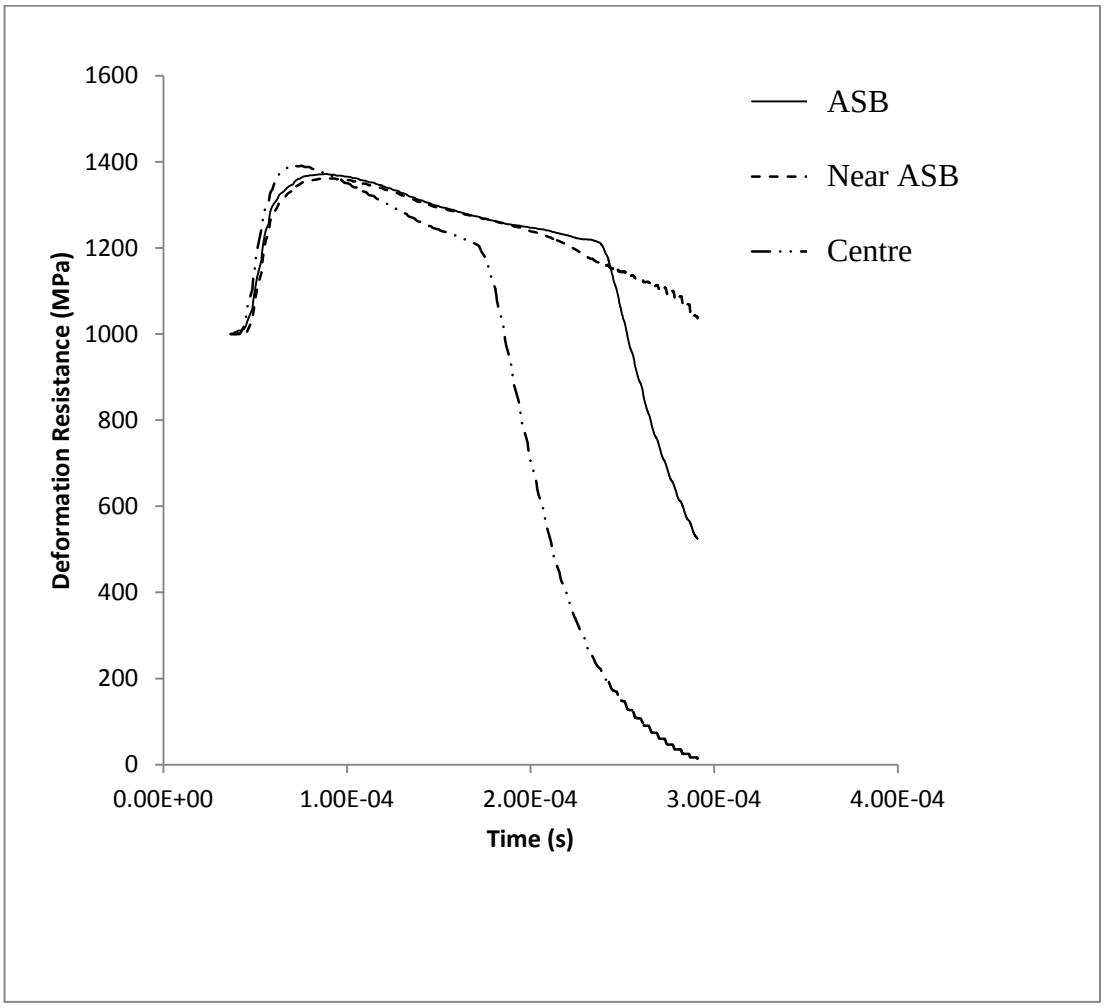

Figure 4.25: Evolution of deformation resistance along region of predicted ASB, at centre of specimen, and near the location of ASB

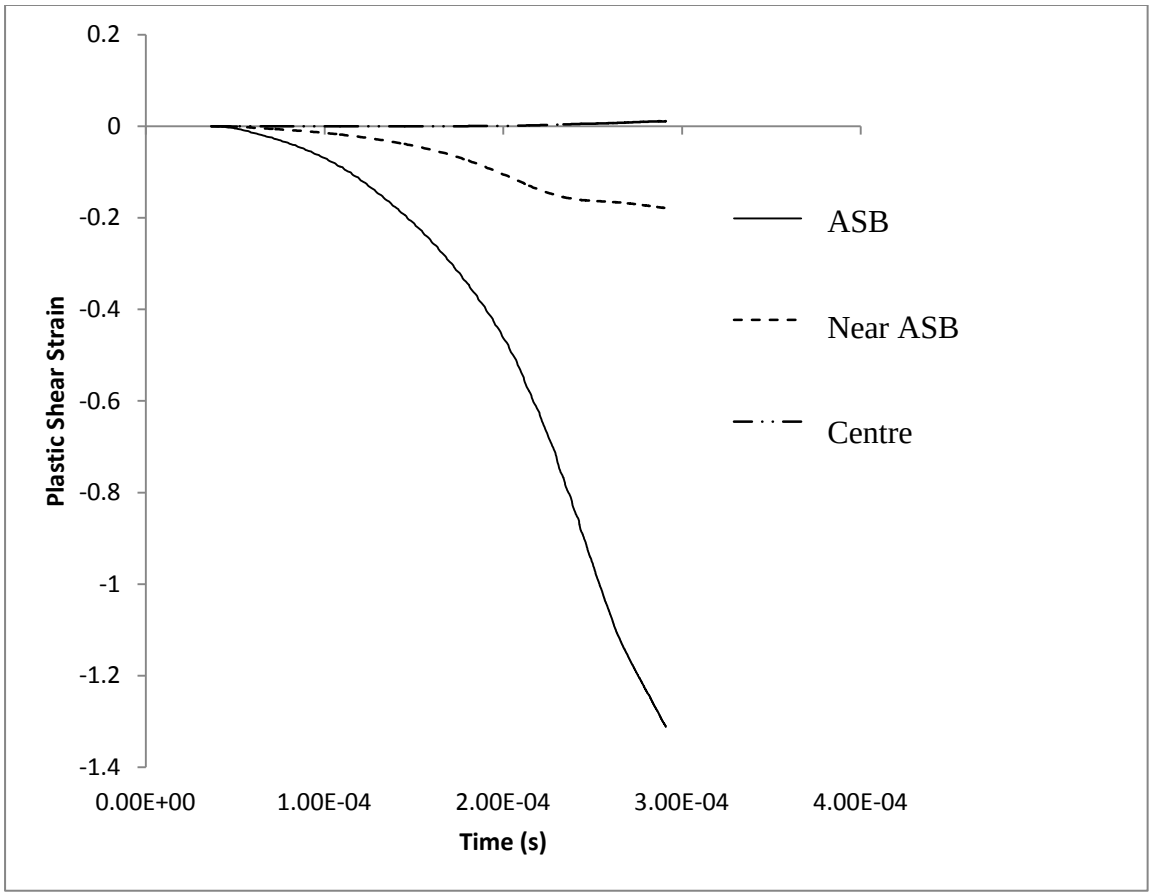

Figure 4.26: Evolution of shear stress along region of predicted ASB, at centre of specimen, and near the location of ASB

These results show that there are regions of intense temperature rise predicted, which are high enough to result in stress collapse, both at the edges and at the centre of the specimen (Figure 4.25). Only the area where ASBs are predicted, along the line from edge to centre, show an increase in shear strain (Figure 4.26). This shear strain decreases significantly moving away from this line (from "ASB" to "Near ASB" in Figure 4.23).

From the time of localization in the deformation resistance curve (Figure 4.25), it is possible to extrapolate back to the stress-strain curve to determine the nominal strain where the onset of ASB is possible. Nominal strain-time curves were generated by exporting the displacement-time data from the two central nodes at either end of the specimen. These curves are plotted in Figure 4.27.

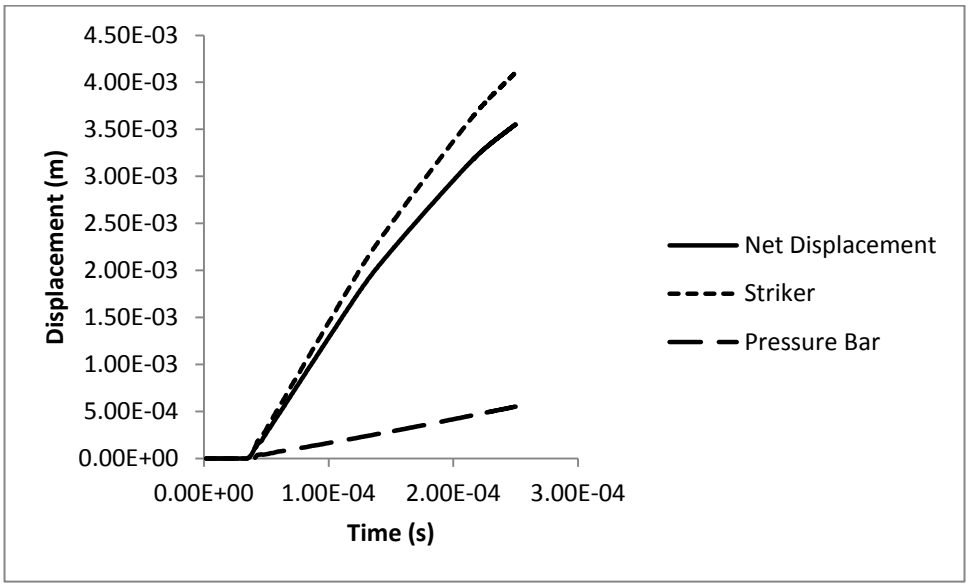

Figure 4.27: Displacement-time curves for the axial nodes at either end of the specimen

The net displacement represents the compression-time information. The true strain-time curve was calculated from this curve to show the nominal strain as a function of time for the simulated direct impact experiment.

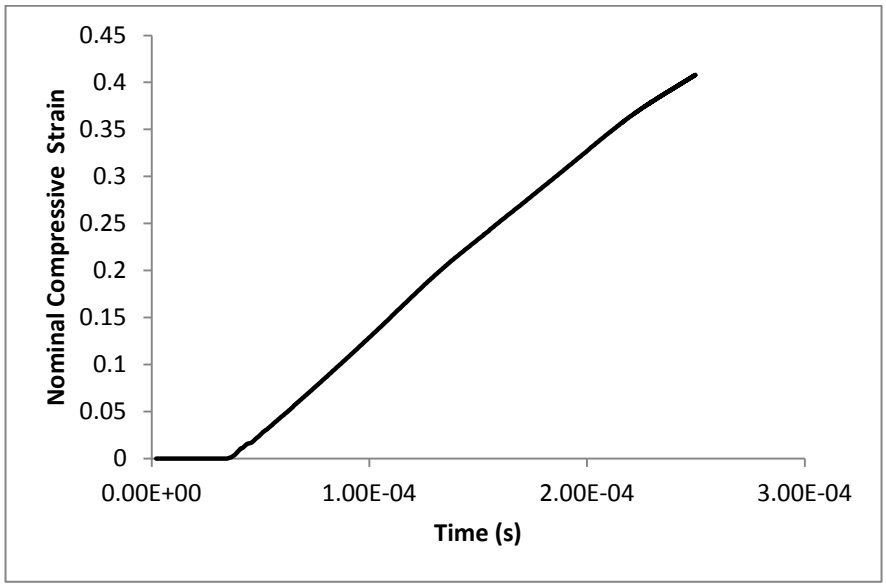

Figure 4.28: Simulated nominal strain in the specimen impacted at 38kg-m/s

The strain rate-time was plotted as an additional check of the validity of the results and assumptions regarding the range of strain rates experienced by the specimen. This data was calculated using the 3 point central difference formula and smoothed over 50μs intervals to make the trend visible. The strain rate-time plot is shown in Figure 4.29.

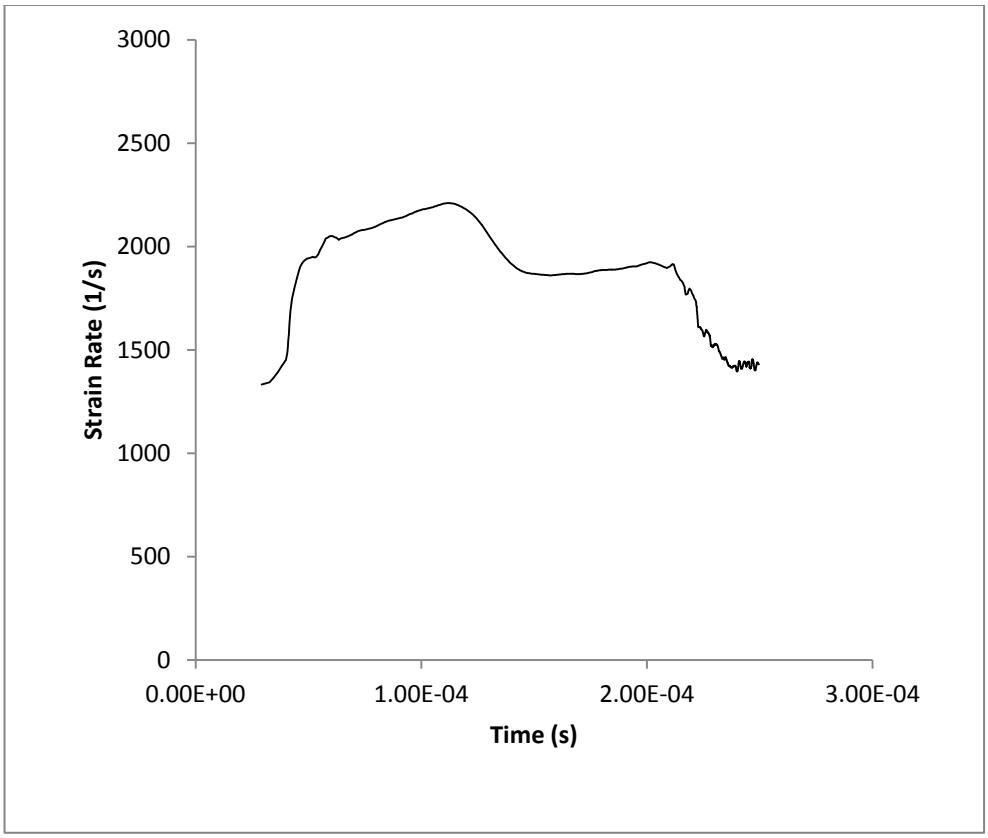

Figure 4.29: Strain rate- time data calculated for simulated impact at 38kg-m/s

These results show that the nominal strain rate over the first two reflections (visible as steps in the strain rate graph, Figure 4.29) is approximately 2000/s and 1700/s respectively, which lies well within the acceptable range of 500/s to 3000/s for the parameters.

Summary of Major Results

The Anand parameters, implemented with the Feng and Bassim model to describe the homogenous and hardening behaviour, were shown to agree well with experimental results for the homogenous constant strain rate stress-strain data obtained experimentally using a direct impact pressure bar. The extension of the Feng and Bassim model to include the physically motivated phenomenon of dynamic recrystallization was demonstrated using a simplified model of a single element that deforms plastically and experiences a temperature rise due to plastic deformation. The material was demonstrated to lose load carrying capacity seamlessly as the dynamic recrystallization temperature is reached. The total temperature rise, as well as the shape of the stress resistance curve, showing hardening, softening, and collapse, agrees with and validates the results Feng and Bassim (1999).

The model was extended to 2 dimensions and the functionality was demonstrated with a simulation of a direct impact experiment. The predicted temperature rise, deformation resistance, and plastic shear strain were examined for several representative elements around and outside of the region of where ASB were expected to form. The region of expected ASB formation showed sufficient temperature rise for dynamic recrystallization at a time of approximately 0.25ms (Figure 4.24), corresponding to a nominal shear of approximately 40% (Figure 4.28). The strain rate calculated in the simulated direct impact experiment were validated by the range of nominal strain rates measured experimentally of 500/s to 3000/s (Figure 4.29).

A similar temperature rise was observed to occur at the centre of the specimen, but no shear bands have been observed in this region. This lack of shear localization was explained by the shear strain curve (Figure 4.26), which shows that there is insufficient shear stress to initiate localization in the centre of the specimen. These results and observations are examined in more detail in the following chapter.

CHAPTER 5: DISCUSSION

The modeling of adiabatic shear bands is important for any application that involves deforming metals at high strain rates and large strains. Traditional material models, such as the Johnson-Cook model, does not capture the unique failure modes associated with these loading conditions, namely ASBs. Criteria for failure in these models is typically percentage of maximum strain or a certain level of maximum allowable stress. Past this point, the model no longer applies. The main challenge of high strain rate failure is related to the buildup of heat which has insufficient time to dissipate into the surrounding material by conduction. Many finite element packages do not include the ability for materials to self-heat during plastic deformation. This ability is critical to modelling behaviour of metals at high strain rates. Feng and Bassim (1999) address these issues and examined the evolution of ASBs in steel by considering the hardening and softening as competing mechanisms. They developed a finite element model that not only included temperature rise due to plastic work, but also softening and loss of mechanical properties.

This thesis aims to validate and extend the model of Feng and Bassim to 2D and proposes a physically motivated softening mechanism, namely dynamic recrystallization, which allows the model to be potentially applied to other materials based on dynamic recrystallization data. This section discusses the implications and significance of the experimental and numerical results. The focus of the discussion is about the experimental results for the material model and its parameters, while the numerical discussion focuses on the results of the finite element simulation of the direct impact experiment.

5.1 Acceptable Ranges for Material Model Temperatures and Strain Rates

Anand's parameters, as adapted for use at high strain rate by Feng and Bassim, were determined in this thesis for AISI 4340 steel for temperatures from 20^{o}C to 500^{o}C and strain rates from approximately 500/s to 3000/s. Anand's model is inherently non-linear and the parameters are only strictly valid over the range which they are fit. It is important to determine what happens outside of these regions to determine which parameters, if any, may be extrapolated to other loading conditions. This section examines the effect on the saturation stress if these temperature and strain rate ranges are exceeded. This information may be applied to future simulations using these parameters, especially in cases where it is desirable to extend the model to temperatures or strain rates outside of the prescribed ranges.

As discussed in the results section, and shown in Figure 4.11, the data does not show very strong strain rate dependence. This is clear from the experimental results in Table 4.3 since there was often no increase in saturation stress at increasing strain rates over the range tested. As a result of this observation, the effect of varying strain rate is not expected to have a very large impact on the saturation stress. It is also apparent from the trends in the temperature dependence graphs that a much larger difference in saturation stress is observed between the room temperature and 300^{o}C specimens than the 300^{o}C and 500^{o}C specimens. This trend suggests that the model should be more sensitive to temperatures below the fitted range than temperatures above, with lower temperatures causing the material to behave stiffer than expected. The simulated curves for strain rate and temperature dependence outside of the prescribed range are shown in Figure 5.1 and Figure 5.2 respectively.

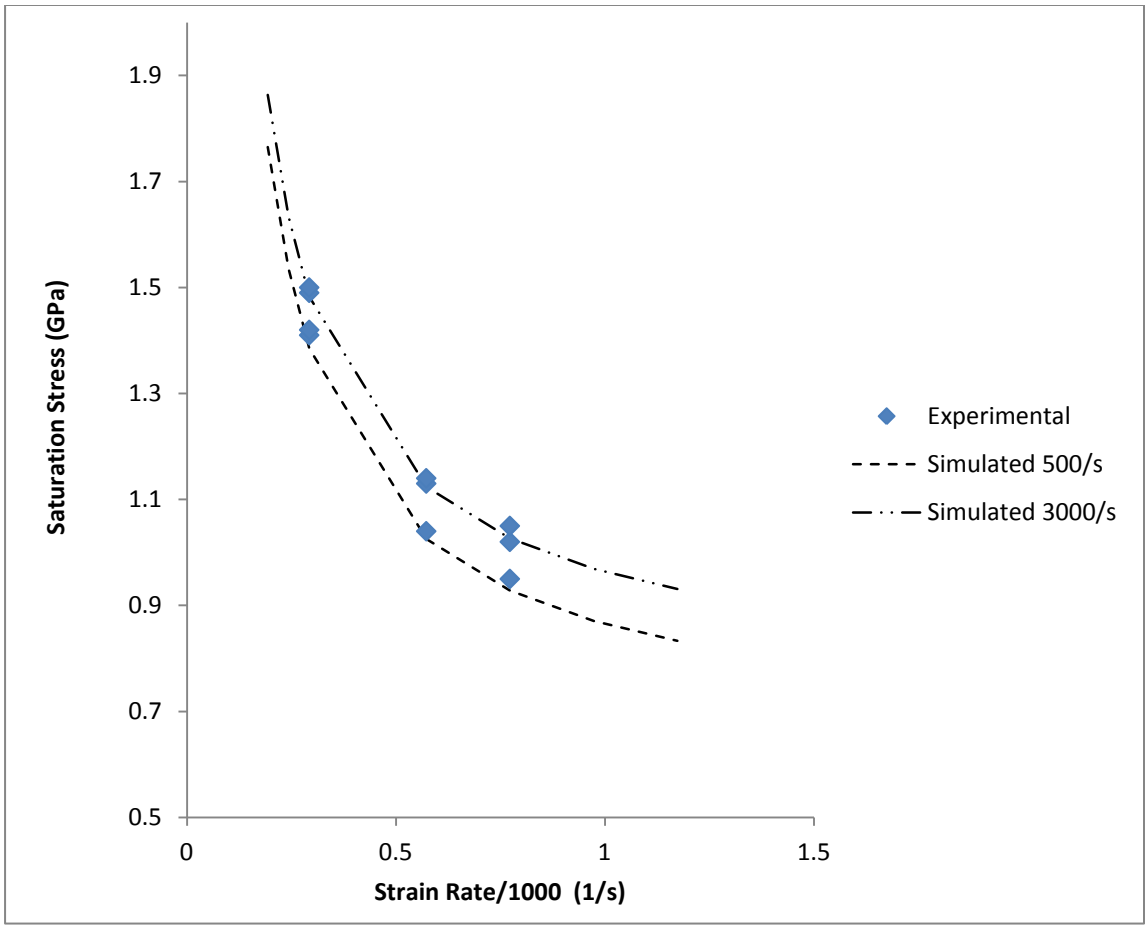

Figure 5.1: Effect of specifying temperatures outside of the fit range of 20-500^{o}C

The experimental data obtained from the direct impact tests is represented by the data points and the broken lines represent the simulated behaviour that would be predicted under these temperatures and strain rates. The range where the model is strictly valid is the region bounded by the experimental data points. Observing the effect of temperatures outside of the designated range of 20^{o}C to 500^{o}C, the values for saturation stress are found to be far more sensitive to a decrease than an increase in temperature, which confirms the assumption made previously. This trend is clearly visible in Figure 5.1, which shows a much more severe slope on the left side than the right. This effect is

slightly more pronounced at lower strain rates, with the values at the lower edge of the strain rate range showing approximately 10% more change versus the values at the high end of the strain rate range. The trends observed here suggest that caution should be exercised when extrapolating these parameters to lower temperatures, since the material may behave unrealistically stiff.

Table 5.1 shows the relative effect of change in temperature at both low and high strain rates. The baseline column lists the predicted saturation stress at the nearest bounding point from the experimental data. This value represents the last known data point for which the material model parameters are known to be reliable, specifically at a temperature of either 773 or 293 K (Table 5.1), or strain rate of 3000/s or 500/s (Table 5.2).

Table 5.1: Effect of varying temperature outside of designated range of 20-500°C

	Predicted Saturation Stress (MPa)	**Temperature (K)**	**Strain Rate (1/s)**	**Baseline (MPa)**	**Change From Baseline**
10% Above Maximum	1001	850.3	3000	1026	-2.5%
	903	850.3	500	928	-2.7%
20% Above Maximum	980	927.6	3000	1026	-4.5%
	881	927.6	500	928	-5.0%
10% Below Minimum	1564	263.7	3000	1483	5.5%
	1466	263.7	500	1384	5.9%
20% Below Minimum	1666	234.4	3000	1483	12.4%
	1568	234.4	500	1384	13.3%

From Table 5.1, the percentage change from baseline becomes larger as the temperature is decreased (5.5 to 12.4 and 5.9 to 13.3), which suggests that the saturation stress continues to trend upwards at an increasing rate. The values for increasing

temperature show the opposite trend, with the percentage change becoming smaller at increasing temperature. This observation suggests that the model is more stable for increasing than decreasing temperatures, and confirms the assumption made previously from the shape of the graph and trends in experimental data.

A similar approach is taken to establish the sensitivity of the model outside of prescribed ranges for strain rate. Strain rate is often taken logarithmically, since changes in material behaviour only occur over orders of magnitude. For this reason, two additional data points are provided in Table 5.2 to represent what occurs at the bounds of the low to high strain rate regimes (1/s and 10^5/s).

Table 5.2: Effect of varying strain rate outside of designated range of 500-3000/s

	Predicted Saturation Stress (MPa)	**Temperature (K)**	**Strain Rate (1/s)**	**Baseline (MPa)**	**Change From Baseline**
10% Above Maximum	1488	293	3300	1483	0.4%
	1031	773	3300	1026	0.5%
20% Above Maximum	1493	293	3600	1483	0.7%
	1036	773	3600	1026	1.0%
10% Below Minimum	1378	293	450	1384	-0.4%
	922	773	450	928	-0.6%
20% Below Minimum	1372	293	400	1384	-0.9%
	916	773	400	928	-1.3%
Low Strain Rate	1043	293	1	1384	-24.6%
	587	773	1	928	-36.8%
Very High Strain Rate	1549	293	10000	1384	11.9%
	1092	773	10000	928	17.7%

The strain rate is less sensitive to small changes of 10-20% outside of the range. Higher strain rates show less error than lower strain rates, with this error magnified at

higher temperatures. At low strain rates of 1/s, the error is quite large at almost 40%. Under quasi-static loading conditions (10^{-4}/s), the material is predicted to saturate at only 400MPa. This large error suggests that these parameters should not be used for lower strain rate applications, especially at elevated temperatures since the material may behave unrealistically ductile. Higher strain rates appear to be less affected, with reasonable values predicted all the way up to 10^{4}/s.

Figure 5.2 shows this relationship graphically. It is important to note that the saturation stress continues to decrease logarithmically with the strain rate, and that there is no bottom bound. At low enough strain rates, the material yields plastically at any stress. This is a key component of Anand plasticity, and the reason it is applied to so many applications involving creep.

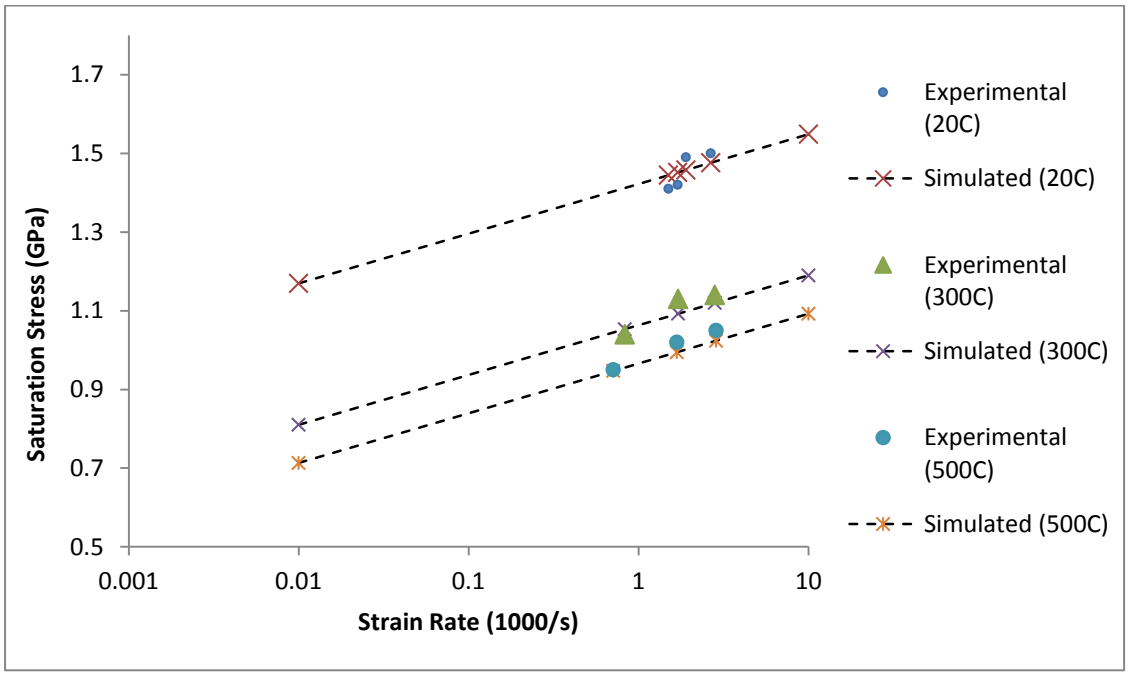

Figure 5.2: Effect of varying strain rate outside of designated range

5.2 Considerations For Extension From 1D to 2D

The model put forth by Feng and Bassim was applied to 1D torsion and initiated ASBs by weakening the element along the midline of the specimen. The present simulation extends the model to 2D by using the as-supplied material behaviour in ANSYS and using the inhomogeneity of the stress field to initiate ASB. The details and justification for the extension are discussed below.

The model of Feng and Bassim uses a 2D mesh that is modified, using special boundary conditions, to simulate 1D model geometry. The mesh simulates a strip along a torsional Hopkinson bar specimen, which experiences a state of pure shear. The geometry of the torsional Hopkinson bar specimen is a thin tube with hex flanged ends, and the loading condition is an applied torque along the axis of the specimen. A photograph showing a specimen prior to deformation is shown in Figure 5.3.

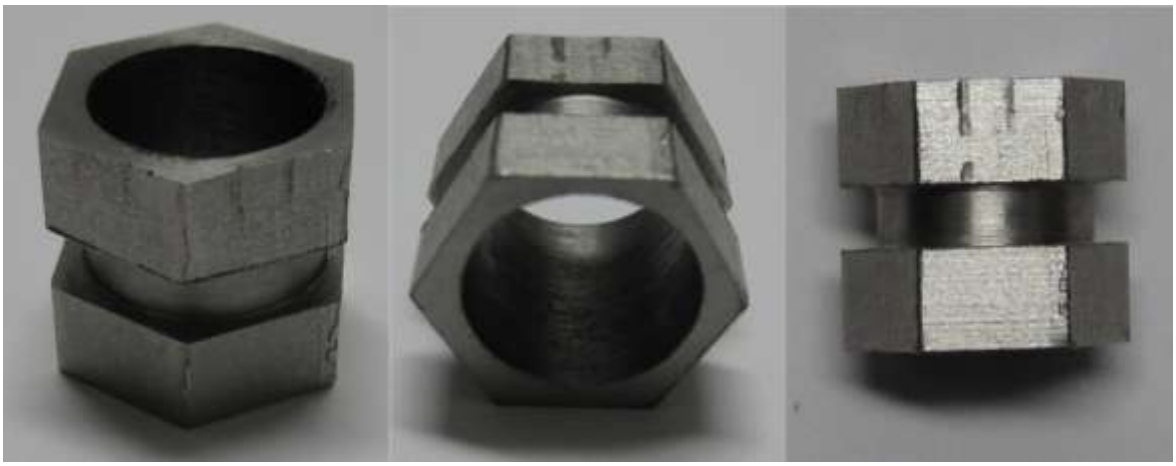

Figure 5.3: Torsional Hopkinson bar specimen

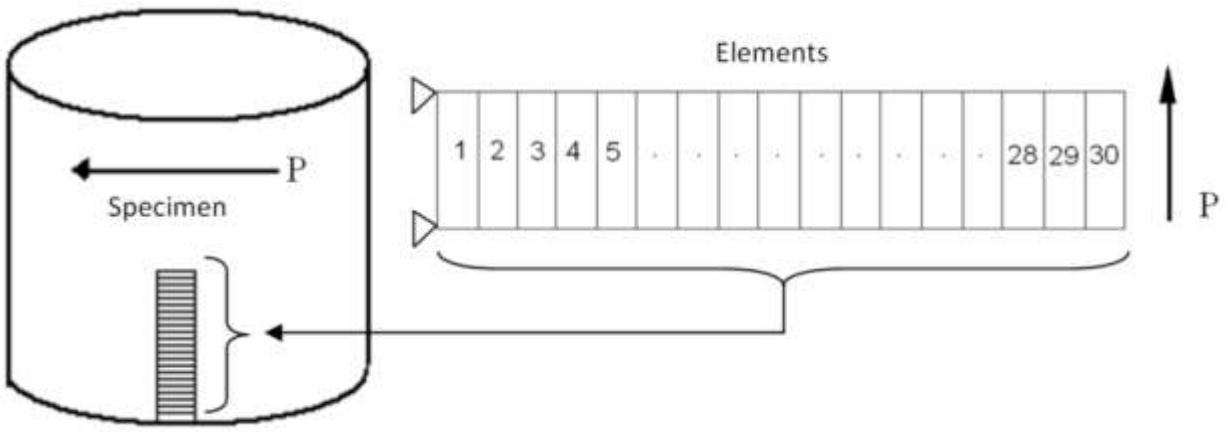

Figure 5.4: Location of finite element mesh of Feng and Bassim along specimen

The mesh of Feng and Bassim consists of 30 elements, with the edges at one edge of the model fixed in all directions to simulate the symmetry about the midline (longitudinally) of the specimen. Elements lying along the same x-location, parallel to the applied load, are constrained to have the same movement in x and y directions to satisfy radial symmetry. From this description, it is clear that special boundary conditions are needed to enforce one dimensional behaviour. By removing these special boundary conditions, the elements return to their original 2D state. ANSYS is capable of applying either plane strain or axisymmetric behaviour to these particular elements, depending on element type selected.

Feng and Bassim initiate shear bands by reducing the strength of the element along the midline of the specimen. This procedure works well with low numbers of elements (30) where the mesh is created manually, but is much more complicated with 2D geometry and automatically generated meshes. This issue is resolved when extended to 2D since the state of stress is no longer perfectly uniform, as with the torsional

specimen, and there are locations of higher shear stress present within the specimen that initiate shear bands. In this case, the inhomogeneity used to initiate shear bands is related to the stress field, instead of the material properties. This procedure is demonstrated in the final results for the 2D direct impact specimen, showing increased shear strain and temperature rise along lines at 45 degrees along the plane of symmetry. The 1D state of compressive stress is disturbed by the radial constriction due to friction at the specimen/bar interfaces, and the regions of highest shear stress are resolved along planes inclined at 45 degrees. In the physical specimen, these planes form an hourglass shape and are the regions where ASBs are found to form. These locations are correctly identified by the model and show increased temperature and shear strain, which is indicative of the initiation of ASBs.

5.3 Predicting time of occurrence of localization from the deformation resistance curves

The deformation resistance curve is valuable for predicting the timing for collapse, as well as the total shear strain present at the time of ASB formation. The deformation resistance curve, as generated by Feng and Bassim, consists of three stages. The first stage is strain hardening, followed by thermal softening, and finally stress collapse. The model predicts the hardening behaviour by using a large hardening coefficient, and the softening and collapse are modeled together using an empirical softening relationship that directly adjusts the deformation resistance parameter as the temperature increases. The present model accounts for the hardening and softening behaviour together by using the as-fit homogenous material properties, and uses a dynamic recrystallization term for the stress collapse portion. This curve is shown to have the same shape, regardless of the way it is generated. This validates the initial premise of Feng and Bassim that the timing for localization could be identified by observing the shape of the deformation resistance curve.

The 2D model has an important difference from the 1D model of Feng and Bassim in the way ASB initiation is identified. The deformation resistance curve alone is not enough to predict whether shear bands are expected for form in a specific location, only if it is possible for them to form. As an example, the location at the centre of the direct impact specimen does not exhibit ASB formation, but the deformation resistance curve specifies that the material has lost structural integrity . This is due to the fact that the state of stress at this location does not include a shear component. When predicting the formation of ASBs using the 2D model, it is therefore necessary to examine not only

whether there is loss of integrity, but also whether there is shear stress present to drive the formation of ASBs. In the 1D torsional model, the state of stress is pure shear and there is always shear stress present to drive the formation of ASBs. With 2D simulations, it is necessary to first identify those locations susceptible to ASBs from the deformation resistance curves, and then examine the state of stress around the area, specifically the presence of shear stress. From the deformation resistance curves for the direct impact case, loss of structural integrity is predicted along planes 45 degrees to the axis of symmetry of the specimen, as well as at the centre of the specimen. Examination the shear stress curve from these locations reveals that the only place with both shear strain and loss of structure are the planes inclined at 45 degrees. This agrees with the locations that ASBs are observed on the physical specimen.

5.4 Width of Predicted ASBs

ASBs are known to be very thin in one direction with respect to the other two. This is an important feature of ASBs that the model should replicate. The shear strain, deformation resistance, and temperature are measured in an element along the plane where ASB is predicted, and one element nearby. The results (Figure 5.5) show that the amount of shear strain found in the nearby element decreases significantly moving away from the plane of maximum shear.

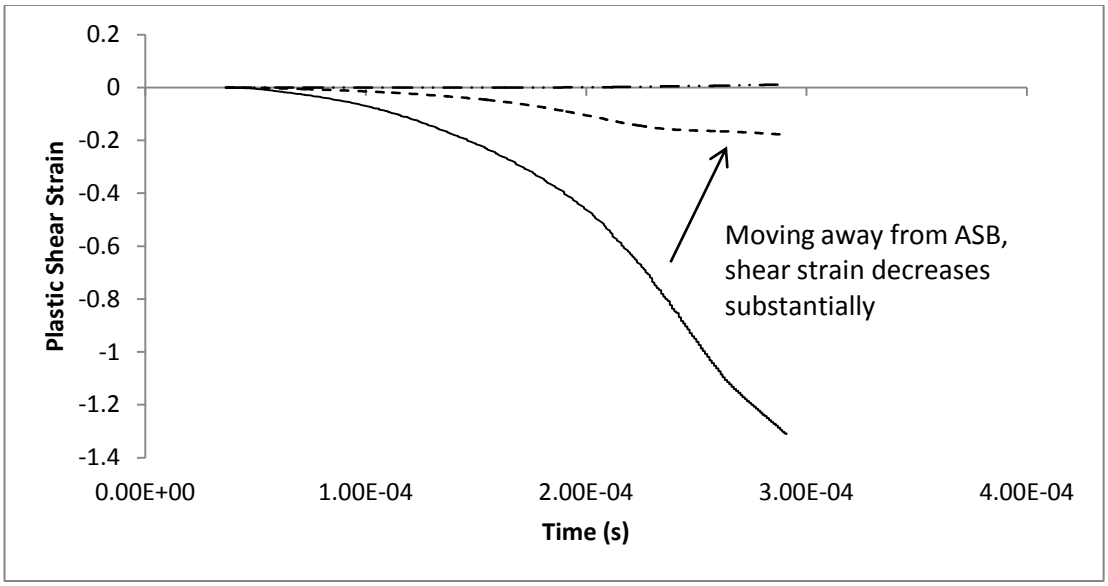

Figure 5.5: Shear stress at site of predicted ASB, near ASB, and at centre of specimen.

From Figure 5.5, the shear strain decreases by a factor of approximately 10 by moving one element length away from the plane of the ASB. This is supported by the experimental observation of ASBs as very narrow and localized regions, with most of the shear strain contained within a small region. The resolution of the ASB in the current model is limited by the fineness of the mesh, which has been selected as the maximum resolution possible with the available computer resources. This corresponds to an element size of approximately 200 μm. Experimental observation of ASBs places their width at a maximum of approximately half that value, which exceeds the resolution of the mesh. The important observation here is that the shear strain drops off very quickly, within the distance of a single element, suggesting that the region of localization is less than one element, or 200 μm. This observation is consistent with what would be expected for a shear band of average width (less than 100 μm) in steel.

5.5 Multiple ASBs

An advantage of the 2D program is that several localization points may be predicted, and the severity and timing of the ASB formation at each site can be quantified. If a certain geometry has more than one location where shear bands are expected, the program is able to predict the timing for each site and reveal which site is more susceptible to shear bands. This feature is observed in the program for the direct impact simulation, where there are two regions of high shear strain evolving as deformation proceeds. The first region is located at the specimen-bar interface, and the second is located at the specimen-projectile interface.

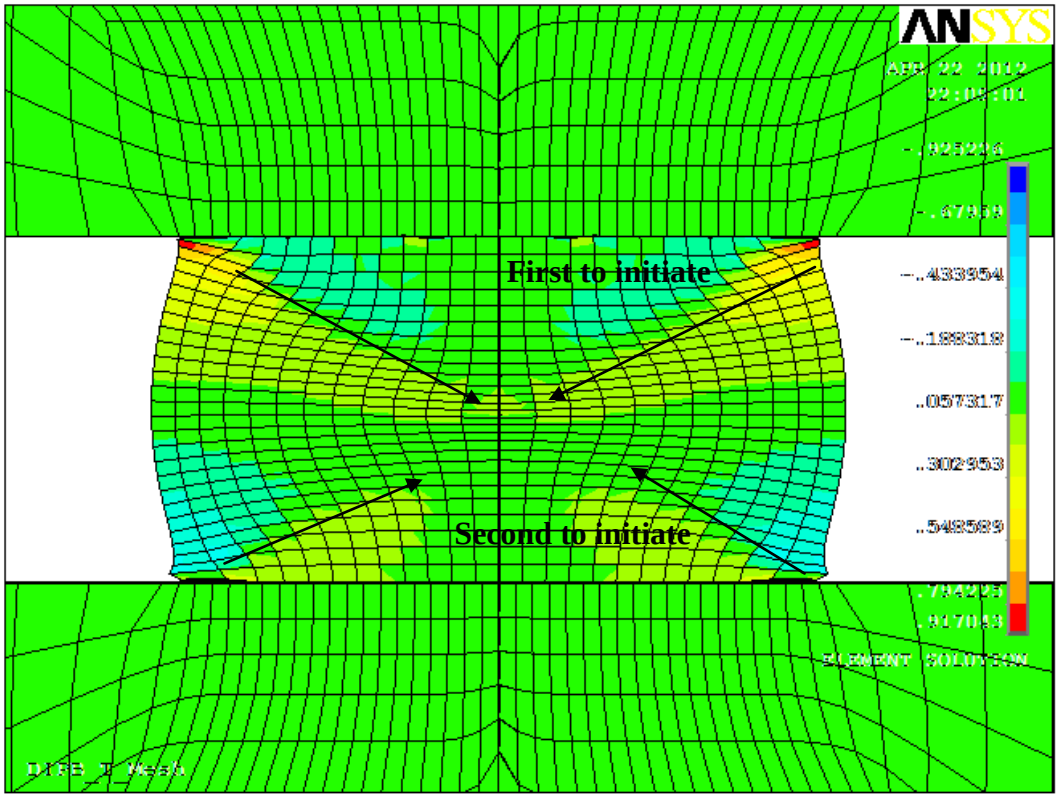

Figure 5.6: Simulated plastic shear strain in specimen impacted at 38kg-m/s showing timing for first and second set of ASBs

From Figure 5.6, the relative severity of the ASB sites is clear. The site at the top of the figure shows much higher shear strain, and the regions of high shear extend much farther than the second set initiating from the bottom of the figure. The timing is examined by recording the time-history of an element along each 45 degree plane, near the corner, from the bar-specimen interface and the striker-specimen interface. The plots for shear strain and deformation resistance as functions of time are shown in Figure 5.7 and Figure 5.8 respectively.

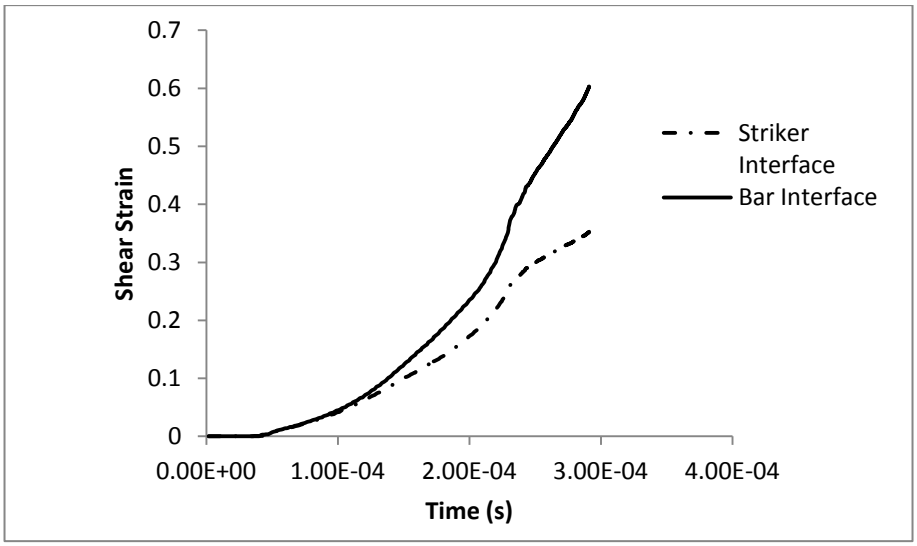

Figure 5.7: Predicted timing and severity of two ASB sites

Figure 5.7 shows that the severity of the ASB is higher for the location at the striker interface, which is expected from the results of the deformed mesh. However, it is interesting to note that the timing for the initiation is almost identical. This is supported by Figure 5.8, which shows the evolution of the deformation resistance as a function of time for each of these elements. The deformation resistance evolves almost identically,

except for a slight increase in the rate of collapse for the bar interface near the end of the graph (approximately $3x10^4$ s).

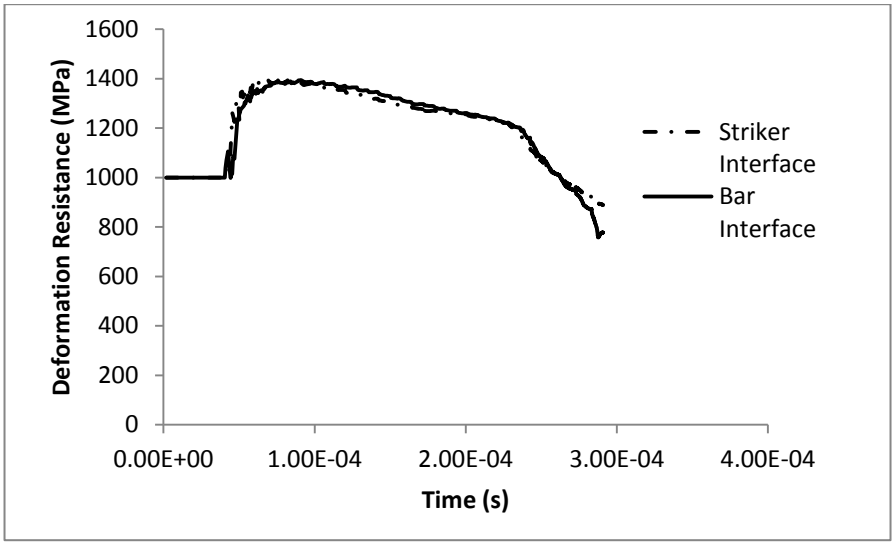

Figure 5.8: Deformation resistance predicted by 2D model for two ASB sites

5.6 Predicting Nominal Failure Strain on Stress-Strain Curves

The timing is important for determining the location on the stress-strain curve where the localization is possible. Prior to this point, the probability of forming ASBs is low, and this may be viewed as the safe zone for design. Past the point of collapse, ASBs are likely and the material is much more susceptible to failure. The timing for localization is mapped back to the nominal stress-strain curve by recording the displacement of each end of the specimen and calculating from this the strain-time information. This strain-time represents the nominal strain of the entire specimen, which allows the numerical results of the simulation to be compared directly with experimental results that use nominal stress-strain curves.

Odeshi et al. (2005) found that the localization strain was approximately 0.4 to 0.5 for AISI 4340 tempered at 650°C. Similar results are reported by Boyake-Yiadom (2010) for the same steel and temper, and a localization strain of approximately 0.3 was reported for the same steel tempered at 450°C. These results agree with the results from the current simulation, which predicts a critical strain of approximately 0.4 for AISI 4340 steel tempered at 550°C. Mapped back to the stress-strain curve for a comparable experiment (250kPa firing pressure yields approximately the same conditions as the simulation) from the current work shows good agreement, with the drop in gross yield stress occurring around the same location as predicted by the model using dynamic recrystallization. Also of interest here is the adiabatic softening observed from nominal strain of 0.20 to 0.35, which is accurately captured by the present model.

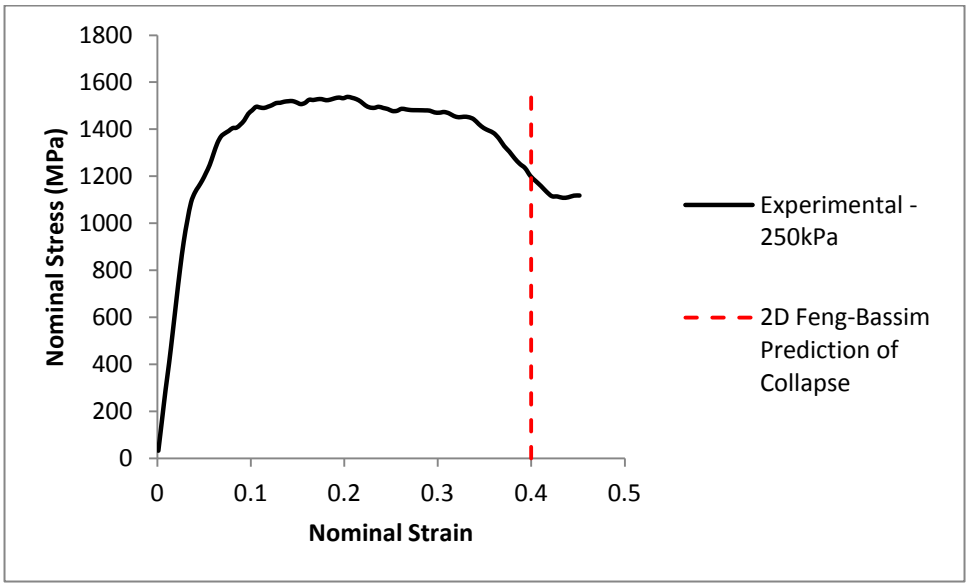

Figure 5.9: Nominal stress-strain curve for specimen impacted at a firing pressure of 250kPa showing predicted area of collapse from 2D Feng and Bassim program

These results validate the approach of Feng and Bassim, specifically the use of deformation resistance curves as predictors for failure, and show that the use of dynamic recrystallization as a localization mechanism provides reasonable results for the timing of localization in steel.

Standard finite element simulations in the literature are limited to locations prior to ASB formation, since there is no softening mechanism to account for intense localized shear strain that occurs at high strain rates. Unfortunately, these simulations have no way of knowing where this point is along the stress-strain curve. This point is shown by the present work, both experimentally and simulated, to occur at approximately 40% nominal strain for the direct impact of AISI 4340 steel tempered at 550^{o}C. The results above show that the extended 2D Feng and Bassim model predicts not only how far along the stress strain curve collapse occurs, but actually models the loss of strength associated with the formation of ASBs. This program effectively extends the predictive capabilities of the standard homogenous finite element model up to and including the point of instability and collapse.

5.7 Summary of Discussion

The approach of Feng and Bassim is validated and extended to include 2D geometry. An alternate mechanism for collapse, based on a critical temperature related to dynamic recrystallization, is proposed and shown to agree well with experimental data. Experimental stress-strain curves are obtained using a direct impact pressure bar, and the results are fit to Anand's plasticity model. Anand's parameters are obtained for AISI 4340 steel at temperatures from 20-500^{o}C and strain rates from 500-3000/s. These

parameters are shown to fit well to experimental data within the recommended ranges, but care should be taken when extrapolating to lower temperatures or strain rates.

A model is developed to extend the model of Feng and Bassim from 1D to 2D. The main features that make this model distinctive from the original are firstly the modification of the original boundary conditions to remove the imposed 1D condition, namely the coupled displacement condition, and secondly the triggering of ASB by stress-based inhomogeneity as opposed to the original material-based inhomogeneity. The program is shown to work well with a variety of boundary conditions (including uniaxial and contact), providing the stress is sufficiently non-uniform.

The model is shown to predict material softening and collapse, but it also shows that this does not mean that ASBs form wherever the material is shown to collapse. To initiate ASBs, the loss of structure must be accompanied by shear stress. This is generally not a concern, since the amount of shear stress required to plastically deform the collapsed material is very small. Locations in the model where collapse is predicted should be checked for shear strain. Areas susceptible to ASB show much higher shear strain than the surrounding regions, even moving away from the ASB by the distance of a single element. The width of an element with the finest mesh was 200μm, or approximately twice the size of the largest ASB expected from experimental observation. The fact that the shear strain diminished so quickly away from the simulated ASB agrees with the experimental observation that the shear bands are smaller than the resolution of the mesh.

The 2D program is shown to be capable of predicting several ASBs in a single simulation, and predict the timing and relative severity of each. The timing for ASB formation is mapped back to the experimental observations of the present work, as well as the observations of other experimentalists (Odeshi et al.(2005), Boakye-Yiadom(2010)) and found to agree with the value of 40-50% for an impact momentum of 38 kg-m/s.

The 2D Feng and Bassim approach presented here extends the modeling capabilities of standard finite element models further along the stress-strain curve for high strain rate deformation to predict the timing for the onset of ASBs, as well as modeling the loss of structural integrity associated with it.

CHAPTER 6: CONCLUSIONS

The purpose of the present research was to validate and extend the finite element model of Feng and Bassim for predicting the onset of thermomechanical instability in metals, namely the formation and evolution of adiabatic shear bands. General purpose plasticity models are only capable of predicting the behaviour of a material accurately up to the point of instability, which in itself is also unknown to these models. The model of Feng and Bassim extends the useful range of finite element simulation, since it not only identifies when localization will occur, but also changes the material behaviour to simulate the stress collapse associated with adiabatic shear bands. The model of Feng and Bassim, initially developed for 1D torsion, was extended to include 2D states of stress and restructured to simulate dynamic recrystallization. This research validated the underlying assumptions of the Feng and Bassim model, specifically that the formation of adiabatic shear bands may be predicted by considering the sum of the hardening and softening of a material. A summary of the conclusions drawn from the present research is given below:

- Material model parameters for the Feng and Bassim model were determined for AISI 4340 steel tempered for 2hrs at 550^{o}C. These parameters were shown to be valid between temperatures of 20-500^{o}C and strain rates of 500-3000/s. Outside of this range, the model was found to be most sensitive to temperatures below the prescribed limits.
- The simulated stress resistance curves obtained from both the direct impact simulation and the uniaxial single element experiment were found to have the same shape as the original Feng and Bassim curves, indicating that the

deformation resistance curve method proposed by Feng and Bassim for predicting the onset of thermomechanical instability is effective regardless of the mechanism being modeled.

- The simulated direct impact experiment showed significant temperature rise of several hundred degrees at the site of ASB formation. This temperature rise is enough to initiate dynamic recrystallization.
- The simulated temperature rise was found to be highest at the centre and along planes 45 degrees to the longitudinal axis.
- The critical temperature for dynamic recrystallization was shown to predict the onset of collapse accurately, and the results for the timing of collapse match experimental observations for nominal strain at time of localization.
- Simulations of 2D geometry require not only sufficient temperature rise, but also a shear stress to drive the formation of adiabatic shear bands.
- The Feng and Bassim model is capable of initiating shear bands from a homogenous material with an inhomogeneous stress field.
- Should there be multiple ASBs in a specific simulation, the deformation resistance together with the plastic shear strain curves may be used to predict the relative severity and timing for each.
- The predicted width of the shear band was found to be less than the maximum resolution of the mesh, 200 μm, which agrees with the expected size of 20-100 μm.

REFERENCES

Anand, L. 1985. "Constitutive equations for hot-working of metals." *International Journal of Plasticity* no. 1 (3):213-31.

Andrade, U., M. A. Meyers, K. S. Vecchio, and A. H. Chokshi. 1994. "Dynamic Recrystallization in High-Strain, High-Strain-Rate Plastic-Deformation of Copper." *Acta Metallurgica Et Materialia* no. 42 (9):3183-3195.

Ashby, M. F., and R. A. Verrall. 1973. "Diffusion-accommodated flow and superplasticity." *Acta Metallurgica* no. 21 (2):149-163.

Bai, Yilong, and Bradley Dodd. 1992. *Adiabatic shear localization : occurrence, theories, and applications*. 1st ed. Oxford ; New York: Pergamon Press.

Bassim, M. N. 2001. "Study of the formation of adiabatic shear bands in steels." *Journal of Materials Processing Technology* no. 119 (1-3):234-236.

Bassim, M. N., and N. Panic. 1999. "High strain rate effects on the strain of alloy steels." *Journal of Materials Processing Technology* no. 93:481-485.

Batra, R. C., and C. H. Kim. 1992. "Analysis of Shear Banding in 12 Materials." *International Journal of Plasticity* no. 8 (4):425-452.

Batra, R. C., and M. H. Lear. 2004. "Simulation of brittle and ductile fracture in an impact loaded prenotched plate." *International Journal of Fracture* no. 126 (2):179-203.

Boakye -Yiadom, Solomon. 2011. "Effect of heat treatment on stability of adiabatic shear bands in 4340 steel." Masters Thesis, University of Manitoba: Winnipeg, Canada.

Bose, A., H. Couque, and J. Lankford Jr. 1992. Shear localization in tungsten heavy alloys. Paper read at Powder Metallurgy World Congress, at San Francisco, CA, USA.

Brown, S. B., K. H. Kim, and L. Anand. 1989. "An internal variable constitutive model for hot working of metals." *International Journal of Plasticity* no. 5 (2):95-130.

Callister, William D. 1994. *Materials science and engineering : an introduction*. 3rd ed. New York: Wiley.

De Souza Neto, E., P.D. Periæ, P.D.R.J. Owen, E.A. De Souza Neto, and D.R.J. Owen. 2008. *Computational Methods for Plasticity: Theory and Applications*: John Wiley & Sons.

Dolinski, M., D. Rittel, and A. Dorogoy. 2010. "Modeling adiabatic shear failure from energy considerations." *Journal of the Mechanics and Physics of Solids* no. 58 (11):1759-1775.

Erlich, D. C., L. Seamen, and D. A. Shockley. 1980. Development of a computational shear band model. Aberdeen Proving Ground, MD: U.S. Army Ballistic Research Laboratory.

Feng, H., and M. N. Bassim. 1999. "Finite element modeling of the formation of adiabatic shear bands in AISI 4340 steel." *Materials Science and Engineering a-Structural Materials Properties Microstructure and Processing* no. 266 (1-2):255-260.

Frenkel, J. 1926. "The theory of the elastic limit and the solidity of crystal bodies." *Zeitschrift Fur Physik* no. 37 (7/8):572-609.

Hartley, K. A., J. Duffy, and R. H. Hawley. 1987. "Measurement of the temperature profile during shear band formation in steels deforming at high strain rates." *Journal of the Mechanics and Physics of Solids* no. 35 (3):283-301.

Hines, J. A., and K. S. Vecchio. 1997. "Recrystallization kinetics within adiabatic shear bands." *Acta Materialia* no. 45 (2):635-649.

Hull, Derek, and D. J. Bacon. 1984. *Introduction to dislocations*. 3rd ed, *International series on materials science and technology*. Oxford Oxfordshire ; New York: Pergamon Press.

Johnson, G. R., and W. H. Cook. 1985. "Fracture Characteristics of 3 Metals Subjected to Various Strains, Strain Rates, Temperatures and Pressures." *Engineering Fracture Mechanics* no. 21 (1):31-48.

Johnson, G. R., and T. J. Holmquist. 1988. "Evaluation of Cylinder-Impact Test Data for Constitutive Model Constants." *Journal of Applied Physics* no. 64 (8):3901-3910.

Johnson, G.R., and W.H. Cook. 1983. "A constitutive model and data for metals subjected to large strains, high strain rates and high temperatures." *Proceedings of the 7th International Symposium on Ballistics*:541-547.

Kad, B. K., M. Gebert, M. E. Kassner, and M. A. Meyers. 2006. "Microstructural evolution and grain refinement in HCP-Zr shear bands." *Journal De Physique Iv* no. 134:1137-1144.

Klepaczko, J. R. 1994. "An experimental technique for shear testing at high and very high strain rates. The case of a mild steel." *International Journal of Impact Engineering* no. 15 (1):25-39.

Lee, W. S., T. H. Chen, C. F. Lin, and G. T. Lu. 2010. "Adiabatic Shearing Localisation in High Strain Rate Deformation of Al-Sc Alloy." *Materials Transactions* no. 51 (7):1216-1221.

Liao, S. C., and J. Duffy. 1998. "Adiabatic shear bands in a Ti-6Al-4V titanium alloy." *Journal of the Mechanics and Physics of Solids* no. 46 (11):2201-2231.

Marchand, A., and J. Duffy. 1988. "An experimental study of the formation process of adiabatic shear bands in a structural steel." *Journal of the Mechanics and Physics of Solids* no. 36 (3):251-283.

McQueen, H. J., and S. Bergerson. 1972. "Dynamic Recrystallization of Copper during Hot Torsion." *Metal Science* no. 6 (1):25-29.

Medyanik, Sergey N., Wing Kam Liu, and Shaofan Li. 2007. "On criteria for dynamic adiabatic shear band propagation." *Journal of the Mechanics and Physics of Solids* no. 55 (7):1439-1461.

Meyers, M. A. 1994. "Dynamic Failure - Mechanical and Microstructural Aspects." *Journal De Physique Iv* no. 4 (C8):597-621.

Meyers, M. A., and H. R. Pak. 1986. "Observation of an Adiabatic Shear Band in Titanium by High-Voltage Transmission Electron-Microscopy." *Acta Metallurgica* no. 34 (12):2493-2499.

Murr, L.E., K.P. Staudhammer, and M.A. Meyers. 1995. *Metallurgical and materials applications of shock-wave and high-strain-rate phenomena: proceedings of the 1995 International Conference on Metallurgical and Materials Applications of Shock-Wave and High-Strain-Rate Phenomena (EXPLOMET '95)*: Elsevier.

Nazimuddin, Ghaznafar Mohamed. 2010. "High strain rate studies of armor materials." Masters Thesis, University of Manitoba: Winnipeg, Canada.

Odeshi, A. G., S. Al-ameeri, S. Mirfakhraei, F. Yazdani, and M. N. Bassim. 2006. "Deformation and failure mechanism in AISI 4340 steel under ballistic impact." *Theoretical and Applied Fracture Mechanics* no. 45 (1):18-24.

Odeshi, A. G., M. N. Bassim, S. Al-Ameeri, and Q. Li. 2005. "Dynamic shear band propagation and failure in AISI 4340 steel." *Journal of Materials Processing Technology* no. 169 (2):150-155.

Odeshi, A. G., G. M. Owolabi, M. N. K. Singh, and M. N. Bassim. 2007. "Deformation and fracture behavior of alumina particle-reinforced Al 6061-T6 composlite during dynamic mechanical loading." *Metallurgical and Materials Transactions a-Physical Metallurgy and Materials Science* no. 38A (11):2674-2680.

Perez-Prado, M. T., J. A. Hines, and K. S. Vecchio. 2001. "Microstructural evolution in adiabatic shear bands in Ta and Ta-W alloys." *Acta Materialia* no. 49 (15):2905-2917.

Polyzois, Ioannis. 2010. "Finite element modeling of the behavior of armor materials under high strain rates and large strains." Masters Thesis, University of Manitoba: Winnipeg, Canada.

Riqiang, Liang, and A. S. Khan. 1999. "A critical review of experimental results and constitutive models for BCC and FCC metals over a wide range of strain rates and temperatures." *International Journal of Plasticity* no. 15 (9):963-80.

Rittel, D. 2009. "A different viewpoint on adiabatic shear localization." *Journal of Physics D-Applied Physics* no. 42 (21).

Rittel, D., and S. Osovski. 2010. "Dynamic failure by adiabatic shear banding." *International Journal of Fracture* no. 162 (1-2):177-185.

Schoenfeld, S. E., and T. W. Wright. 2003. "A failure criterion based on material instability." *International Journal of Solids and Structures* no. 40 (12):3021-3037.

Shahan, A. R., and A. Karimi Taheri. 1993. "Adiabatic shear bands in titanium and titanium alloys: a critical review." *Materials & Design* no. 14 (4):243-250.

Shawki, T. G., and R. J. Clifton. 1989. "Shear band formation in thermal viscoplastic materials." *Mechanics of Materials* no. 8 (1):13-43.

Stock, T. A. C., and K. R. Thompson. 1970. "Penetration of Aluminum Alloys by Projectiles." *Metallurgical Transactions* no. 1 (1):219.

Tresca, M. H 1878. "On Further Applications of the Flow of Solids." *Proceedings of the Institution of Mechanical Engineers* (29):2.

Wright, T. W. 2002. *The physics and mathematics of adiabatic shear bands*, *Cambridge monographs on mechanics*. Cambridge, UK ; New York: Cambridge University Press.

Wright, T. W., and R. C. Batra. 1985. "Further Results on the Initiation and Growth of Adiabatic Shear Bands at High-Strain Rates." *Journal De Physique* no. 46 (Nc-5):323-330.

Wright, T. W., S. E. Schoenfeld, K. T. Ramesh, and X. Y. Wu. 2004. "Progress in computational models for damage from shear bands and voids." *Shock Compression of Condensed Matter - 2003, Pts 1 and 2, Proceedings* no. 706:629-632.

Xu, Y. B., X. Wang, Z. G. Wang, L. M. Luo, and Y. L. Bai. 1990. "Formation and Microstructure of Localized Shear Band in a Low-Carbon Steel." *Scripta Metallurgica Et Materialia* no. 24 (3):571-576.

Xu, Y. B., W. L. Zhong, Y. J. Chen, L. T. Shen, Q. Liu, Y. L. Bai, and M. A. Meyers. 2001. "Shear localization and recrystallization in dynamic deformation of 8090 Al-Li alloy." *Materials Science and Engineering a-Structural Materials Properties Microstructure and Processing* no. 299 (1-2):287-295.

Yazdani, F., M. N. Bassim, and A. G. Odeshi. 2009. "The formation of adiabatic shear bands in copper during torsion at high strain rates." *Mesomechanics 2009* no. 1 (1):225-228.

Zener, C., and J. H. Hollomon. 1944. "Effect of strain rate upon plastic flow of steel." *Journal of Applied Physics* no. 15 (1):22-32.

Zerilli, F. J., and R. W. Armstrong. 1987. "Dislocation-mechanics-based constitutive relations for material dynamics calculations." *Journal of Applied Physics* no. 61 (5):1816-25.

Zhou, M., G. Ravichandran, and A. J. Rosakis. 1996. "Dynamically propagating shear bands in impact-loaded prenotched plates .2. Numerical simulations." *Journal of the Mechanics and Physics of Solids* no. 44 (6):1007.

Zou, D. L., L. Zhen, C. Y. Xu, and W. Z. Shao. 2011. "Characterization of adiabatic shear bands in AM60B magnesium alloy under ballistic impact." *Materials Characterization* no. 62 (5):496-502.